Süleyman Dündar

Imaging of the crustal, lithospheric and upper mantle structure beneath the westernmost mediterranean region using P- and S-receiver function methods

Dissertation
zur Erlangung des Doktorgrades am
Fachbereich Geowissenschaften der
Freien Universität Berlin

Erstgutachter: Prof. Dr. Rainer Kind
Zweitgutachter: Prof. Dr. Marco Bohnhoff
Tag der mündlichen Prüfung: 01.11.2011

To my dear adviser and my dear parents

Rainer, Nazik, and Cevat

for their unconditional and unending support.

Table of contents

Eidesstattliche Erklärung

Hiermit erkläre ich, Süleyman Dündar, dass die Dissertation von mir selbstständig angefertigt und andere als die in der Dissertation angegebenen Hilfsmittel nicht benutzt wurden. Ich versichere, dass die wörtlichen oder dem Sinne nach anderen Veröffentlichungen entnommenen Stellen von mir kenntlich gemacht wurden. Zusätzlich erkläre ich, dass ich mich bisher keiner weiteren Doktorprüfung unterzogen habe. Ich habe die Dissertation weder in der gegenwärtigen noch in einer anderen Fassung an einer in- oder ausländischen Fakultät als Dissertation, Semesterarbeit, Prüfungsarbeit, oder zur Erlangung eines akademischen Grades vorgelegt.

Süleyman Dündar

Berlin, den 30. Juni 2011 _____

Süleyman Dündar

Statement of authorship

I, Süleyman Dündar, confirm that this PhD dissertation has been prepared, written and interpreted solely by my. I have fully acknowledged and referenced the ideas and work of others, whether published or unpublished, in my dissertation. My dissertation does not contain work extracted from any thesis, dissertation or research paper previously presented for another degree or diploma at this or any other university.

Süleyman Dündar

Berlin, 30th June 2011 _____

Süleyman Dündar

Acknowledgements

First of all, I am deeply indebted to my dear adviser, Professor Rainer Kind, for giving me an once-in-a-lifetime chance to do this dissertation and for helping me to think like a scientist. Without his help, support and expertise, I never could have finished my dissertation. In the scientific world, he is seen as a living legend. It has been a very great pleasure, honour and privilege for me to work under his direction.

Thanks also to the members of section 2.4 for their continuous help, support, and fruitful discussions: Dr. Forough Sodoudi, Dr. Xuequing Li, Dr. Barbara Heuer, Prof. Dr. Frederik Tilmann, Dr. Xiahoui Yuan, Dr. Prakash Kumar, Dr. Benjamin Heit, Manfred Stiller, Dr. Marcelo Bianchi, Dr. Winfried Hanka, Dr. Joachim Saul, Dr. Günter Asch, and Dr. Ayman Mohsen.

I also wish to thank the other people in section 2.4, who helped me in many ways and made my more than 4-years-stay a very pleasant experience: Liane Lauterjung, Susanne Hemmleb, Amerika Manzanares, Heiko Sperlich, Andriamiranto Ravelson, Shantanu Pandey, and Andreas Heinloo.

I would like to express my gratitude and thanks to Dr. Fatih Bulut and Dr. Tuna Eken for their continued assistance and support.

I am also grateful to M. A. Paul Milkaitis as well as Dr. Benjamin Heit for help in improving the English version of the dissertation.

This research project was financially supported both by the Friedrich-Ebert-Stiftung and the Helmholtz-Zentrum Potsdam Deutsches GeoForschungsZentrum (GFZ). I would like to express my sincere thanks to both institutions for their support.

The computations were made in Seismic Handler (SHC) (Stammler 1993). Most of the figures were created using Generic Mapping Tools (GMT) (Wessel and Smith 1991).

The data management centers of IRIS and GEOFON kindly provided seismograms to me.
I would also like to thank the IRIS and GEOFON teams for their cooperative support.

I also acknowledge using about two years' worth of data of the IAG Regional Network of the Spanish Andalusian Institute of Geophysics. I would like to express my deepest gratitude to Dr. Flor de Lis Mancilla for providing the seismic data.

Finally, I would like to express my sincere appreciation to my family for their unwavering support, patience, encouragement, and love throughout the last four years, and my entire life.

Abstract

From the geodynamic point of view, the westernmost Mediterranean region, containing the Alboran Domain and the surrounding land areas, is situated in the collision zone between two main tectonic plates, namely the southwestern part of the Eurasian plate (Iberia) and the African plate. Consequently, this region is characterized by a highly complex tectonic setting, as testified by its surface geology and seismicity. The north-northwestward continuing convergence between those plates, from the Cretaceous to the Neogene, led to the evolution of the contractional structural units such as the Rif, Betics and Atlas mountain chains and the creation of an intra-continental extensional basin, known as the Alboran Basin.

The seismicity of this region is closely connected with the compressional tectonic activity in the vicinity of a diffuse plate boundary between the African and Iberian plates. It is primarily characterized by events of moderate magnitude. Although most of them are shallow earthquakes ($h \leq 35$ km), with magnitudes less than 5.5, significant middle-deep earthquake activities are also observed in the investigated region ($35 \text{ km} < h < 150 \text{ km}$). The most important specific feature in seismicty is the occurrence of some deep-focus earthquakes ($h > 600$ km), whose epicenters are located in southern Spain (Granada). They are the deepest earthquakes ever registered in the Mediterranean region, und their genesis is still not very well understood. Furthermore, west of the study area, along the Azores-Gibraltar fracture zone in the Atlantic ocean is thought to be the epicenter of the Great Lisbon Earthquake of 1 November 1755, with an estimated magnitude range of 8.5-9.0 (Gutscher et al. 2006).

The formation of such contrasting surface structures in a convergent geodynamic setting and the peculiar nature of the seismic activity of this area have attracted the attention of many scientists since the early 70s. Although this region has been the focus of numerous geophysical and geological studies since then, its geodynamic evolution has remained controversial. In other words, the geodynamic models put forth thus far, are still in development and are not yet universally accepted.

An accurate knowledge of the depth variations (topography) and the geometry of the subsurface seismic velocity structures, which are located within the first 700 km of the

interior of the Earth, are of great importance to improving our understanding of the geological evolution of a tectonically active area. In this context, we investigated the seismic velocity structure under the westernmost Mediterranean Sea (Alboran Sea and surroundings regions), including the crust-mantel (Moho), the lithosphere-asthenosphere-boundary (LAB) and the upper mantle transition zone (MTZ) discontinuities at depths of 410 and 660 km. This was done by means of the parallel application of the passive seismic techniques of P- and S-receiver-functions (hereafter called PRFs and SRFs). Both techniques were developed based on the conversion of the elastic body-waves (P, S and SKS) at an interface dividing the layers with different elastic properties. In this study, the PRFs analysis was performed to image the Moho and upper mantle transition zone structures along the area of interest, whilst the SRFs analysis was conducted to resolve in a better way the variation of the LAB. The SRFs analysis avoided complications arising from the crustal-reverberations, usually known as multiples.

The database for the comprehensive PRFs- and SRFs-surveys was put together from teleseismic events with magnitudes greater than 5.7. The data was recorded at three-component seismological stations belonging to nine temporary and permanent networks which were deployed in the area of study within the framework of different seismological projects. In order to take advantage of planar wave approximation and avoid the complications of dealing with interfering phases, the PRFs and SRFs analyses were restricted to earthquakes occurring in the epicentral-distance-ranges between 30°-95° and 60°-120°, respectively. The usable teleseismic records were extracted from the database of IRIS and GEOFON data centers, using the U.S. Geological Survey Catalogue.

For this study, around 5,500 PRFs and 14,000 SRFs were created by executing a set of data processing steps. Firstly, the data quality was manually evaluated to eliminate the waveforms with unclear P-, S- and SKS-onsets. Secondly, the seismograms were rotated into P-, SH- and SV-components to obtain the highest energy of the converted phases. Afterwards, the receiver functions were computed using a time-domain deconvolution approach that allows the elimination of unknown source and path effects. Finally, the move-out correction was applied prior to the stacking of individual traces, based on event-station distance (or slowness), in order to combine coherent phases. For this purpose, a reference slowness of 6.4 s/deg was used.

Using the IASP91 velocity model, the variations of the depths to velocity discontinuities below the subject area were estimated by measuring the delay-time between the main P-, S-, and SKS-arrivals and the corresponding converted Ps-, Sp-, SKSp-phases, respectively, which were generated at the base of the seismic boundaries, such as the Moho, LAB, 410 and 660 km. We were successful in observing the presence of important lateral heterogeneities of the crust by analyzing the PRFs, utilizing the single-station-multiple-events stacking technique. Additionally, the variation of the lithospheric thickness was derived from the SRFs, applying the common conversion point (CCP) stacking technique. The results suggest that the thickness of the crust as well as the depth of LAB systematically decreases towards the east. The relatively shallow Moho as well as the shallow LAB beneath the Alboran Sea are consistent with the extensional nature of the boundary between the Iberian and African plates. We were also able to succeed in making an image of the depth of the upper mantle seismic discontinuities, applying the CCP stacking technique to the PRFs. The 410 and 660 km discontinuities were found at their expected depth, implying that mantle temperatures in the region are close to the global average.

Of all of proposed tectonic models to date, the results of this study favor the model which postulates “the convective removal of a lithospheric root beneath a previously over-thickened lithosphere” as the most likely geodynamic model.

Zusammenfassung

Von der geodynamischen Perspektive her gesehen, ist der westliche Mittelmeerraum, der das Alboran-Meer und die umgebenden Festlandregionen umfasst, insbesondere aufgrund seiner geographischen Lage ein sehr interessantes Untersuchungsgebiet für geowissenschaftliche Forschung. Es befindet sich nämlich in der hoch aktiven Kollisionszone zwischen der Afrikanischen und Eurasischen (Iberischen) Platte und entspricht damit einer geodynamisch besonders mobilen Zone unserer Erde. Dementsprechend ist die daraus resultierende Tektonik und Geodynamik dieser Region sehr kompliziert, wie es aus den seismischen Aktivitäten und den an der Oberfläche erkennbaren, geologischen Großstrukturen zum Ausdruck kommt.

Die Seismizität des Untersuchungsgebietes steht in erster Linie in engem Zusammenhang mit den kompressiven tektonischen Aktivitäten im Bereich der Plattengrenze zwischen der Afrikanischen und Iberischen Platte. Sie ist hauptsächlich durch das Auftreten von Erdbeben mit moderater Magnitude charakterisiert. Obwohl die meisten davon Flachbeben ($h \leq 35$ km) mit Magnitude weniger als 5.5 sind, werden auch signifikante seismische Aktivitäten in mittleren Tiefen ($35 \text{ km} < h < 150 \text{ km}$) beobachtet. Insbesondere bemerkenswert ist, dass auch einige Erdbeben in sehr großen Tiefen ($h > 600$ km) zu registrieren sind. Das Auftreten der Tiefenseismizität ist in einer kleinen Region im Süden von Spanien (Granada) konzentriert. Dies sind die tiefsten aufgezeichneten Erdbeben im Mittelmeerraum und ihre Ursprünge sind immer noch ein ungeklärtes Problem. Die Verteilung der Epizentren von Erdbeben lässt darauf schließen, dass die Plattengrenze eine breite und diffuse Deformationszone bildet. Des weiteren beherbergt diese Region das verheerende Erdbeben von Lissabon mit der Stärke 8.7, das am 1. November 1755 entlang der Azoren-Gibraltar-Bruchzone geschah.

Von den geologischen Oberflächenstrukturen der Region her gesehen, schließt das Untersuchungsgebiet zwei unterschiedliche, große tektonischen Einheiten ein. Die nord- bis nordwestwärts gerichtete Afrika-Iberia-Konvergenz seit dem späten Mesozoikum und die damit verbundene Kontinent-Kontinent-Kollision zwischen den beiden Platten haben zum einen auf dem Festland zur Entstehung der kompressionalen Struktureinheiten wie dem Rif, der Betischen Kordillere und den Gebirgszügen des Atlas-Systems geführt. Zum anderen ist es jedoch trotz dieser kontinuierlichen Konvergenz im geologischen Zeitalter des Neogen zu

einer Dehnungsphase gekommen, in der sich erstaunlicherweise das Alboran-Meeresbecken gebildet hat. Dieses rätselhafte Phänomen zieht seit den frühen 70er Jahren die Aufmerksamkeit der Geowissenschaftler auf sich. Eine besonders interessante Frage für diese Region besteht darin, wie sich so ein ausgedehntes Becken in einem kompressiven Regime ausbilden konnte. Die treibenden Mechanismen, die zur Entwicklung eines sich ausdehnenden Beckens in einem kompressionalen Umfeld geführt haben, sind bislang wenig verstanden und bilden somit Gegenstand äußerst kontroverser Diskussionen.

Für diese tektonisch gesehen sehr kompliziert aufgebaute Region wurden von verschiedenen Geowissenschaftlern diverse Entwicklungsmodelle entworfen. Einige der vorgeschlagenen geodynamischen Modelle lassen sich wie folgt zusammenfassen:

1) Backarc Extension westwärts-gerichteten Roll-back eines nach Ost einfallenden schmalen Slabs (rückschreitende Subduktion einer ozeanischen Lithosphäre) (Morley 1993; Royden 1993; Lonergan and White 1997; Michard et al. 2002). Dieses Modell wird durch Untersuchungen mittels seismischer Tomographie (Gutscher et al. 2002; Spakman and Wortel 2004) unterstützt.

2) Radialer Extensionskollaps, verursacht durch konvektive Entfernung des lithosphärischen Mantels (Platt and Vissers 1989; Houseman 1996).

3) Slab Detachment und Delamination von subkrustaler Lithosphäre (Garcia-Duenas et al. 1992; Comas et al. 1992; Docherty and Banda 1995; Seber et al. 1996; Calvert et al. 2000).

4) Slab-breakoff Modell (Zeck 1996)

Durch die akkurate Identifizierung und Ermittlung der lateralen Tiefenlage-Änderungen von großräumigen Strukturgrenzen im Erdinnern bis in Tiefen von bis zu 700 km können wertvolle Rückschlüsse auf die im Erdinnern vor sich gehenden, geodynamischen Prozesse, und somit auf die geologische Evolution einer tektonisch aktiven Region gezogen werden. Hierbei legt man einen großen Wert auf die exakte Bestimmung der Topographie von seismischen Grenzstrukturen, wie der Moho-Diskontinuität (Kruste-Mantel-Grenze, Moho), der Gutenberg-Diskontinuität (Lithosphären-Asthenosphären-Grenze, LAB) und den seismischen Diskontinuitäten des Oberen Mantels (410 and 660 km). In diesem

Zusammenhang besteht das Hauptziel dieser Dissertation darin, die seismischen Strukturgrenzen (Diskontinuitäten) unterhalb des westlichen Mittelmeeres und der umliegenden Regionen aufzulösen und zu kartieren. Des weiteren werden die postulierten, geotektonischen Modelle mit den erhaltenen Ergebnissen verglichen.

Um Aussagen über die sich im Inneren des westlichen Mittelmeerraumes abspielenden Prozesse treffen zu können, wird im Rahmen dieser Doktorarbeit eine Strukturanalyse des tieferen Untergrunds bis hinab in den Erdmantel mithilfe der P- und S-Receiver-Funktionen (PRF und SRF) Methoden durchgeführt. Hierbei werden die Laufzeiten der von einem natürlichen Fernbeben ausgehenden Phasen (P, S, SKS) der Raumwellen untersucht, die an seismischen Diskontinuitäten konvertiert werden (z.B. von P zu S (Ps), von S zu P (Sp) oder SKS zu P (SKSp) und steil von unten an den Stationen einfallen.

Da P-zu-S konvertierte Wellen von der LAB häufig durch multiple Reflexionen in der Kruste überlagert werden, ist die PRF Methode in vielen Fällen für die LAB-Bestimmung ungeeignet. Auf der anderen Seite sind S-Receiver-Funktionen grundsätzlich frei von diesen multiplen Reflexionen: Die direkten konvertierten Phasen (Sp,SKSp) erreichen die Stationen früher als die erzeugten S- und SKS-Wellen, und somit werden diese von der multiplen Phase nicht gestört. Davon ausgehend sind P-Receiver-Funktionen in dieser Dissertation nur zur Bestimmung der lateralen Änderung der Moho-Mächtigkeit und zur Untersuchung der oberen Manteldiskontinuitäten (410 km, 660 km) zum Einsatz gelangt. Im Gegensatz dazu werden S-Receiver-Funktionen mit dem Ziel benutzt, die laterale Tiefenvariation der Lithosphären-Asthenosphären-Grenze entlang des Untersuchungsgebietes festzustellen.

Unter der parallelen Anwendung dieser zwei voneinander unabhängigen, passiven seismischen Methoden kann ein detailliertes Abbild der großräumigen Tiefenstrukturen unterhalb des zu studierenden Gebietes erhalten werden. Um die seismischen Diskontinuitäten identifizieren und deren Tiefenlage abschätzen zu können, werden als erstes die Laufzeit-Differenzen der konvertierten Phasen (Ps, Sp, SKSp) zu den direkten Phasen (P, S, SKS) berechnet. Dann werden sie unter Anwendung des eindimensionalen IASP91 Geschwindigkeitsmodells in Tiefe umgerechnet.

Im Rahmen dieser Dissertation wurden insgesamt 5,500 P- und 14,000 S-Receiver-Funktionen berechnet. Im allgemeinen konnte die Mächtigkeit der Kruste und der

Lithosphäre entlang des Untersuchungsgebietes mit hoher Auflösung bestimmt werden. Aus der Untersuchung der P- und S-Receiver-Funktionen folgt, dass starke laterale Variationen der Moho- und LAB-Topographie im Untersuchungsgebiet festzustellen sind, was somit einen klaren Hinweis auf die komplexe tektonische Entwicklung dieser Region gibt. Darüber hinaus wird eindeutig beobachtet, dass eine systematischen Zunahme der Moho- und LAB-Tiefen von Osten nach Westen entlang der untersuchten Region zu verzeichnen ist. In der Regel ist die Kruste in der externen Zone der Alboran Domain und der ganzen Iberian Peninsula Region mächtiger als in der internen Zone, die das Alboran-Becken und die umliegende Region einschließt. Die Kruste-Mantel-Grenze (Moho) erreicht eine Maximaltiefe von etwa 40 km im Bereich der Straße von Gibraltar, wohingegen die minimale Moho-Tiefe im zentralen Bereich des Alboran Meeres etwa 16 km beträgt. In dem Untersuchungsgebiet lassen sich außerdem zwei Region feststellen, in denen die Mächtigkeit der Lithosphäre im Verhältnis zu dem restlichen Bereich des Untersuchungsgebietes deutlich abnimmt: 1) Der zentrale Bereich des Alboran Meeres und 2) die zentrale Region auf der Iberischen Halbinsel, nördlich der Betischen Kordillere gelegen. Schließlich wurden die in 410 und 660 km Tiefe im Mantel auftretenden zwei seismischen Diskontinuitäten genauer untersucht, um die Existenz von subduziertem Material dort nachzuweisen. Die 410- und die 660-km Diskontinuitäten werden in den durchschnittlichen, globalen Tiefen beobachtet, was darauf hindeutet, dass die Manteltemperatur in dieser Region nicht sonderlich anomal ist. Basierend auf diesen Ergebnissen, wird unter anderem das geodynamische Modell „konvektive Entfernung des lithosphärischen Material unterhalb einer ehemaligen über-verdickten Lithosphäre“ als höchstmöglicher, geodynamischer Tiefen-Mechanismus favorisiert, der das Untersuchungsgebiet geformt, deformiert und ausgeprägt haben könnte.

Chapter 1

Introduction

1.1 General introduction

There is abundant evidence suggesting that the Earth as a whole is a differentiated body and is inhomogeneous on many scales. But, it is extremely difficult to know about the Earth's interior by direct observations, due to its inaccessibility. Most of the knowledge of the deep interior of the Earth comes from a few **direct** observations (e.g., samples from deep mines, wells, volcanoes and meteorites). However, this knowledge is very limited, if one considers the actual Earth's dimensions, which has a diameter of 12756 km**:**

- The deepest mines in the world are only 3 to 4 km deep
  (e.g., TauTona Gold Mine, South Africa).

- The deepest well ever drilled by mankind only penetrates 12 km into the interior (e.g., Kola Superdeep Borehole, located near Murmansk, Russia).

- Volcanic and plutonic rocks provide samples of the Earth's interior from different depths in the mantle (e.g., Kimberlites and xenoliths).

- Finally, meteorites that fall to the Earth are also believed to be representative of the materials from the mantle and core of planets similar to the Earth.

In particular, the rapid increase of temperature below the Earth's surface is leading to limitations on direct observation inside the Earth through mining and drilling operations. Another technique to collect information about the Earth's remote interior by **indirect** ways consists in utilizing seismic, or earthquake waves. When an earthquake occurs, seismic energy is released, and P- and S-body-waves radiate in all directions from its focus. Consequently, seismic waves can travel through the entire Earth in any direction, being refracted, reflected, and converted (possibly mode-changed) for example from P-to-S, or S-to-P types, when they encounter a discontinuity (an interface between materials of different

elastic properties) within the Earth. A sensitive detector, called a seismograph, can record these various waves, whose arrival times are determined by the depth of the source and its epicentral distance.

Thus, the most direct knowledge available of the Earth’s deep interior is inferred from the analysis of the propagation characteristics (travel times, reflected or converted signals, dispersion, etc.) of seismic P- and S-waves. One of the most important aspects of seismology is concerned with measuring the speeds at which seismic waves travel through the Earth. There are several depths within the Earth at which seismic velocities and density dramatically change. This phenomenon is commonly attributed to a change in either the composition, physical state, or both, of the Earth's materials.

To detect and analyze the Earth's remote deep structures, Earth scientists are generally forced to develop indirect methods in which various types of geophysical or geological modeling are used. For this purpose, there are numerous approaches which are available to researchers (e.g., reflection seismic, seismic tomography, receiver functions, surface wave analysis etc.). Under some specific seismological assumptions, these techniques rely either on advanced forward or inverse modeling techniques.

The receiver function (RF) technique, having been influenced by the exploration seismics, is a well-established method in the field of observational seismology for extracting valuable information about the Earth’s internal structure. This technique exploits the waveforms obtained from distant earthquakes on the receiver side, and examines them in terms of refracted, mode-converted phases in order to explore the seismic deep structures lying beneath a seismic receiving device.

In the following sections, we will give a brief overview of the history of seismology and the discovery of the main structural units of the Earth.

1.2 Historical seismology

Establishing and developing seismology as a separate branch of natural science and discovering the Earth's major layers was a long-term process, to which many scientists from different countries have contributed. Let us now take a brief look at the historical development of this field into a modern science. At the early date 132 AD, the Chinese

scholar **Chang Heng** invented the first earthquake detector, a seismoscope. However, this device showed only the direction of incoming earthquake waves. The great Lisbon earthquake is generally accepted as an event that dramatically changed man's outlook on the phenomenon of earthquakes, and marks the beginning of the modern era of seismology. In 1875, **Filippo Cecchi** in Italy developed the first successful seismograph, an instrument that could detect and record the vibrations produced by an earthquake. In 1889, the science of seismology was revolutionized when a distant earthquake from Japan was recorded instrumentally by **Ernst von Rebeur-Paschwitz** at Potsdam and Wilhelmshaven for the first time. A prototype of a modern seismograph was developed in 1892 by **John Milne** and his associates in Japan.

R. Dixon Oldham first put forward in 1900 that there were three distinct wave phases corresponding with the P, the S and the L waves (he simply denoted them as the first, second and the third phases). He designated the first phase as "compressional" waves and the second phase as "distortional" waves, interpretations that remain valid today. Some of the first seismic travel time curves and tables were developed by **Oldham, Zoeppritz, Turner** and **Gutenberg** between 1906 and 1914. The first complete velocity model of the interior, using travel time, was introduced by **Jeffreys and Bullen** in 1940. The so-called Jefferys-Bullen tables are still occasionally referenced today (Jeffreys et al. 1940). The second revolution in seismology occurred between 1950 and 1955, when digital computers were first introduced. The ability to perform fast calculations increased the dimensionality of seismology both in space and time.

Developments of modern seismology since 1960s resulted in a large increase of seismological data, allowing scientists to develop several new velocity models with more accuracy. The preliminary reference Earth model (**PREM**) was the first one accounting for the anisotropy of wave velocity inside the Earth (Dziewonski and Anderson, 1981). Afterwards, the **IASP91** standard velocity model was developed in 1991 (Kennett and Engdahl 1991). Finally, the **AK135** model was put forth based on data from the International Seismological Centre (ISC) from 1964 to1987. This can be considered as an improved version of the IASP91 model (Kennett et al. 1995).

Past earthquake studies revealed that P-(primary/compressional)waves travel faster through the Earth, whereas S-(secondary/transverse)waves are slower and cannot pass through

liquids. This allowed scientists to recognize the Earth's layers known as the crust, mantle, and core. The disappearance of S waves below a depth of 2,900 km indicates that the outer core of the Earth is liquid. In the following section, we will give some information about the historical discovery of the Earth's main layers.

1.3 The discovery of the internal structure of the Earth

The layered structure of the Earth has been known fairly well from seismology since the beginning of the 20th century. Seismology teaches that the Earth is chemically subdivided into three basic sections: the crust, the mantle (subdivided into upper and lower mantle) and finally the core, that is differentiated into an outer and inner core. In addition to this classification, the Earth can be separated into layers based on mechanical properties, such as rheology. For this type of differentiation of the interior structures, the uppermost part of the Earth, encompassing the layers of the lithosphere and asthenosphere, is defined by the manner in which material at a given depth responds to forces that are exerted on it. Let us now take a closer look at the historical discovery of the Earth's major layers.

Henry Cavendish (1798) performed a series of experiments to calculate the Earth's density. Based on the results of this work, he estimated the average density of the Earth to be 5.48 times the density of water, a result quite close to the modern measured value of 5.53. On the basis of the density determination of Cavendish, **Emil Wiechert** (1896; 1897) claimed that the Earth’s density is too great for it to be composed solely of rock, and he drew the conclusion that the Earth might have a core made of iron metal, like the iron meteorites. Thus, he subdivided the Earth's interior into two main layers: a silicate shell surrounding a metallic core. To make it clearer, he presented a quantitative Earth model, proposing that the Earth has a dense iron core, which is surrounded by a lighter rocky layer, now called the mantle.

Around 1910, two seismological studies confirmed Wiechert’s claim experimentally, leading to the discovery of the Earth’s core. Firstly, **R. D. Oldham** (1906) supplied seismological evidence for the existence of a central core of an approximate radius of 1,600 km. He called attention to the fact that there is a substantial delay in the arrival of P-waves at angular distances beyond 120° from an earthquake epicenter. From this observation, he concluded that the Earth contains a central core in which the P-wave velocity slows down. He also

suggested that a specific region of epicentral distances (shadow zone) exists in which P-waves could not arrive. Based upon the findings of this study, it was also revealed that the mantle transmits P- and S-waves everywhere, and thus being solid for stress with periods not greatly exceeding tidal periods.

Beno Gutenberg (1914) investigated this phenomenon in some detail, confirming the presence of a shadow zone for P-waves in the range of epicentral distances between 105° and 143°. By analyzing records of earthquakes that had epicentral distances of over 80° from Göttingen, he located the core-mantle boundary with an impressive accuracy of about 2,900 km, where the velocity of longitudinal waves was reduced from 13.25 to 8.5 km/s. A modern estimate of the radius of the core is 3,485 km, while the mantle is 2,885 km thick. Furthermore, Gutenberg also suggested that S-waves, being transverse, cannot be transmitted trough liquids and are therefore could not be present beyond 105°. From this fact, he concluded that the Earth's core must be liquid. Finally, Gutenberg prognosticated that P- and S-waves would be reflected from the core-mantle boundary, known today as PcS and ScS waves. The core-mantle boundary today is also called the Gutenberg seismic discontinuity, after its discoverer. Thus, the core was the first internal structural element of the Earth to be identified.

Andrija Mohorovicic (1909) discovered a sharp material discontinuity at some level under the Balkan peninsula. While analyzing the P-wave arrivals from an earthquake near Zagreb, he observed only a single arrival Pg at distances close to the epicenter. In contrast, beyond about 200 km, he detected two arrivals, Pg and Pn, whereby the Pg arrival is overtaken by the Pn events which had to travel trough a medium (the upper Mantel) that permitted them to speed up. Mohorovicic identified Pg as the direct wave and Pn as a double refracted wave which travelled partly in the upper mantle. Mohorovicic computed velocities of 5.6 km/s for Pg and 7.9 km/s for Pn, and found out that a sharp increase in the P-wave-velocity occurred at a depth of 54 km below the Earth's surface. Seismological studies done later indicated such an increase to be applicable worldwide, and this boundary is to be found throughout the Earth at an average depth of 35 km below the surfaces in continental shield areas. The depth of this discontinuity can reach 70 km under some mountain ranges, and can be as little as approximately 5 km below the floors of deep oceans. Similarly, this boundary is called the Mohorovicic discontinuity (Moho), after its discoverer. Being the lower

boundary (base) of the Earth's crust, the Moho represents the boundary between the crust and mantle.

The terms lithosphere and asthenosphere were first proposed by **Joseph Barrel** (1914). He spoke of an upper, rigid lithosphere, and a lower more plastic asthenosphere, and placed the boundary between the two at 100 km.

Beno Gutenberg (1926) postulated a seismic low-velocity zone (LVZ) in the upper mantle at a depth of about 100-200 km, pointing out that seismic waves from hypocenters (foci) with depths of 50–250 km took longer to arrive than expected. He supported his claim with his later works, giving a depth of 80 km of his low-velocity zone (Gutenberg and Richter 1939; Gutenberg 1948, 1954, 1959). At that time, he also speculated that this low-velocity layer corresponded to a zone of decoupling of horizontal motions of the shallower parts from the deeper parts of the Earth, as proposed by Wegener (1912). It was later recognized that the presence of an upper mantle LVZ was of revolutionary significance for mantle dynamics in terms of plate tectonic concepts (Wilson 1965; McKenzie and Parker 1967), providing a relatiely low-viscosity region (asthenosphere) upon which lithospheric plates can move with very little friction. In honour of Gutenberg, the lithosphere-asthenosphere boundary is sometimes called today the Gutenberg discontinuity. Nowadays, the low-velocity zone is generally equated with the relatively-weak asthenosphere, underlying the outermost rigid shell of the Earth, the so-called high-velocity lithosphere. It is broadly accepted that this zone is characterized by low seismic wave velocities, high seismic energy attenuation and high electrical conductivity. These observations are generally interpreted to mean that the upper mantle at those levels must be partially molten, probably one percent or less.

Inge Lehmann (1936) proposed the presence of an inner core in order to explain the amplitudes of P waves between angular distances of 105° and 143°, which were previously thought to be diffracted waves. The improvements made in terms of sensitivity of seismographs in the 1930s made it possible to see previously undetectable seismic waves within the P-wave shadow zone. Whilst analyzing a large earthquake in detail that occurred near New Zealand, Lehmann recognized that even the P-wave shadow zone was not completely free of the P waves, and weak arrivals of longitudinal waves (P) were detectable there. According to Lehmann, these waves should have travelled some distance into the core and bounced off (deflected) some kind of boundary before being recorded at seismic

stations. From this fact, she deducted that the core itself was homogeneous, and might be subdivided into a solid inner core surrounded by a liquid outer core, which is separated by a discontinuity. This transition zone, sometimes called the Lehmann Discontinuity, separates the outer and the inner core at a depth of about 5,000 to 5,100 km. The radius of the inner core was found by B. Gutenberg (1938) and by H. Jeffreys (1939) to be about 1,200 to 1,250 km.

H. Jeffreys and K.E. Bullen (1940) introduced a velocity model of the internal structure of the Earth, which consisted of seven concentric shells. In their models, they integrated a change of velocity gradients at a depth of 413 km. This rested upon the so-called 20° discontinuity, which was first theorized by **Byerly** (1926) from the travel time studies of P-waves from the Montana earthquake of June 28, 1925. Thus, they separated the mantle into two major parts: the upper (Layer B : 33-413 km) and lower one (Layer D : 984-2,400 km) by defining the transition region of the mantle as a diffuse region of high seismic-speed gradient, extending from 413 km to 984 km (Layer C). However, the detailed structure of the transition zones became more clear only in the 1960s. From the surface wave studies, it was inferred that the transition region was not a broad 600 km thick zone and that the upper mantle low velocity zone (the base of the asthenosphere) was globally underlain by the two strong positive velocity gradients, located at approximately 350-450 km and 600-700 km depths (Anderson and Toksöz, 1963; Töksöz and Ben-Menahem, 1963; Toksöz and Anderson, 1966). In later years, body waves recorded by large seismic arrays (1,000-3,000 km distance range) were used to refine the velocity depth for the mantle transition zones. It turned out that the two major upper mantle travel time triplications are generated by abrupt P- and S-velocity increases near the 410 and 660 km depths (Niazi and Anderson 1965; Johnson 1967; Kanamori 1967).

One of the main tasks of modern seismology consists in resolving the lateral heterogeneity in the Earth. This research is concerned with the detection of possible discontinuities in the Earth's crust (Moho) and in the upper mantle above a depth of 700 km (LAB as well as 410 and 660 km) beneath the westernmost Mediterranean Sea region and the surroundings, using PRF- and SRF-techniques. Nowadays, it has been widely recognized that the exact knowledge of such seismic velocity structures could provide valuable clues to the dynamics of the Earth’s deep interior processes, which in turn may be helpful in revealing of the tectonic evolution of a geological region in terms of plate tectonic concepts. Accordingly, the

findings from such studies are used as a basic step for testing and developing models for the kinematic evolution of a tectonically active region.

1.4 Purpose of this study

The westernmost Mediterranean region, i.e., the Alboran Sea basin and the surrounding land areas, developed into its present state through the complex and continuous interactions between two main lithospheric plates, namely the Eurasian/Iberian and the African plates. Corresponding to the western part of the Eurasia-Africa plate boundary, the area under investigation is of great seismological and tectonic interest. Although the tectonic settings of this region have been extensively investigated by means of geological and geophysical methods since the beginning of the 1970's, different conclusions have been reached, and the driving crustal and mantle tectonic processes, which are responsible for the geological evolution of this area have remained ambiguous up to now.

Information on the internal structure of the Earth on various scales is of fundamental importance in understanding the past and present geodynamic-dominated state for a tectonically complicated region. In this context, great emphasis is especially placed on the knowledge of the seismic subsurface structures from the crust (Moho) to the upper mantle transition zone discontinuities at 410 km and 660 km depth, including the uppermost mantle discontinuity, known as the lithosphere-asthenosphere boundary (LAB).

A precise definition of the topographic variation of such deep velocity structures is commonly considered to be important, since knowledge of them may contribute strongly to understanding the geodynamic evolution of an area within the framework of plate tectonics. For this reason, the main aim of this dissertation is to outline and map the deep key seismic structures, as mentioned above, beneath the westernmost Mediterranean Sea region and surroundings, by making use of the well-known PRF- and SRF-techniques applied to large volumes of data.

Another aim is to test the validity of the available hypotheses, which have been postulated in explaining the geodynamic evolution of the area under study. This includes setting up appropriate boundary conditions to develop more comprehensive geodynamic models for the region.

Chapter 2

Geology of the area of study

2.1 General overview of the whole Mediterranean Region

If one considers the Mediterranean region on a large-scale, the geodynamical evolution of this area is characterized by the ongoing collision between the African-Arabian and Eurasian plates, as indicated in figure 1. This feature is evidenced in the area by the formation of several orogenic belts, such as the Betics, the Magrebides (Rif and Atlas mountain chains), the Apennines, the Alps, the Carpathians, the Dinarides-Hellenides, Taurus, etc. In spite of convergence acting as the primary plate-tectonic process, the whole area hosts several regions, whose tectonic settings are dominated by large scale extension, such as the Alboran Sea, the Algero-Provencal and Tyrrhenian Sea basins, the Pannonian basin, and the Aegean region (Mckenzie 1972, Dewey 1973, Horvarth et al. 1982, Joliet et al. 1999, Durand 1999).

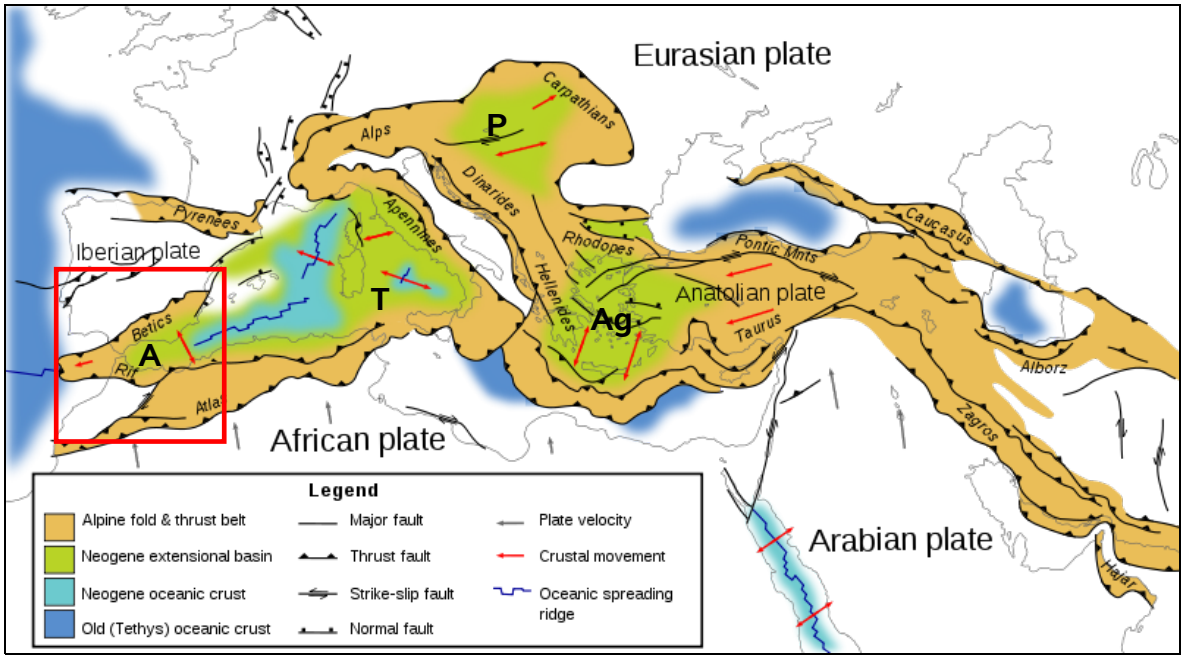

Figure 1: Tectonic Map of the Mediterranean Region. The opening of the Aegean and Tyrrhenian basin are related to the subduction retreat processes. The origin of the Alboran and Pannonian basin is controversial. Abbreviations: A: Alboran basin; Ag: Aegean basin T: Tyrrhenian basin; P: Pannonian basin. (adopted from http://en.wikipedia.org/wiki/File:Tectonic_map_Mediterranean_EN.svg and modified).

Generally, there is a broad consensus about the geodynamic evolution of the central Mediterranean and the Aegean region. For instance, the Aegean and Tyrrhenian basins are commonly thought to be back-arc basins, and their rapid opening is related to the subduction retreat processes. On the other hand, the other basins such as the Pannonian and the Alboran have formed in essentially intracontinental settings, and their tectonic evolution is highly complicated and still hotly debated. Within the framework of this research, the main focus is on the westernmost Mediterranean region, encompassing the Alboran Domain and the surrounding regions, including the southern parts of the Iberian Peninsula (e.g., Betic chain, South Spain and Portuguese Zone), and the collisional belts of the north-western Africa (Rif and Atlas mountains). Finally, an attempt will be made to contribute to a better understanding of the tectonic evolution of the area of interest, using the RF technique. The area investigated is marked with a red box on the map in figure 1.

2.2 General overview of the target area

The westernmost Mediterranean region is a very interesting and complex area from the structural and tectonic point of view, mainly due to its geodynamical location between the converging Eurasian (Iberian) and African plates. This region accommodates both juxtaposed compressional and extensional zones (Betic, Rif, and Atlas Mountains as well as an Alboran Basin) within a convergent geodynamic setting, thus giving researchers a unique opportunity to investigate the contrasting tectonic processes in an overall convergent setting.

Dominated on a large scale by the continent-to-continent collision between Africa and Eurasia in southern Iberia and northern Morocco, the whole zone is affected by shallow and intermediate depth seismicity, despite the fact that some deep earthquakes of great magnitude have taken place near the Spanish city of Granada. The geodynamic evolution of the area is still controversial and the focus of widespread debates.

The most popular geodynamic scenarios proposed and propounded in the recent literature, are as follows: (1) backarc extension driven by the westward rollback of an eastward-subducting slab (Morley 1993; Royden 1993; Lonergan and White 1997; Michard et al. 2002). This model is also supported by the tomographic studies done on the Alboran region by Gutscher et al. (2002) and Spakman and Wortel (2004). (2) Radial extensional collapse

of an earlier collisional Betic-Rif orogen, caused by a convective removal of deep lithospheric roots (Platt and Vissers 1989; Houseman 1996). (3) Slab detachment and delamination of the lithospheric mantle (Garcia-Duenas et al. 1992; Comas et al. 1992; Docherty and Banda 1995; Seber et al. 1996; Calvert et al. 2000). (4) Subduction and breaking of a slab material (Zeck 1996).

Despite the relatively large amount of geological and geophysical studies conducted in this area during the last decades, still little is known of the deep crustal and mantle structures in this area. The main objectives of this study are (1) to investigate and discuss the general deep-seated velocity structures of the western Mediterranean region and surroundings through the analysis of teleseismic data, using the receiver function technique, and (2) to shed light on the geodynamic evolution of the area of investigation. In particular, the study of the crustal-mantel velocity structures (e.g., Moho, LAB, and upper mantle discontinuities (410-, 660 km)) constitutes the main focus of this research project, whose detailed information is essential to better understand the past and present tectonic evolution of the whole area.

2.3 Geological setting

The historical opening of the Central Atlantic and the Western Tethys plates during the Middle Jurassic (176 Myr ago), and the African-Eurasian-convergence since the late Cretaceous (92 Myr ago) have been the most important geological events which have played a prominent role in the tectonic evolution of the western Mediterranean (e.g., Schaer 1987; Bortolotti et al. 2005; Dewey et al. 1989). The region is presumed to have hosted approximately 150-170 km of plate convergence between the Eurasian and African plates since then (e.g., Dewey et al. 1989). The area of study experienced a major change during the Late Oligocene (around 25 Myr ago), when the prior dominance of northward subduction of the Neo-Tethys was replaced by the first stages of continental collision. Finally, the interaction between the Iberian and African plates in the westernmost Mediterranean region led to the opening of the Alboran Sea basin and forming of the Betic-Gibraltar-Rif orogenic system, and the Atlas Mountains, whose structurally and evolutionary framework is particularly complex (figure 2). The almost coeval geological evolution of the extended Alboran Sea and the shortened mountain range within the Eurasia-African collision zone cannot be easily explained in terms of plate tectonic mechanisms alone.

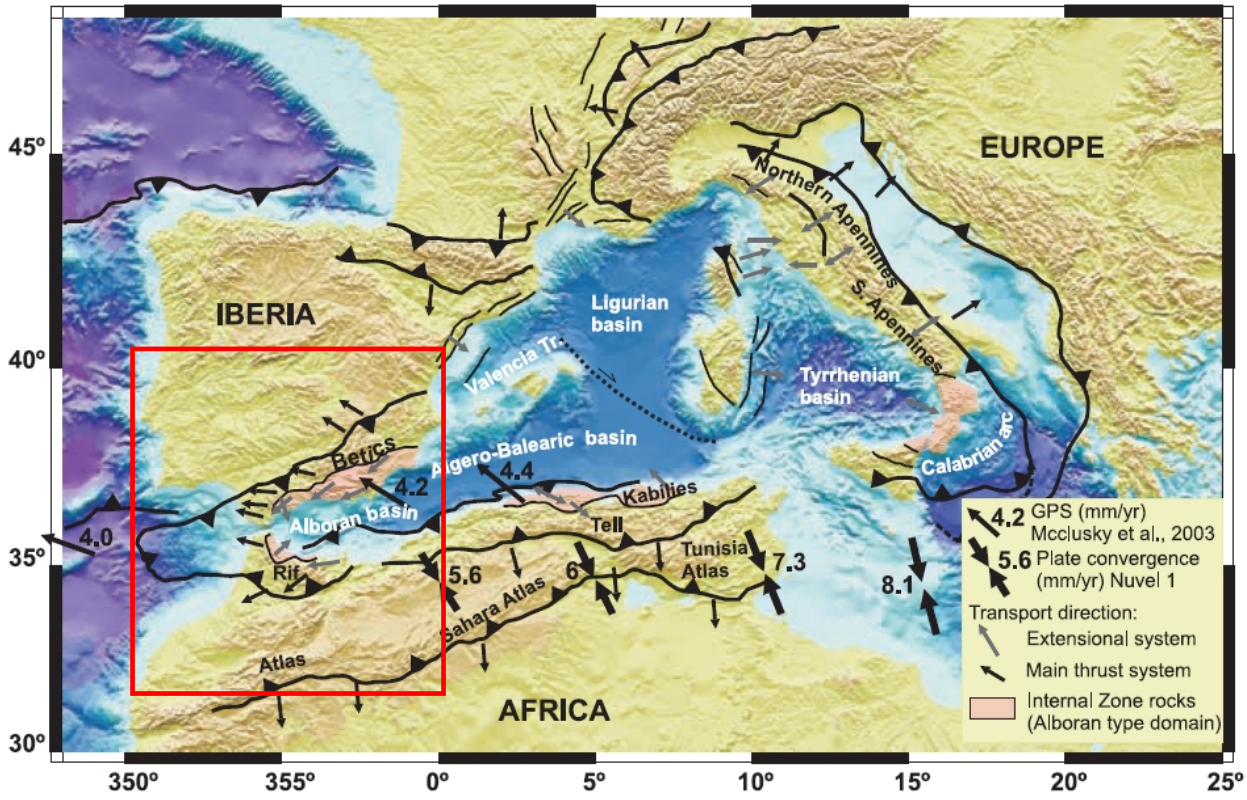

Figure 2: Map showing the principal tectonic features and zones of deformation of the Africa-Eurasia plate boundary in the western Mediterranean (modified from Booth-Rea et al. 2007). Red box outlines the subject area which is characterized by the ongoing collision between the African and Iberian plates, and includes the main tectonic features „the extensional Alboran basin“ and „the compressional Atlas, Betic-Rif Cordilleras“. The arrows indicate the type of stress field and main directions, and numbers the GPS-derived velocities in mm/yr after McClusky et al. (2003) and Nuvel 1 (DeMets et al. 1990; 1994). The open question related to this area is: “how was the extensional Alboran basin able to develop within a convergence setting, which is surrounded by the contractional Atlas, Rif-Betic Cordilleras?”.

In contrast, it is important to note that there is a broad consensus about the geodynamic evolution of the central Mediterranean region. It is generally thought that this area was mainly shaped by the migration of a slab associated with a west-directed subduction during the Neogene within the framework of steady convergence of African and Eurasian plates. Within this context, the Ligurian and Tyrrhenian basin are generally considered as extensional back-arc basins generated by retreat of the Apenninic slab during the eastward-migration of Apenninic and Calabrian arc.

The main structural provinces in this area are shown in figure 2 and can be distinguished from north to south, the southernmost part of the Iberian Peninsula (southernmost part of Spain and Portugal), the easternmost area of the Atlantic Ocean (Gulf of Cadiz), the western portion of the Mediterranean Sea (Alboran Sea), and the north-western area of Africa (basically Morocco). The remarkable surface structures are the Betic Mountains in southern Spain, the Rif and the Atlas Mountains (High, Middle) in northern Morocco. According to the Nuvel-1 plate motion model (DeMets et al. 1990; 1994) for this region, the African plate is moving northwest relative to Eurasia at a rate of 4-6 mm/yr.

The Neogene extensional Alboran Sea basin is one of many Mediterranean basins, and was formed during Oligo-Miocene times whilst the African plate moved northward with respect to Eurasia. (Dewey et al. 1973). This narrow rift basin has an east-west trending horst and graben morphology (Dillon et al. 1980), and is underlain by a thin, highly metamorphosed continental crust which underwent large amounts of extension and rapid exhumation in the Late Oligocene - Early Miocene era (Watts et al. 1993). The Alboran Sea is characterized by a complex bathymetry with a water depth of less than 2 km, where two main basins can be distinguished: the Western Alboran Basin and the Eastern Alboran Basin. These basins are separated by the SW-NE-trending Alboran Ridge. A thick (early Miocene to recent) sedimentary cover fills the basin beneath the sea, resulting from the early Miocene extension in the basin (Comas and Jurado 1990). Multichannel seismic reflection profiles and commercial well data conclude that the West Alboran Basin is characterized by major sedimentary accumulation (up to 8 km thick), whereas sediments are probably less than 4 km thick in the Eastern Alboran basin. Basement rock samples, from the Ocean Drilling Program (ODP) site 976, show that the foundation beneath the Alboran Sea consists of continental crust (Platt et al. 1996). The crustal structure of the Alboran Sea is similar to that of the internal zone of the Betic and Rif cordillera, and they together make up the Alboran Domain.

The Betic Cordillera in southern Iberia and the Rif in northwestern Africa are arc-shaped orogen, forming the westernmost end of the **Alpine orogenic belt** in Europe. They constitute the northern and southern segments of the Gibraltar arc which forms the western boundary of the Alboran Sea. Those thrust-and-fold belts were formed from crustal shortening when the Iberian continental margin was involved in Alpine orogeny. Both **the Betic and Rif systems** comprise three main structural domains, commonly known as the

Internal Zones, the Flysh Nappes, and the External Zones. The internal zones of Betic-Rif orogen are common to both cordilleras, and are made of stretched and thinned continental crust, which is composed of Paleozoic to Mesozoic rocks of low-to-very-high grade metamorphism that were deformed mainly during the Late Cretaceous to Paleogene period. Subsequently, they were thrust onto the margins of Southern Spain and Northern Morocco during the early Miocene (Lonergan and White 1997). It is generally believed that the autochthonous internal zones of the Betic and Rif regions are the dismembered remnants of an early Alpine collisional system that evolved through the latest Oligocene or earliest Miocene (e.g., Rehault et al. 1985). **The Flysch Nappes** are Cretaceous to Oligocene deepwater turbidites that were emplaced as nappes onto margins of Spain and Morocco during the Early Miocene period (Lonergan and White 1997).

The Betic and Rif external zones are characterized by a thin-skinned fold-and-thrust belt composed of Mesozoic to Tertiary continental margin strata, which underwent continual deformation from Miocene to Early Pliocene times period (Lonergan and White 1997). Calc-alcaline volcanism in the area occurred from 18-8 Ma, followed by high-volcanic activity from 9-4 Ma, and alkali-basalts (5-1 Ma) (Gomez et al. 2000).

To the north, the Betics Cordillera is separated from the Iberian Massif by the Guadalquivir foreland basin. A large area of the central and western Iberian Peninsula is covered by the Variscan Iberian Massif, a large, old and geologically stable block of continental lithosphere (Dallmeyer and Martinez Garcia 1990), which is tectonically less complex than the rest of the area of study. On the other hand, the Rif is separated by the Gharb foreland basin from the Moroccan Meseta to the south. This is in large part equivalent to the Iberian Massif.

Spanning more than 2,000 km and attaining elevations of up to 4 km, the Atlas Mountains in the northwestern Africa can be viewed as the southernmost product of the Iberian-Africa plate boundary. They were formed in a convergent tectonic regime during the Oligence-Miocene time within the Proterozoic-Paleozoic Sahara (African) platform (Gomez et. al 1998). It has been traditionally regarded as intracontinental in nature and differentiated from interplate Betics and Rif mountain belts by their distance from the collisional zone and their lack of Nappe structures, ophiolites, regional metamorphism, and granitoid intrusions. The Atlas Mountains are typically subdivided into the High Atlas and Middle Atlas of Morocco and

the Saharan Atlas of Algeria. Two large crustal blocks are situated north of the High and Saharan Atlas: the Moroccan Meseta to the west and the High Plateau to the east.

2.4 Regional seismicity

The seismicity of the study region is mainly triggered by the NW-SE convergence (4-6 mm/yr) between the African and Eurasian plates (DeMets et al. 1990; 1994). Figure 3 shows the distribution of epicentres of regional earthquakes with magnitudes ≥ 3 during the instrumental period from 1900 to 2010. As can be easily seen, the present-day seismicity is widely spread along the southern Iberian Peninsula, in the Betic Cordillera, in the Alboran Sea, and in the Rif and Atlas Mountain ranges, whereby it is virtually impossible to identify the plate boundary trace in this area. Seismicity of the Iberia-African region is generally marked by the occurrence of small and moderate earthquakes. Most events correspond to shallow shocks with a magnitude of less than 5.5. Most of the hypocenters are located in the crustal domain in the depth range 0-33 km. However, there is a great number of events with depths between 33 and 150 km present, which are mainly situated in the western Alboran Sea between 3.5°W and 5°W. These define a narrow N-S trending band. At the western side of the Gibraltar Arc, from the Gulf of Cadiz to the Gorringe bank region, intermediate-depth shocks are spread over a band approximately 100 km wide, extending E-W from 8°W to 10°W. No intermediate depth seismicity is observed east of 3°W in Spain or Morocco. In addition, five deep earthquakes have been registered, all with depths between 600 and 635 km. They are clustered together with epicenters located south of the city of Granada in Spain. The first event registered in 1973 has been assigned a magnitude of 4.0 whereas the others have magnitudes of 4.1, 3.9, 2.1, and 6.3, respectively. These deep earthquakes are commonly related to fractures in a detached fragment of cold and rigid plate that is sinking into the deep mantle (e.g., Platt and Vissers 1989; Blanco and Spakman 1993; Zeck 1996). In the Atlas Mountain range, which is located south of the Rif mountains, the present-day seismicity is rare. North of the Betic Cordillera, the Hercynian Iberian Massif is internally influenced by the Alpine deformation, but is relatively seismically inactive.

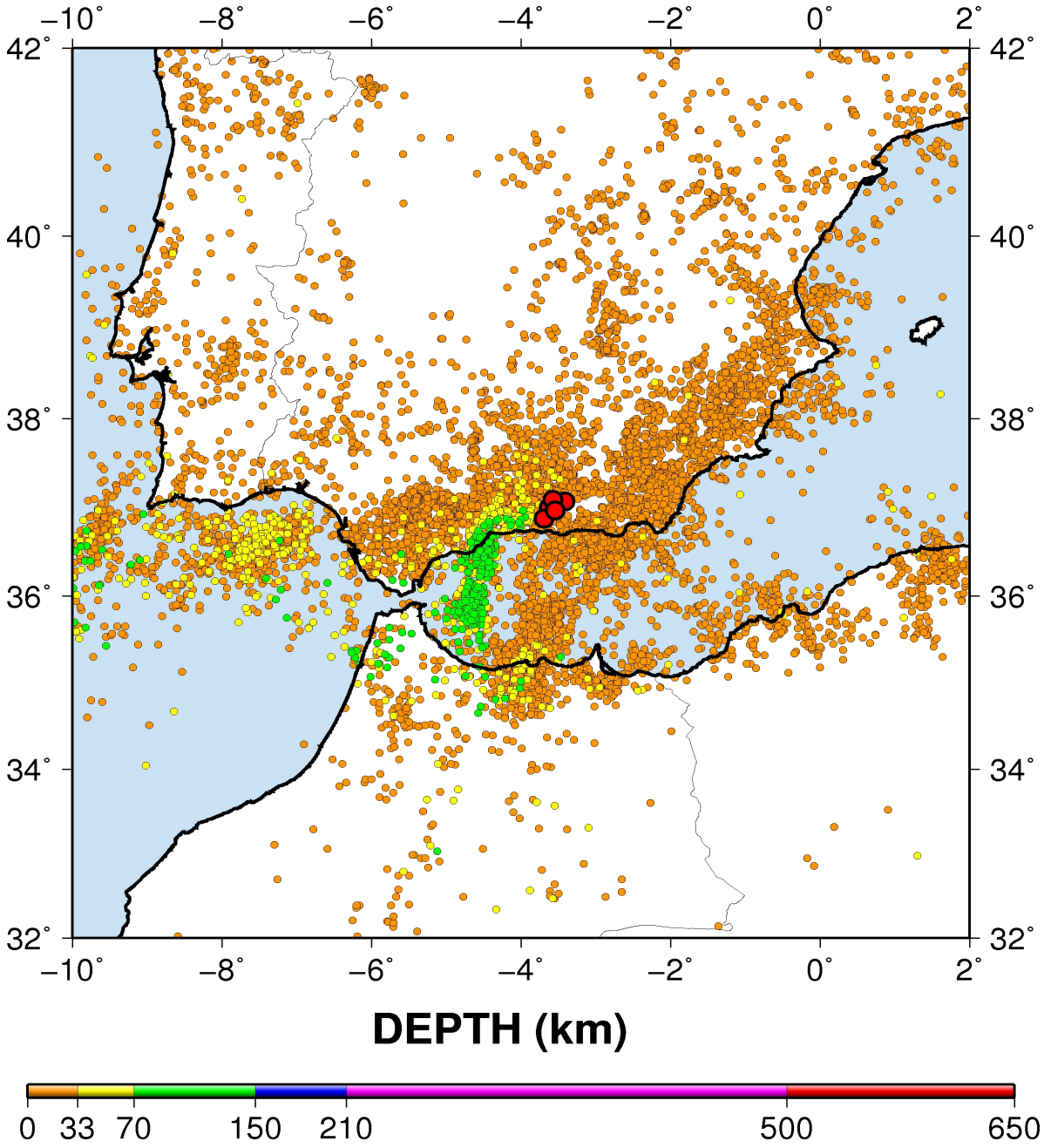

Figure 3: Seismicity map of the western Mediterranean region and the surrounding area. The circles indicate the location of events with a magnitude greater than or equal to 3 for the period 1900-2010. The earthquakes are extracted from the USGS/NEIC catalog. The regional seismicity is diffuse and does not clearly delineate the present-day plate boundary. A number of large recent events occurred in the area of study, including the 1964 March Gulf of Cadiz (Ms=6.4), the 1969 February 28 Horseshoe (Ms=8.0), and the 2004 February 24 Al-Hoceima (Ms=6.4) earthquakes. The region also suffered the Lisbon earthquake of 1755 , which was believed to have occurred along the Azores-Gibraltar fracture zone in the Atlantic Ocean, about 200 km WSW of Cape St. Vincent.

2.5 Previous studies of the crust, mantle and lithosphere

Geophysical studies since the early 1970's have provided insights into the deep structures of the crust and upper mantle of the Alboran Domain in the westernmost Mediterranean and the surrounding regions. These studies have indicated that important lateral heterogeneities exist in the crust and upper mantle of this region. The most important finding from those surveys relevant to the present work is that both the crust and the mantle lithosphere are strongly thinned under the Alboran Sea basin with regard to the outer region of the compressional front. An overview of these studies, including their methodologies, is summarized below:

1) Seismic refraction studies and two dimensional gravity modeling reveal distinct differences between the crust and upper mantle of the Alboran Sea basin and surroundings (WGDSSA 1978; Hatzfeld 1980; Banda and Ansorge 1980; Medialdea et al. 1986; Torné and Banda 1992; Banda et al. 1993; Watts et al. 1993; Galindo-Zaldívar et al. 1997; Comas et al. 1997; Booth-Rea et al. 2007). The most remarkable results of studies can be summarized as follow:

a) Being of continental character, the crust beneath the Alboran Sea has a minimum thickness of 16 km, and thins towards the east and is finally oceanic beneath the Algerian Basin, while an abrupt change in crustal thickness is observed in the central Betic and Rif Cordilleras (about 35-38 km).

b) The crust reaches a thickness of up to 35 km in the Strait of Gibraltar, whilst towards the eastern Betics Cordillera there is a decrease in crustal thickness (about 20-24 km).

c) Banda et al. (1981) obtain a crustal thickness of 32 km with an average velocity of 6.34 km/s for the central Spain.

d) The crust of the Alboran Sea lies over an anomalous mantle with a reduced propagation velocities, ranging from 7.6 to 7.8 km/s, whereas the crust of central Betics and Rif cordilleras lies over a normal mantle (Hatzfeld 1978).

In regard to the observations of the above-mentioned and other authors, two schematic cross sections were designed in order to show the lateral variations of the east-west and north-south crustal structure along the Alboran Domain, as seen in the works of Comas et al. 1999 (figure 4).

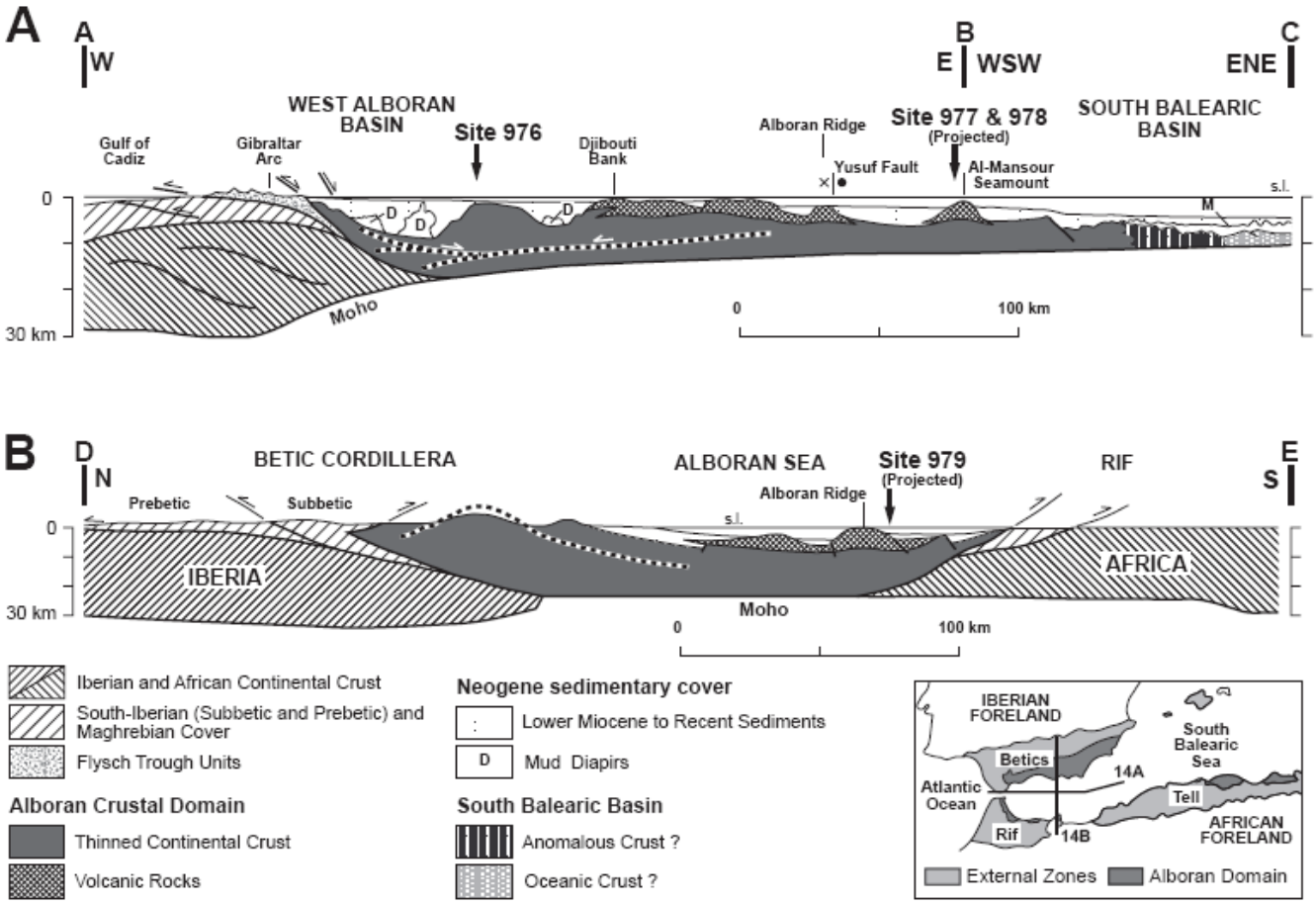

Figure 4: Cross-sections of the Alboran Domain (adopted from Comas et al. 1999). **(A)** Section longitudinal to the Alboran Domain (W-E-ENE). **(B)** Section perpendicular to the Alboran Domain (N-S). The main observation is a strong variation in the crustal thickness beneath the Alboran Sea and the surrounding region (e.g., Betic Cordillera). The Basin is underlain by thin continental crust (15-20 km).

2) The structure of the crust in the Iberian Peninsula, especially in the Hercynian of the central and southern Portugal, including the South Portuguese basin, is derived from a large number of seismic refraction and wide-angle reflection experiments (e.g., Müller et al. 1973; Sousa Moreira et al. 1978, 1983; Mendes Victor et al. 1980; Palomeras et al. 2008).

The principal outcome of these studies shows that the area is characterized by an average crustal thickness of approximately 30 km, with strong variations between 25 km under the Tagus Valley and up to 34 km in the South Portuguese zone. They also give an estimate of the average velocity of the crust, ranging between 6.15 and 6.30 km/s.

3) More recently, Diaz et al. (2009) have recompiled results of the published wide-angle and multichannel seismic profiles that provide information about the whole crustal structure under Iberia and the surrounding areas (figure 5).

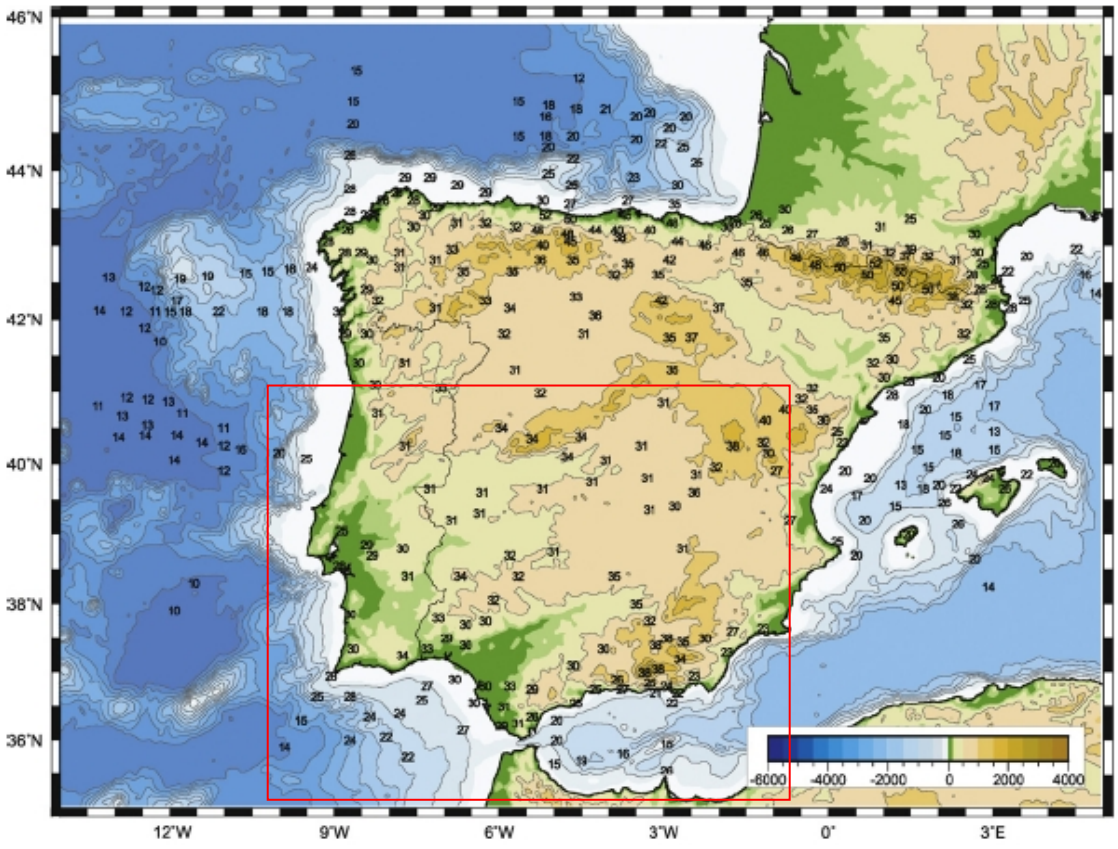

Figure 5: Recompilation of the crustal depth thickness by Diaz et al. (2009), based on published deep seismic sounding profiles.

4) The seismic refraction and gravity studies in Morocco provide the most valuable constraints on the crustal structure of the Rif, Middle and High Atlas Mountains. These studies point out that the Moroccan crust is relatively thin (~30 km) beneath the Rif and

Middle Atlas, and reaches its maximum thickness beneath the High Atlas (~40 km) (Demnati 1972; Schwarz and Wigger 1988; Wigger et al. 1992).

5) Using surface wave data, Badal et al. (1992), and more recently Martinez et al. (2005) have suggested that the top of the asthenosphere is located 80 km below the surface throughout the Iberian Peninsula.

6) Polyak et al. (1996) suggest a general increase of the thermal regime along the Alboran Sea from west to east, after analyzing the heat flow data. Additionally, they confirm the oceanic nature of the crust as well, based upon the data in the Algerian Basin.

7) Back stripping (Docherty and Banda 1995) and shear wave attenuation along with 3D gravity modeling (Seber et al. 1996a) indicate the presence of asthenospheric material at subcrustal levels.

8) The tomography studies (e.g., Seber et al. 1996b; Bijwaard et al. 1998; Calvert et al. 2000; Primallo and Morelli 2003; Faccenna et al. 2004; Spakman and Wortel 2004) detect a low velocity anomaly (warm material) in the upper mantle beneath the Alboran Sea, but a high velocity (cold body) anomaly in deeper levels (ca. 600 km depth).

9) The recent integrated lithospheric models along 2D profiles point out a rather flat lithosphere-asthenosphere boundary along the SW Iberian margin (Fernandez et al. 2004), and a considerable thickening of the lithosphere beneath the Gulf of Cadiz (Zeyen et al. 2005).

10) The geoid (Fullea et al. 2006) and the gravity modeling (Torne et al. 2000) studies indicate a thin lithosphere (between 60-90 km) beneath the Alboran Sea; it is as thick as 130-160 km under Gibraltar Strait (Iribarren et al. 2007).

11) Using a combined data of elevation, gravity, geoid, surface heat flow, and seismic data, Fullea et al. (2010) model the crustal (6A) and lithospheric (6B) structure for the Gibraltar Arc System, Atlas Mountains and adjacent zones, as shown in figure 6.

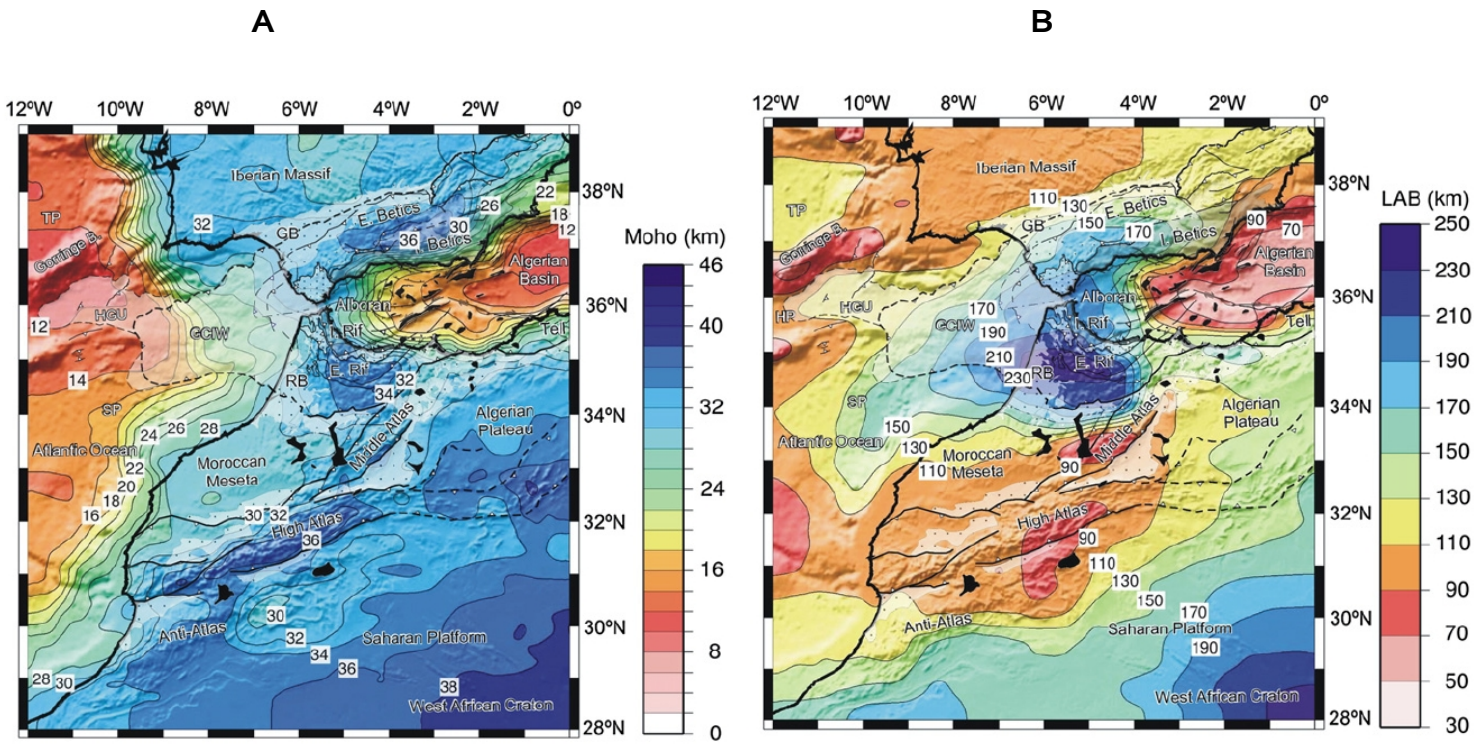

Figure 6: Crustal (**A**) and lithospheric (**B**) structure deduced by Fullea et al. (2010) from the integration of elevation and geoid anomaly data with a thermal field.

2.6 Geodynamic models

The area of study is situated in a complex tectonic setting and the exact details surrounding its geodynamic evolution are still being hotly debated. A wide variety of geodynamic models have been postulated to explain how the extensional Alboran Domain and the contractional structures (Betics, Rif and Atlas Mountains) may have evolved in a convergent tectonic setting, in relation to the interference of the African and Iberian plates. No single model can adequately explain or account for all of the geological features observed within the western Mediterranean. Several authors have presented various geodynamic models to explain the genesis and the tectonic evolution of the subject area (figure 7):

1) Rapid westward motion of a rigid Alboran microplate model is put forward by some authors in order to explain the build-up of the Betic and Rif cordilleras. In this model, the internal Zones of the Betic and the Rif cordilleras are viewed as belonging to a mobile Alboran domain. According to this model, the Alboran microplate collided with Europe and

Africa during its westwards displacement/migration, and thrusted over the South Iberian and the north African Margins, resulting in the formation of orogens (e.g., Andrieux et al., 1971; de Smet, 1984; Leblanc and Oliver, 1984).

2) Ryoden (1993) and Lonergan and White (1997) support this model and propose the slab rollback model, in which the opening of the Alboran Sea is related to the westward rollback of a east-directed subducting slab. They assume that this subduction is taking place west of the Gibraltar arc in the Atlantic, in the contact zone between the Iberian and African plates. The main difference between the models suggested by the above-mentioned authors lies in the origin of the slab. Whilst Lonergan and White's model assumes the roll-back of an ancient subducting slab, Ryoden's model suggests the rollback of a slab originating from the detachment of a sinking lithosphere.

3) Another subduction-related model is proposed by Morley (1993), envisaging a northward-dipping subduction located along the African Margin.

4) Sustaining this view, a sinking slab model is suggested by Zeck (1996, 1997) to explain the Alpine Betic–Rif orogeny. He relates the extensional tectonics on the surface with a existence of a broken subducted sheet as well.

5) Convective removal of a lithospheric root beneath a previous over thickened crust is proposed by several authors to be the cause for the underlying mechanism for the geodynamical evolution of this region (e.g., Wijermars 1985, 1987; Doblas and Oyarzun 1989a, b; Platt and Visser 1989). They take as a starting point the fact of the formation of a large dome and later extension-related lithospheric thinning in the Alboran Sea. Variations in Africa-Eurasia convergence rates are suggested to explain the alternating episodes of extension and compression.

6) Without rejecting other models, Houseman (1996) is of the opinion that the convection model provides the best explanation.

7) Asymmetric delamination of the lithospheric mantle model is propounded by several authors (e.g., Garcia-Duenas et al. 1992; Watts et al. 1993; Docherty and Banda 1995; Seber et al. 1996, Mezcua and Rueda 1997; Buforn et al. 1997). This model is very similar

to the convective removal hypothesis. The main difference is how the thickened lithosphere was removed**:**

a) Garcia-Duenas et al. (1992), Watts et al. (1993) and Docherty and Banda (1995) relate the geodynamic evolution of the Alboran Sea to the lithospheric delamination process. In such model, the subcrustal lithosphere detaches from the overlying crust and peels away, exposing subcrustal depths to hot asthenospheric material. Based on regional subsidence analysis, Docherty and Banda (1995) propose an eastward migration of the basin duo to a possible south-eastern position, thereby propagating lithospheric delamination.

b) Inferred from the tomographic study, Seber et al (1996a, b) claim that a lithospheric body, rooted 350 km deep under a part of northern Morocco, the Alboran Sea and Betic Cordillera exists. Its sinking was possibly due to a delamination process.

c) Mezcua and Rueda (1997) relocate the records from 1950 to 1995 in the Alboran Sea, Gulf of Cadiz, Betic Cordillera and Rif, and draw the conclusion that the delamination process would be the best fitting model to explain the intermediate and very deep seismicity of the region.

d) Buforn et al. (1997) report the existence a vertical sheet situated between Malaga and Granada and the West Alboran Sea which probably evolved as a result of a lithospheric delamination process and extends from approximately 50 to 150 km depth.

e) Based on the analysis of the origin of the intermediate earthquakes in the W-Alboran Sea, Morales et al. (1997) conclude the existence of a delamination process which spread westwards.

8) Morales et al. (1999) suggest a southward-directed subduction beneath the Betic Mountains, inferring from a tomographic study.

9) Other tomographic studies reveal a narrow east dipping slab (100-200 km wide) located in the Gibraltar Arc (Bijwaard and Spakman 2000; Calvert et al. 2000; Gutscher et al. 2002; Spakman and Wortel 2004), supporting the geodynamic models that were proposed based

on subduction rollback (Morley 1993, Royden 1993, Lonergan and White 1997, Michard et al. 2002).

10) By performing shear wave splitting analysis from SKS, Buontempo et al. (2008) and Diaz et al. (2010) suggest a rotation of the polarization direction of the fast split SKS waves following the curvature of the Betics and Gibraltar Arc. From their results, they favor the slab rollback model rather than the delamination model.

11) On the basis of global positioning system (GPS) measurements, McClusky et al. (2003), Fadil et al. (2006), Vernant et al. (2010), Perouse et al. (2010) attribute the kinematic displacement of the region with slab-rollback towards the SSW, considering the Alboran Sea as a back-arc basin.

The previous work in this field has helped in understanding the complex geodynamic situation of the area of study by indicating that different tectonic models can be used to explain the unclear geodynamic evolution of the region (figure 7).

A

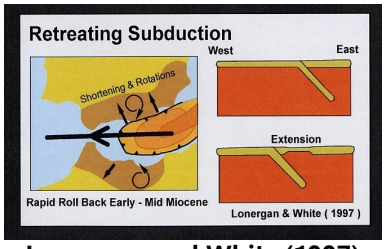

Lonergan and White (1997)

- West directed rollback of an east dipping subducting slab beneath the Gibraltar.
- constrained by paleomagnetic and seismic data.

B

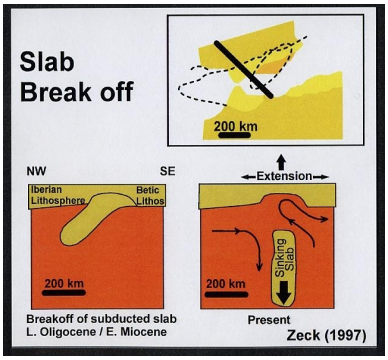

Zeck (1997)

- Detachment of near vertical subducted oceanic lithosphere.
- Obtained using seismic tomography.

C

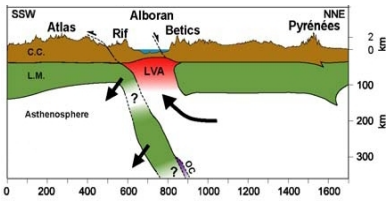

Fadil et al. (2006)

- N-S directed back arc opening in the Alboran Sea; deduced from the GPS-results.

D

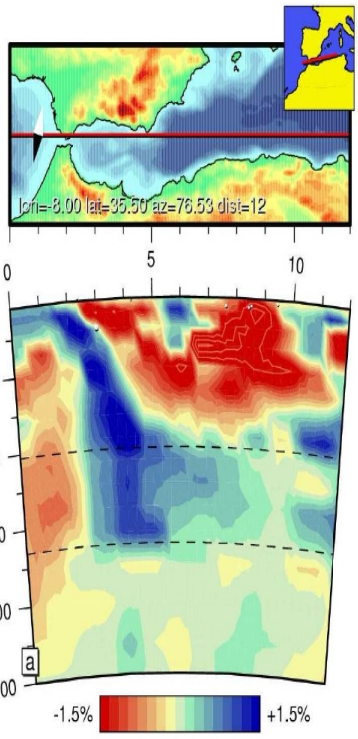

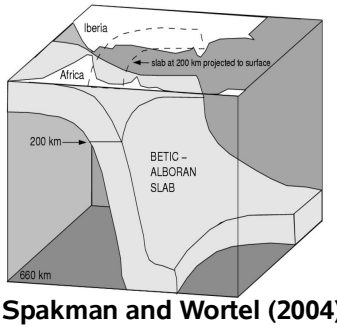

Spakman and Wortel (2004)

- Imaging of the high velocity body beneath the Alboran Sea using tomography technique (Eastward dipping model)

E

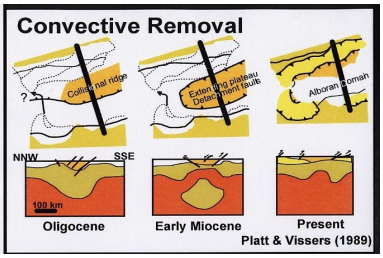

Platt and Vissers (1989)

- Detachment of the thickened lithosphere in continental collision zone and sinking into the asthenosphere possibly as a whole.
- Inferred from the P-T analysis of rocks.

F

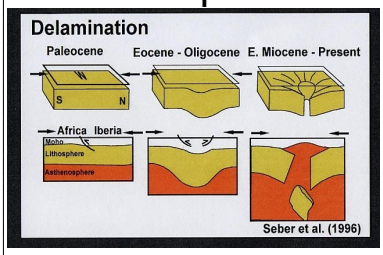

Seber et al. (1996)

- Seperation of previously thickened subcontinental lithosphere from the overlying crust; Peeling away and raising asthenospheric material replacing and the delaminiting lithosphere.
- Inferred from Seismicity and gravity measurements

G

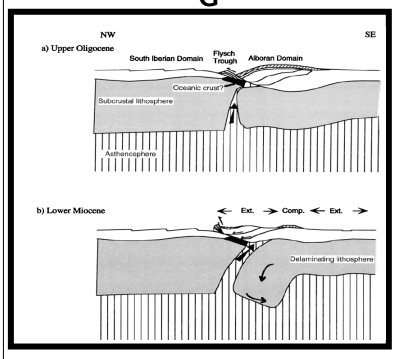

Docherty and Banda (1995)

- An active southeasterly migrating delamination model developed on the basis of the subsidence analysis.

Figure 7: Tectonic models proposed to explain the geodynamic evolution of the target region. The area under investigation has been extensively studied from a geological and geophysical point of view during the past four decades, and many different models have been proposed for its genesis and geodynamic evolution. Subduction (A, B, C, D), removal of the mantle lithosphere (E) and slab detachment or delamination of the lithospheric mantle (F, G) are considered viable mechanisms.

Chapter 3

Methodology

3.1 General introduction

This work deals with the application of the receiver function method to the data collected at the seismic stations deployed by several institutions in the Alboran Sea region and its surroundings area. The purpose is to obtain a better constrained picture of the crustal, sub-crustal and upper mantle structures, including features such as Moho, LAB, the mantle discontinues 410 km and 660 km. Seismic waves that are generated by distant earthquakes can be utilized to explore the dynamics of the Earth's interior by studying the distribution of different discontinuities lying beneath a seismological station with the aid of RF techniques.

The RF technique is a well-established processing and high-resolution imaging technique which uses the natural seismicity (e.g., distant earthquakes) as seismic sources and a portable or permanent seismological network as receivers in order to obtain detailed structural information from the Earth’s interior. It is based on the analysis of converted seismic waves created at an interface between two layers with different elastic properties. This methodology allows us to characterize the nature of seismic structures as well as to estimate the position of the interfaces beneath a seismological recording device. The main assumptions upon which RF computation is based, are that the Earth can be represented by a stack of homogeneous elastic layers, and that the seismic waves impinging from below the structure are sufficiently far from their source, so that they can be considered as plane waves.

Indicating the response of the Earth’s structure beneath a recording station, RFs are in the usual way time series generated from three-component seismograms by deconvolving one trace by another to extract signals created at interfaces (e.g., layer boundaries). For this purpose, the effects attributable to source complexity and heterogeneity of deeper structures along the propagation path are isolated from the waveforms.

In this work, we applied PRFs- and SRFs-analysis techniques in parallel to different data sets for our structural investigation of the westernmost Mediterranean region. These conceptually very similar techniques were used in a complementary way to image the key seismic velocity discontinuities which would contribute in the final analysis to a better understanding of deep Earth processes associated with lithospheric and mantle dynamics which are occurring within the interior of the target area. For this purpose, PRFs were utilized to characterize the crust and upper mantle structure, whereas the SRFs were used to resolve the uppermost mantle (lithospheric) structure.

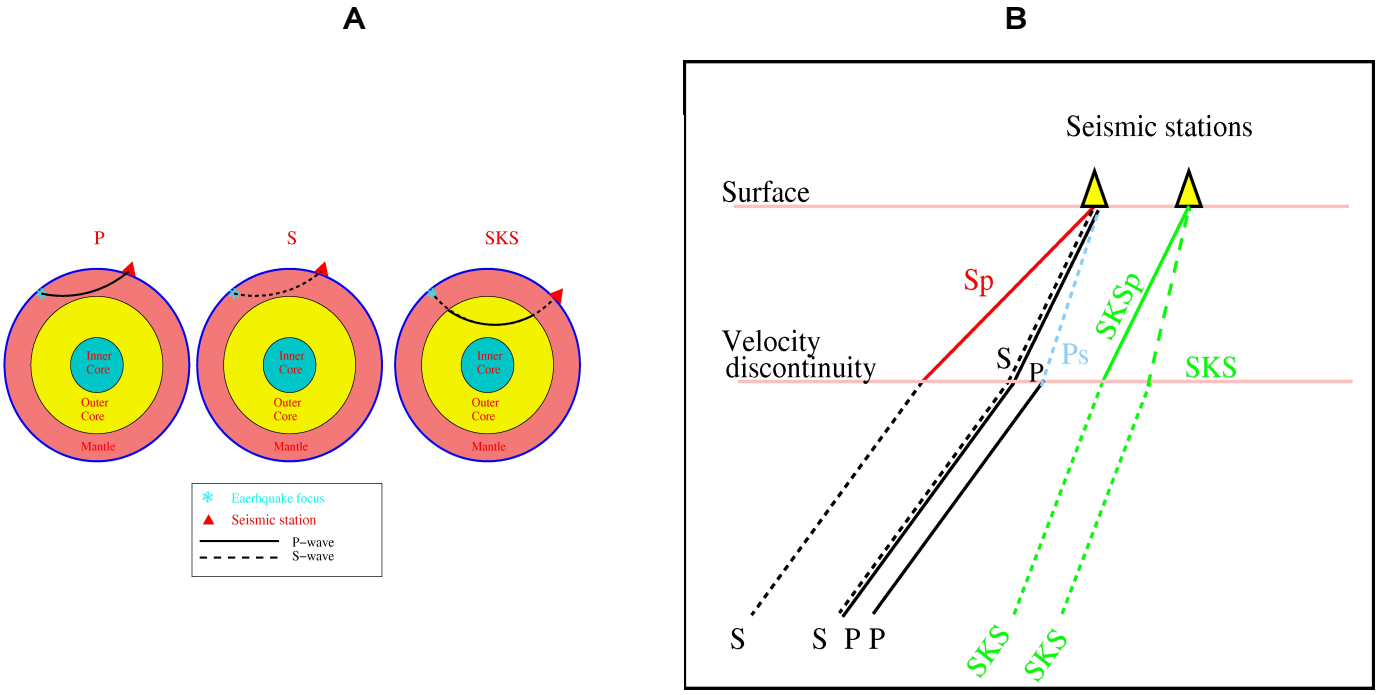

Figure 8: (A) Simplified diagram showing the theoretical ray travel paths for P-, S-, and SKS-waves, generated by a distant earthquake (teleseismic) source and finally received by a seismograph. Note that P- and S-waves sample the crust and upper mantle beneath the area investigated, whereas SKS-wave samples additionally the Earth's outer corn. **(B)** Geometry of the "Ps, Sp and SKSp" converted waves in a stratified elastic medium, as P-, S-, and SKS-waves from the teleseismic source pass through the material with different physical properties in the Earth "discontinuities/boundaries", where they change their directions and velocities. At such impedance boundaries, some of the energy of the incoming waves will be not only reflected but also some of them will be refracted (transmitted), whereby seismic mode-conversions such as P-to-S and S-to-P etc. take place as well. Based on measurement of the travel time delays of the transmitted, converted phases, receiver functions methodology is used for mapping deep seismic structure beneath a seismic station. Note the difference in horizontal distance from the stations sampled by P, S and SKS phases.

PRFs are generally created by using the mantle phases P, whereas SRFs are produced utilizing the mantle phases such as direct shear waves (S) and core-mantle refracted shear waves (SKS). Here at this point it is worth noting that SKS phases are originally S waves travelling through the Earth‘s liquid core as P-waves before converting back to S-waves. The typical ray paths of P, S and SKS waves, which are produced by a seismic source at the teleseismic distances are depicted in figure 8A. The principles of RFs analysis are based on the ray-theoretical treatment of seismic waves at welded boundaries. Any seismic waves (i.e., P, S or SKS) emanating from a teleseismic event source will be reflected, transmitted and converted when they encounter a seismic interface with impedance contrast. In this context, RF technique focuses on the analysis of the converted secondary waves, which emerge at an interface between two media of different elastic properties. By measuring the delay time between direct transmitted arrival (i.e., P, S and SKS) and the converted waves (i.e., Ps, Sp and SKSp), the depth of the velocity discontinuity beneath the seismic stations can be estimated, using an assumed velocity model. An illustration of the RF method can be found in figure 8B.

3.2 The P receiver function method (PRF)

Due to its sensitivity to the gross lateral variations in the Earth's structure below the receiver, PRFs analysis has proved to be a useful technique for detecting the depth variation of seismic velocity discontinuities. It was originally developed as a tool to model the crustal structure below recordings sites from the frequency-domain spectrum analysis of teleseismic P-waveforms recorded at a single three-component seismic station, using the amplitude spectra of long-period P waves (Phinney 1964). With the advent of digital broadband data, the time-domain receiver-function modeling was later introduced in the 1970s to constrain the crustal properties (Langston 1977, 1979). Nowadays, this technique is widely used to produce images of the crust as well as the mantle, using teleseismic waveforms. A comprehensive review of PRFs method are given by Bakun (1971), Leong (1975), Vinnik (1977), Owens et al. (1984, 1987), Sheehan et al. (1995), Ammon (1991, 1993), Dueker and Sheehan (1997), Al–Amri (1998), Shen et al. (1998), Li et al. (2000(a, b), 2003, 2004), Zhu (2000), Yuan et al. (1997, 2000) Grunewald et al. (2001), Niu et al. (2002), Ai et al. (2003), Shiomi et al. (2004) and Fee and Dueker (2004).

3.3 Theoretical background of PRFs analysis

A short review of the method is given here following the approaches from different authors as expressed above. Let us consider the wave front of a P-wave in the Earth which comes from the distance range between 30° and 95°. Within this teleseismic distance range, the P-wave-front arrives with a steep angle of incidence and is assumed to be nearly plane. The rays are nearly straight and parallel to one-another. The internal boundaries of the Earth are regarded plane layers as well. When the P-wave-front passes through such subsurface velocity discontinues (impedance boundaries), such as the Moho and the LAB, a number of seismic phases will arise as illustrated in figure 9A, representing the first-order reflections, transmissions as well as conversions from the above-mentioned velocity structures. The diverse types of seismic phases emerge independently, being subsequently recorded by a three-component seismogram (Z,N,E) on the Earth's surface. The remarkable difference between those phases consists in their travel paths, whereby crustal reverberations sample the structures away from the station, while the conversions take place in the direct vicinity. They can be generally categorized into the two main groups:

- P_pP_p, P_sP_p, P_pS_p, P_sS_p, P_p

- P_pP_s, P_sP_s, P_pS_s, P_sS_s. P_Ms, P_Ls

Dominating the vertical component (Z/L≈P) of ground motion, the first group of the observed waves includes the direct “Pp” and “P-reverberations (i.e., P_pP_p, P_sP_p, P_pS_p and P_sS_p)”, with the final ray legs spent in the “P-mode”. The second group of waves consists of the most important converted phases such as “P_Ms” and “P_Ls”, being generated at Moho and LAB velocity discontinuities, respectively. They are represented by the radial component (R/Q≈SV) of seismogram. Also visible on this component is a range of crustal reverberations (i.e., “P_pP_s, P_sP_s, P_pS_s, P_sS_s”,) with the final ray legs spent in the “S-mode”, where they are commonly produced between the surface and the Moho discontinuity. They can be easily distinguished from each other by their polarity and move-out response (changes in travel time with increased offset between earthquake source and receiver). In the case of a lateral homogeneous isotropic Earth, it is inherently assumed that the tangential component of ground motion (T≈SH) should not contain any energy. Therefore, it is often not taken into account in RFs analysis. As indicated above, in PRFs analysis, the rotated Q-component of ground

motion is commonly used, which theoretically contain the main conversions "P_{MS}, P_{LS}" and the associated crustal reverberations "P_pP_s, $P_pS_s + P_pS_s$" almost exclusively.

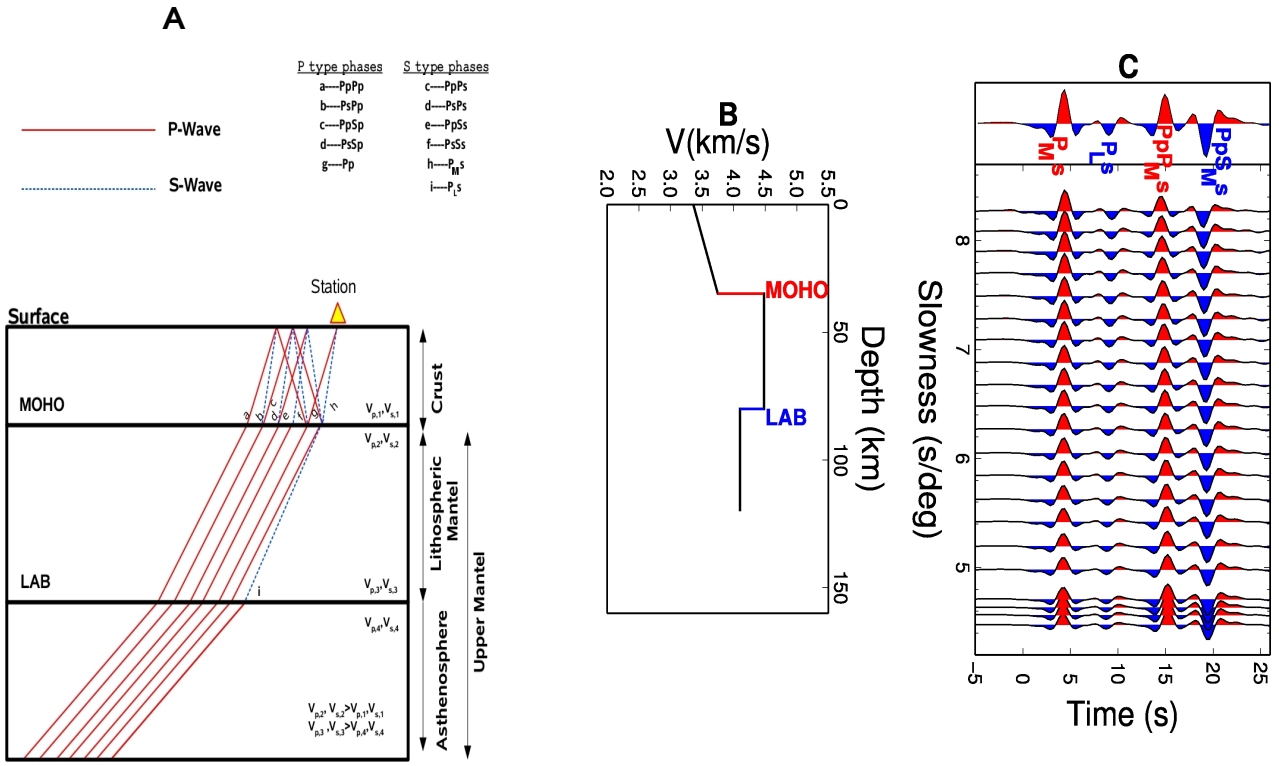

Figure 9) (A) General overview of seismic travel ray paths appearing at seismic velocity discontinues such as Moho and LAB in the case of the steeply incident P wave front in the distance range between 30°-95°. A planar P-wave is approaching through the discontinuities MOHO and LAB towards the receiver and gives rise to the generation of not only the direct "P_p" and reflected P waves "P_pP_p, P_sP_p, P_pS_p, P_sS_p" but also the P-to-S converted waves "P_MS" and "P_LS", as produced at the base of the crust and the lithosphere, respectively, and many other P-wave phases i.e., "P_pP_s, P_sP_s, P_pS_s, P_sS_s" due to the reverberations within the crust. P ray paths are indicated by red lines, whereas blue dashed lines mark the S ray. The notation used to describe ray paths for the two-layered model: The first capital letter "P" designates the incident wave. Lowercase letters refer to upward-travelling waves in the layer and uppercase letters denote downward phases. **(B)** Velocity model defined for the two main layers "Moho and LAB" and used in the computation of the synthetic Q-component PRFs. **(C)** Synthetic simulation of the Q-component PRFs calculated using the reference model. Synthetics are plotted for increasing ray parameters spanning from 4.2 to 8 s/deg. The major features seen on the synthetics are S arrivals related to P-to-S conversions and reflections in the crust (reverberations).

In order to clarify this, the synthetic Q-component for PRFs was simulated for a given Earth model with a crustal thickness of 35 km depth and a LAB at 80 km depth (figure 9B), following the data processing steps, such as “rotation”, “deconvolution” and move-out correction. The theoretical seismograms (figure 9C) were calculated by applying the reflectivity code written by Kind (1978). As can be easily seen, the phases “P_{MS} and P_{LS} are observed only a few seconds after the direct arrival of P, whereas the crustal multiples arrive later. It is worth mentioning that the two phases “P_sP_s and P_sS_s” are generally invisible because their energy is low and washed out by the direct arrivals. Furthermore, it is especially important to emphasize that the arrival “P_{LS}” from the base of LAB are mostly contaminated with interfering signals from the reverberations within the crust even though it is clearly identifiable in the synthetics. Being hampered by this fact, the image of the lithospheric mantle structure is mostly questionable when using the PRFs-technique. Even though, in some cases, this technique has been successfully used for resolving of the LAB (Rychert et al., 2005; Chen et al., 2006), in this work, PRFs were created only in order to identify the Moho and the 410 and 660 km mantle discontinuities.

In this study, PRF computation was basically performed through the 3-D rotation of the three component seismograms, and the deconvolution of the P-component from SV-component of ground motion in the time domain. The rotation process aids in the separation of upgoing P- and S-wavefields, whereby the deconvolution procedure allows suppressing the earthquake source and path effects. The deconvolution is accomplished through an iterative approach that relies on the cross correlation of the vertical and radial components. After the deconvolution routine, a band-pass filter from 1 to 10s is used.
To measure discontinuity depth, the time differences between the direct P-wave arrivals (Pp) and the converted phases (Ps) are generally used, as generated at the velocity discontinuities.

3.4 The S receiver function method (SRF)

An accurate knowledge of the depth extent of lithosphere is of particular scientific interest in understanding the geodynamic interaction of major tectonic elements in a long-term frame, in view of the prevalent concepts of plate tectonics. Within this context, one of the most difficult tasks in structural seismology consists therefore in imaging the LAB in greater detail, utilizing S-body waves. The base of the lithosphere is strongly believed to be underlain by a

low-velocity layer in the upper mantle, which is attributed with the asthenosphere. The high-velocity layer between the Moho and the base of the lithosphere is generally named the upper mantle lid. Large-scale structural analysis requires more accurate constraints on this lithospheric structure in order to describe the geodynamic evolution of tectonically complex regions. In this study, SRFs analysis have additionally been carried out to determine the spatial variations of LAB thickness across the westernmost Mediterranean region, and surroundings, in order to contribute to a better understanding of the tectonic evolution of the target area.

The SRFs technique is a state-of-the-art tool to image the structural variation of the LAB in a well-resolved scale. This technique was developed by Farra and Vinnik (2000). Its theoretical background was also described in detail by Yuan et al. (2006). Recently, this relatively new technique was adopted by many different working-groups to understand long-term physical process in the lithospheric depth range (see the review by Fischer et al. 2010 and references therein). Being a relatively new high-resolution imaging technique, this approach is basically complementary to the PRFs method, and therefore is used to provide independent constraints for the velocity discontinuities (e.g., crustal and lithospheric structure) lying beneath a seismological station. This technique has been successfully applied in a geologically complex area to better understand the variation of the LAB in depth (Li et al. 2004; Kumar et al. 2005; Vinnik et al. 2005b; Li et al. 2007).
The SRFs analysis has initially been used to study the S-to-P converted seismic phases (Sp) in order to determine the average layer thicknesses of the LAB. To enlarge our teleseismic data set, in this work, we also analyzed for the first time both the S-to-Sp (Sp) and SKS-to-SKSp (SKSp) phases using the SRF technique to image the lithospheric structure along the Alboran Sea and adjacent areas. In this context, it is important to note that the abbreviation “SRFs” is used throughout this dissertation as a generic term for the S-RFs and SKS-RFs. The lack of free-surface reverberations within the time window containing the Sp and SKSp arrivals allows the SRFs to provide rather more reliable information about lithospheric structure than the PRFs.

3.5 Theoretical background of SRFs analysis

Let us focus again on a laterally homogeneous isotropic Earth model, similarly to the PRFs. The ray paths of the seismic phases considered in the SRFs calculations are represented in

figure 10A. The converted secondary phases “Sp and SKSp”, emerging from the direct S and SKS waves, respectively, when they encounter a seismic interface with contrasting impedance, are mainly represented on the L-component. In contrast, the S related direct phases usually have their largest amplitude on the Q-component. In order to visualize this phenomenon, in the following, the L-component-theoretical SRFs (figure 10C) were generated, using the Frederiksen ray theory code on the basis of a given 1-D velocity model (figure 10B) that contains a Moho at 35 km and LAB at 80 km depth. The synthetic test was performed following the analysis schema used for the real-data.

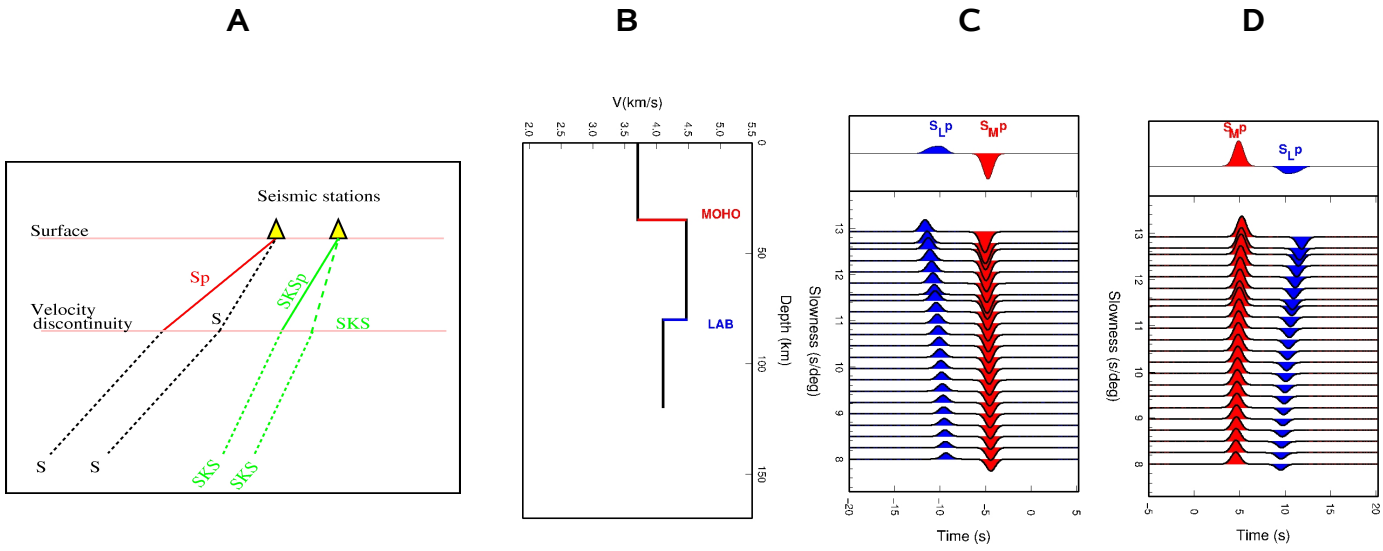

Figure 10: (A) Simplified diagram showing the ray paths of the “Sp” and “SKSp” converted waves generated at a velocity discontinuity below the station. Note that “S” and “SKS” phases sample velocity discontinuities at different locations and thus permit us to investigate different parts of the target volume away from the station. **(B)** Two-layered velocity model used for synthetic simulation of SRFs. **(C)** L-component synthetic SRFs showing the converted signals generated at discontinuities beneath the station. The major phases visible on the L-component are “S_Mp” and “S_Lp”. The converted, strong phase in red colour “S_MP” arriving approximately 5s before the direct S phase stems from the crust-mantle boundary (Moho). The converted dark blue phase “S_Lp” arrives 8s in front of the direct S phase and is interpreted as an S-to-P conversion from a discontinuity in the mantle where velocity decreases as a function of depth (Low-Velocity-Zone-LAB). **(D)** The time and amplitude of the synthetics SRFs are reversed to be able to make a direct comparison to PRFs. Synthetics are ordered by slowness which span from 8 to 13 s/deg. Variations in arrival times with increasing slowness are clearly seen for the Moho and LAB discontinuities.

Since the deconvolved SRFs present an opposite polarity with respect to the PRFs, the sign of the SRFs are generally inverted to facilitate direct comparison with PRFs. Additionally, SRFs are reversed in terms of time and amplitude (figure 10D). With this transformation on the SRFs, the downward positive (negative) velocity variation produces positive (negative) converted amplitude on the two types of the RFs. Note that the Moho "S_Mp" arrivals occur at about 5s after the direct S arrivals. Besides, significant negative conversion amplitude is clearly visible beyond the Moho, which is conventionally interpreted to stem from the base of the LAB, as marked as "S_Lp". This conversion is mostly hard to observe on the PRFs, as it falls into the time window, which is predominantly covered by the crustal multiples.

3.6 Evaluation and comparision of the methods used

Within the framework of this study, the seismic velocity discontinuities, such as the crust-mantle boundary (Moho), lithosphere-asthenosphere boundary (LAB) and 410 and 660 km transition zone beneath the Alboran Sea and adjacent areas have been investigated by a parallel application of PRF and SRF methods. The PRFs were computed with a technique similar to the SRFs, exchanging only the respective role of the P and SV components. The fundamental differences between these two kinds of RFs can be summarized as following:

1) The PRF method uses P-to-S (Ps) converted seismic phases which are triggered by the direct P-phase arrival due to a velocity contrast caused by a seismic interface. The SRFs method on the other hand deals with converted seismic phases, both S-to-P (Sp) and SKS-to-P (SKSp), originating from direct S- and SKS-phase arrivals, respectively.

2) The PRF analysis makes use of P-wave arrivals extracted from the teleseismic events originating at the epicentral distances ranging between 30°-95° with magnitudes larger than 5.7, while S- and SKS-waves arrivals from distant events with epicentral distances between $60° < \Delta < 85°$ and $85° < \Delta < 120°$, respectively, form the basis for the calculation of SRFs.

3) The converted Ps energy arrives at the seismometer in the P wavefield a few seconds later than the incoming direct P-wave. Unlike the Sp and SKSp, converted energy travels faster and arrives earlier than the incoming S- and SKS-wavefield, acting as a precursor.

4) Considering a spherically symmetric homogeneous radial Earth, direct and converted waves are de-coupled and appear on separate components in a properly rotated 3-component seismogram (Z,N,E are rotated into L(P), Q(SV), T(SH)). In PRFs analysis, the direct P-waves are predominantly visible on the L (longitudinal) component, while the corresponding converted waves (e.g., Ps, PpPs, PpSs+PsSs) show up on the Q-components. The energy on the transverse component (T) may indicate either the presence of dipping interfaces or seismic anisotropy. In contrast, in SRFs analysis, the direct S- and SKS-waves are mainly polarized on the Q-component, whereas the L-component is primarily dominated by the converted waves such as Sp, SKSp. Consequently, the Q- and L-components are used for P- and SRFs analysis, respectively.

5) Ps-, Sp- and SKSp- converted phases sample velocity discontinuities at different lateral locations due to different raypaths, thus, leading to investigation different parts of the target volume further away from the receiver in the area under investigation. In comparison to PRFs, the SRFs permit studying a broader area, even where no station is present. By subdividing the region of interest into small sub-regions, the deep structures can be investigated in more detailed using SRFs.

6) The PRF method gives generally reliable estimates of the depth of the Moho and mid upper mantle discontinuities at depths of 410 and 660 km. However, it is usually not suitable for imaging of LAB, since the converted phases stemming from the base of the lithosphere are mostly contaminated by free-surface reverberations within the crust.
In contrast, SRFs image (Sp and SKSp) are free of multiples because the converted Sp and SKSp waves arrive earlier than the direct S- and SKS-wave arrivals. Therefore, they do not carry the influence of the crustal reverberations arriving after S and SKS.

7) The resolution of seismic waves is a direct function of the wavelength; in principle, the shorter the wave length, the higher the resolution. SRFs have less ability to resolve fine-scale crustal structures, owing to its inherently longer dominant period. They are also noisy because of interference from adverse phases. In contrast, PRFs exhibit inherently shorter dominant periods than the S waves, and they are more sensitive for resolving crustal structures.

8) In comparison to PRFs, the SRFs contain not only some level of background noise but also noise which is generated from earlier arriving signals. Therefore, a probable influence of adverse phases on SRFs cannot be excluded.

3.7 Typical receiver functions analysis

In order to give a general overview of a typical RF-analysis-procedure, the principle flow of the RF analysis carried out within this work are firstly summarized in Table 1. The data-set was built by using events extracted from the NEIC earthquake catalog. The teleseismic waveforms were inheriently extracted from the recordings of events with magnitudes larger than 5.7 and epicentral distances ranging between 35°-95° and 60°-120° for PRFs and SRFs, respectively. In principle, there are several agencies that collect and/or distribute broad-band seismic data around the world (e.g., Geofon, IRIS, Erfeus). After selecting the useable events from the available event catalog, the teleseismic waveforms were requested from the data centers of those agencies. In this study, the seismic data were primarly provided by the IRIS- and Geofon data management centers.

The data processing step was similar in both the PRF and SRF-analyses, as indicated in the flow chart. After having obtained seismic data, a suite of processing steps such as rotation, deconvolution, moveout-correction and stacking were applied to the raw data in order to create the RFs. The RFs obtained were then used for further structural investigation of the area of interest. For example, they are utilized in the preparation of cross-sections in order to infer lateral variations along them.

After delay times of the converted phases (i.e., Ps, Sp, SKSp) had been transformed into the depth domain by using a velocity model, it was possible to create maps for the Moho, LAB, etc. Finally, the results were interpreted in terms of the geological features of the area investigated.

The PRFs were computed, using the procedures described by Yuan et al. (1997), whereas the SRFs were produced in a manner similar to that of Kumar et al. (2006). In the following section of this chapter, we will describe in detail the main steps in the RF analysis related to the preparation/selection and processing of the raw data, which have been carried out to calculate the two types of RFs.

RAW DATA (1) →	ROTATION (2) →	DECONVOLUTION (3)
► Selecting the suitable teleseismic events from the Earthquake catalogue provided by USGS ► Extraction of seismograms from database of GEOFON and IRIS data center	►Transformation of seismograms into the ray coordinate system of P,SV,SH components ► Using theoretical or observed value of azimuth and incidence angle of incoming seismic wave Target: Isolating the converted phases	►Using the spiking deconvolution technique in time domain Target: Removing the effects of source and ray path
MOVEOUT-CORRECTION (4) →	STACKING (5) →	DEPTH ESTIMATION AND INTERPRETATION (6)
► Using an epicentral distance of 67° as the reference distance ► Aligning and better identification of coherent phases in the individual traces	► Using two alternative approaches of traces stacking -station-based stacking -piercing points-based stacking Target: Enhance the signal-to-noise ratio	► Transformation of the delay time of the converted waves into the depth domain using a reference velocity model ► The resulting receiver functions are then used in preparation of cross sections and mapping the delay times of the converted phases across the studied regions. ► Testing the present tectonic models, or, eventually developing a tectonic model corresponding the achieved results

Table 1: Flow chart showing simplified basic steps for the RFs analysis. Once the seismograms have been extracted, a suite of processing steps such as rotation, deconvolution, moveout-correction and stacking were applied to the raw data in order to create the RF. This flow chart is similar in both PRF- and SRF-procedures. Finally, the results were interpreted, taking the geodynamical features of the area of interest into consideration.

3.7.1 Data organization

In this work, the data-sets were constructed by making use of the hypocenter catalogue of NEIC data center. In order to determine the suitable events, the catalogue was restricted to the major earthquakes (M>5.7) located at 30°-90°, 60°-85° and 85°-120° distances for P-, S- and SKS-phases, respectively. The selected records were then requested from the IRIS DMC and the GEOFON database for further analysis. Any seismograms containing gaps, or missing components, were neglected. Doing so, a PRFs data-set consisting of more than 5,700 teleseismic events as well as a SRFs data-set comprising more than15,000 teleseismic earthquakes were created.

3.7.2 Data selection

The raw seismic data were first visually controlled for each record to avoid noisy traces. To process the PRFs and SRFs, we selected corresponding events with high signal-to-noise ratios as well as events with clear and sharp P- and S(SKS)-onset in all three components, respectively. After this careful inspection, more than 5,500 P-waveforms and 14,000 S-waveforms proved to be sufficient for further processing.

3.7.3 Rotation

Teleseismic events are initially recorded by the seismometer according to the corresponding local coordinate system Z (vertical), N (North-South), and E (East-West). In order to separate different types of energy from each other, seismograms have to be aligned in the axis to the earthquake (backazimuth) and the angle of incidence. This can be achieved by accomplishing a 3-dimensional rotation procedure from the left-handed local coordinate system (Z,N,E) into the right-handed coordinate system (L,Q,T), which can be described as a ray coordinate system with mainly P-wave on the L-component, and SV and SH on the Q- and T-component, respectively.

Generally, two rotation steps are applied to the teleseismic events in order to generate receiver functions, being outlined in figure 11. Regardless of which type of RFs is calculated, the horizontal records (N, E) of the three component seismograms are firstly rotated into the

radial (R) and tangential (T) component using theoretical and/or calculated value of back azimuth (2-dimensions rotation). After that, the obtained seismograms are transformed into the (L-Q-T) system by determininig the theoretical and/or calculated incident angle of the incoming P- and S-waves (3-dimensions rotation). This type of rotation was used first by Yuan et al. (1997), which has a clear advantage over the alternative method of rotation into the (Z-R-T) components. This modified version of the rotation technique permits better separation of the P-to-SV and SV-to-P conversions from the P- and S-wave train respectively, and enable thus to identify converted phases even from shallow discontinuities.

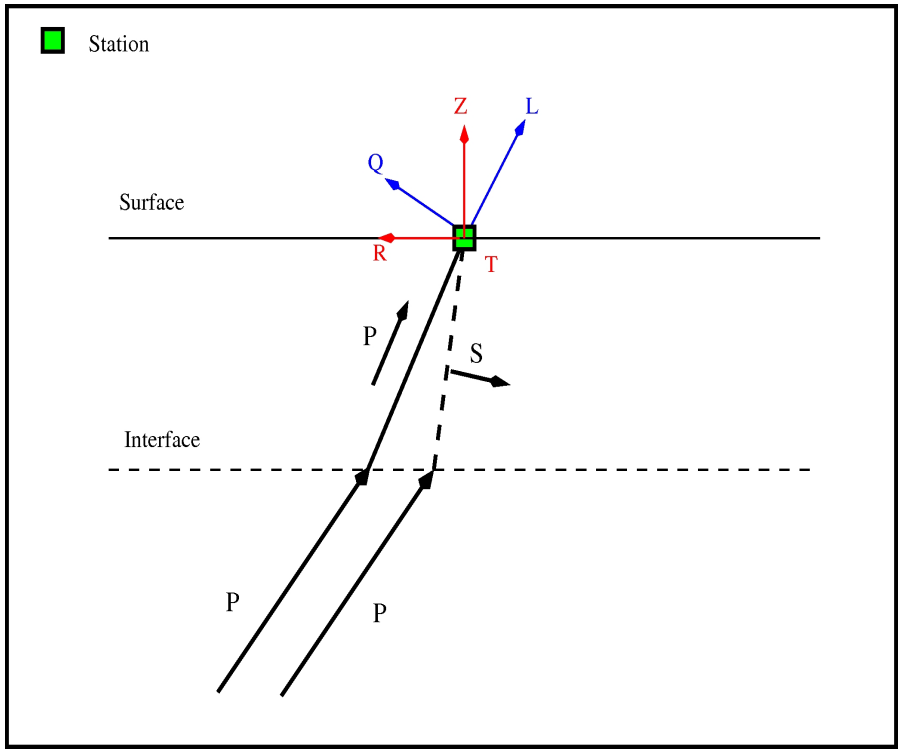

Figure 11: Sketch showing 2(ZRT)- and 3(LQT)-dimensional coordinate systems used in rotation process. Rotating the three-component seismogram with regard to the actual ray direction is crucial in obtaining the high portion of the energy of the signal.

In this thesis, the PRFs were generated using both the theoretical and calculated values of the rotation angles in order to be able to estimate the most suitable incidence and back-azimuth values. The theoretical rotation angles were firstly determined from the earthquake hypocenter location and the station location. But, in the presence of significant lateral velocity variations and low signal-to-noise ratios, this approach is mostly disadvantageous

because it results in a poor estimate of the true rotation angle, whereby the theoretical incidence correspondingly deviates largely from its real direction. In order to avoid this complication as well as to check the consistency of the theoretically-derived direction of incoming waves, the real rotation angles were also secondarily calculated using the eigenvalues of the covariance matrix of the observed three components P wave recordings (Yuan et al. 1997). The final angles were finally optimized comparing the observed and theoretical angles. In the case that the deviations for the incidence angles exceeds 20°, the events were eliminated from the data.

On the other hand, the rotation process applied to S-waveforms in order to generate SRFs differs substantially from that to P-waveforms. To create SRFs, the horizontal records (N, E) of the three component seismograms (Z, N, E) were in the first step rotated into the radial (R) and tangential (T) component using theoretical values of back azimuth of the incoming S-wave. In a second step, the three component seismograms observed (Z, R, T) were projected into the principle directions (longitudinal and in-plane transverse; L, Q, T) applying the calculated incidence angle, which was obtained by the iterative rotation technique. Three component seismograms were rotated through a series of incidence angles to generate a set of L component data. The optimal incidence angle was chosen by minimizing the direct S- and SKS-wave energy at zero time in the P-component.

3.7.4 Deconvolution

The seismic recording at a single three component station is generally considered to be a convolution of the source time history, source orientation, near-source structure, propagation effects through the mantle, and local structure beneath the recording site. The receiver function determination can therefore be inherently viewed as a deconvolution problem. In this dissertation, a time-domain least-squares deconvolution approach was applied in order to eliminate the complications connected with the instrument response and the source and ray path effects from the recorded seismogram. Thus, this permitted the isolation of the response of the local structures beneath the receiving station. For three-component data the removal of those effects can be accomplished by deconvolution. The deconvolution process, as applied in the PRF and SRF-techniques, differs only in exchanging the respective role of the P and SV-components. In the PRF-analysis, the L-component of the ground motion is assumed to be represented predominantly by the incoming P-wavefield, containing the

effects of the source and ray-path, whilst the SV-component is thought to be dominated by most of the P-to-S converted energy. Within this context, the SV-component (Q) is deconvolved with the vertical-component P (L) to obtain source-equalized PRF. In contrast, the SV-component is used in SRFs analysis as a proxy for the effective source time function and ray path effects to isolate the local response from the P-component.

The computations of PRFs and SRFs are done in time domain using the Toeplitz matrix made from the autocorrelation of the specified window (Oldenburg 1981; Gurrola et al. 1995; Zhu 2004). In PRFs analysis, a time domain spike deconvolution operation is performed for the waveforms in the time between 5s, before, and 80s after, the predicted P-wave arrival time. On the other hand, in SRFs calculation, a deconvolution routine is accomplished for a time window of 100 s, starting from the 10s before the S and SKS- arrivals. The deconvolution is carried out by generating an inverse filter in the time domain and compressing the energy into a approximate spike at a zero lag time, where a trade-off parameter is applied to stabilize the inversion.

The deconvolution (inverse) filter is created by minimizing the least-squares difference between the actual output and the desired delta-like spike function of normalized amplitude. After the deconvolution process, the PRFs data are then filtered with a Butterworth bandpass filter from 1 second to 0.1 Hz, while the SRFs data are band-pass filtered in the frequencies ranging between 0.3 and 1 Hz.

Another approach used to compute source-equalized receiver functions may be the frequency-domain deconvolution technique, also referred to as the water-level deconvolution technique. In general, these two approaches provide similar results when the available data are broadband, with high signal-to-noise ratio.

3.7.5 Moveout-correction

The difference time of two phases travelling with different slowness (ray parameter) depends on the epicentral distance. Therefore, this moveout must be corrected before summation. The moveout-correction procedure is performed for RFs to align and for better identification the coherent phases. Doing so, one can also stack the RFs computed for events approaching from a range of distances to improve the signal to noise ratio.

RFs are moveout corrected for a certain ray parameter. For this purpose, we applied the same approach as Yuan et al. (1997), in which 6,4 s/deg is used as a reference ray parameter, corresponding to 67 degrees epicentral distances. The IASP91 model is used to compute the moveout-correction. In this way, earthquakes at different distances, with correspondingly different ray parameters, can be stacked. It is worthy to mention that this correction is particularly essential for aligning and stacking the converted phases from the upper mantle discontinuities at 410 km and 660 km by helping distinguish them from the uppermost mantle multiples.

Deconvolution and distance moveout correction steps are applied in order to enable the summation of events from different distances and with different magnitudes and source-time functions. Likewise, a reference P-wave slowness of 6.4 s/deg is also utilized for SRFs in order to make the SRFs directly comparable to the PRFs. The moveout-correction can also be done for multiples, besides the directly converted phases.

3.7.6 Stacking

Seismic data often contain substantial noise, particularly when the source is relatively weak and/or the structure is highly complex. By suppressing noise and increasing signal-to-noise ratios, the stacking procedure is traditionally used (Gilbert et al. 2003) in teleseismic RFs to improve the stability and reliability of the observations. This routine enables us to resolve even small-amplitude features by cancelling the random noise and other unwanted phases within the individual receiver functions. Stacked receiver functions, thus, can be generally viewed as averaged waveforms which accentuate laterally coherent features.

In this work, two different approaches were used to stack RFs. For crustal structure analysis, traces from the same station were typically stacked together to improve the signal-to-noise ratios. This is also known as a single station/multiple event stacking technique. However, this approach is not always efficient when determining a deeper discontinuity structure (e.g., LAB, 410 and 660). In this case, the individual traces were stacked using the common conversion point (CCP) stacking technique. The concept that this technique envisages, among other things, involves stacking RFs recorded by multiple stations which sample the same subsurface area. For this purpose, the exact position of the conversion point was determined by geographically binning the ray set, using the IASP91 reference model. The

resulting RFs were then used in preparing cross sections and mapping the delay times of the converted phases across the studied regions.

3.7.7 Data analysis and interpration

A set of processing steps such as rotation, deconvolution, moveout-correction and stacking were applied to the raw data in order to calculate the PRFs and SRFs. To be able to estimate the lateral deep variations of the prominent velocity discontinuities along the area of study, the resulting receiver functions were carefully examined. The examination was conducted, in terms of the converted phases from the possible subsurface structures, by means of both the stationwise- and piercingpoints-stacking approaches. Lastly, the results obtained were interpreted against the backdrop of the geodynamical features of the target area.

3.7.8 Real data examples and main processing steps

The converted phases generated at the seismic discontinuities under a station are generally signals of low amplitude. Because of the high level of noise in records, these mode-changed phases are usually difficult to discern/detect visually on a seismogram. To isolate and enhance these converted signals, which are hidden in the P- and S-waveforms, a procedure with a sequence of data processing steps is basically implemented as described in the previous sections of this chapter. In order to highlight this fact, an example of PRF and SRF, created from teleseismic data recorded by the broadband station EVO and MTE, respectively, (figure 12), has been shown.

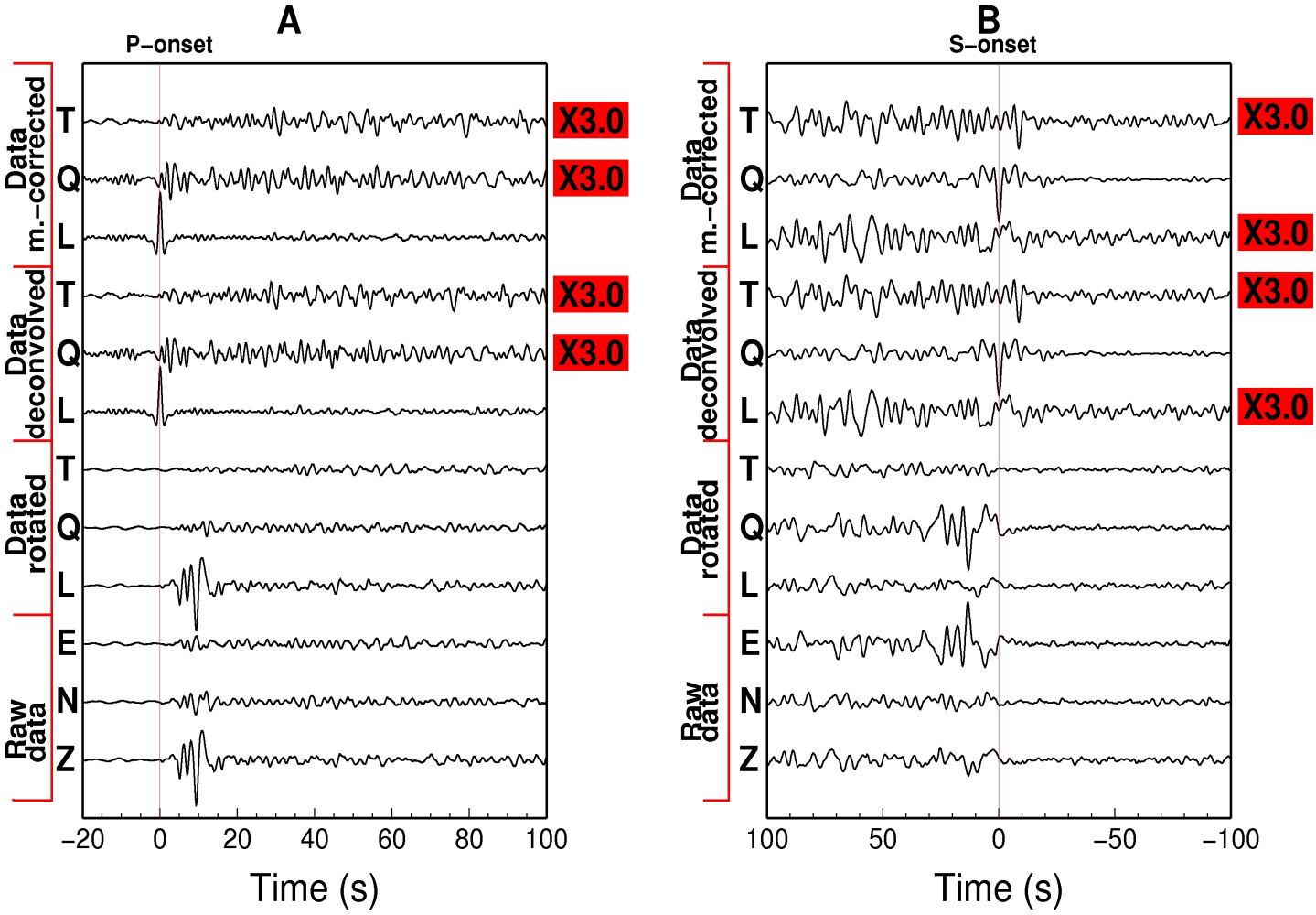

Figure 12: **(A)** An example of PRF data generated for the teleseismic data recorded at the EVO station with the epicentral distance of 82° from an event of Mb = 6.3. The event occurred on November 13, 2006, 01:26 origin time. Traces are band-pass-filtered at 0.1-1 Hz. Amplitudes of the components were scaled (normed) after each processing step. Due to its SV wave polarity, the converted Ps phase should primarily be registered on the Q-component. To better recognize the converted phases, the Q- und T-componenten obtained after the deconvolution procedure were multiplied with a factor of 3. **(B)** An example of SRF calculated for the teleseismic data recorded at IFR station with the epicentral distance of 80° from an event of magnitude Mb = 6.4. The event occurred on February 12, 2008, 12:50 origin time. Amplitudes of the components were similarly scaled (normed) after each processing step. Differently from PRFs, the polarity of the SRFs amplitudes was reversed. Negative time scale indicates times in front of S-arrival. Traces were band-pass-filtered at 0,03-1 Hz. Because of its P wave polarity, the converted precursor Sp should principally be dominated on the L-component. To better recognize the converted phases, the Q- und T-componenten obtained after the deconvolution procedure were in turn multiplied with a factor of 3.

Chapter 4

Crustal thickness variations estimated from PRFs analysis

4.1 General information

Being a compositional discontinuity, the crust-mantle boundary, also known as Mohorovičič discontinuity or Moho, marks the transition from the crust to the uppermost section of the mantle. This relatively narrow zone of the Earth can be characterized by an increase in seismic wave velocity as the waves pass from the crust (6.5 km/s) to the underlying mantle (8.1 km/s). The increase in seismic wave velocity occurs as body waves travel from lower density felsic rocks of the continental crust (i.e., granite) and mafic rocks of the oceanic (i.e., basalt) crust into higher density ultramafic rocks of the mantle (e.g., peridotites).

Numerous seismological observations have been put forward during the last decades to show that the Moho depth varies significantly. It is the thinnest beneath the oceans, averaging only 5-10 km thick, and the thickest place being beneath large mountain ranges, such as the Himalayas or the Sierra Nevada, where the crust reaches a thickness of up to 90 km. The continental crust averages in thickness from about 30-35 km (Monroe et al., 2008).

4.2 PRFs data

In this study, a large number of seismic data was analyzed, belonging to thirty-seven temporary and permanent stations of the nine different networks deployed within the framework of diverse geophysical experiments in the area of study. To create the PRFs-data-set, we firstly selected all the earthquakes with M≥5.7 within epicentral distances from 30°-95°, using the global earthquake catalogue of the U.S. Geological Survey–NEIC (National Earthquake Information Center (http://earthquake.usgs.gov). we subsequently extracted the usable teleseismic recordings from these data centers:

- Incorporated Research Institutions for Seismology
  IRIS: http://www.iris.washington.edu

- and GeoForschungsNetz, Geo Research Network
  (GEOFON: http://geofon.gfz-potsdam.de/geofon/)

The core data of the PRFs-study came mainly from seismic stations of the TEDESE-temporal network deployed from 2001 to 2004, which covered the southernmost region of Spain and northernmost Africa. Additionally, data from the temporary stations of the IAG Regional Network extended the data coverage substantially. Overall, we used teleseismic records from the following networks operating in the target area:

- The TEDESE seismic Network.

- IAG Regional Network / Andalusian Institute of Geophysics.

- The GEOFON / Western Mediterranean Seismic Network.

- The Mediterrean Network (MEDNET) / Istituto Nazionale di Geofisica,Italy.

- Global Seismograph Network (IU)/ USGS Albuquerque Seismological Laboratory.

- YF Network - Mantle Investigation of the Deep Suture between Eurasia and Africa (MIDSEA) / collaborated experiment by four institutes.

- GEOSCOPE (G) / Institut de Physique du Globe de Paris.

- Portuguese National Seismic Network (PM) / Instituto de Meteorologia.

- University of LISbon SEISmic network/Centro de Geofisica da Universidade.

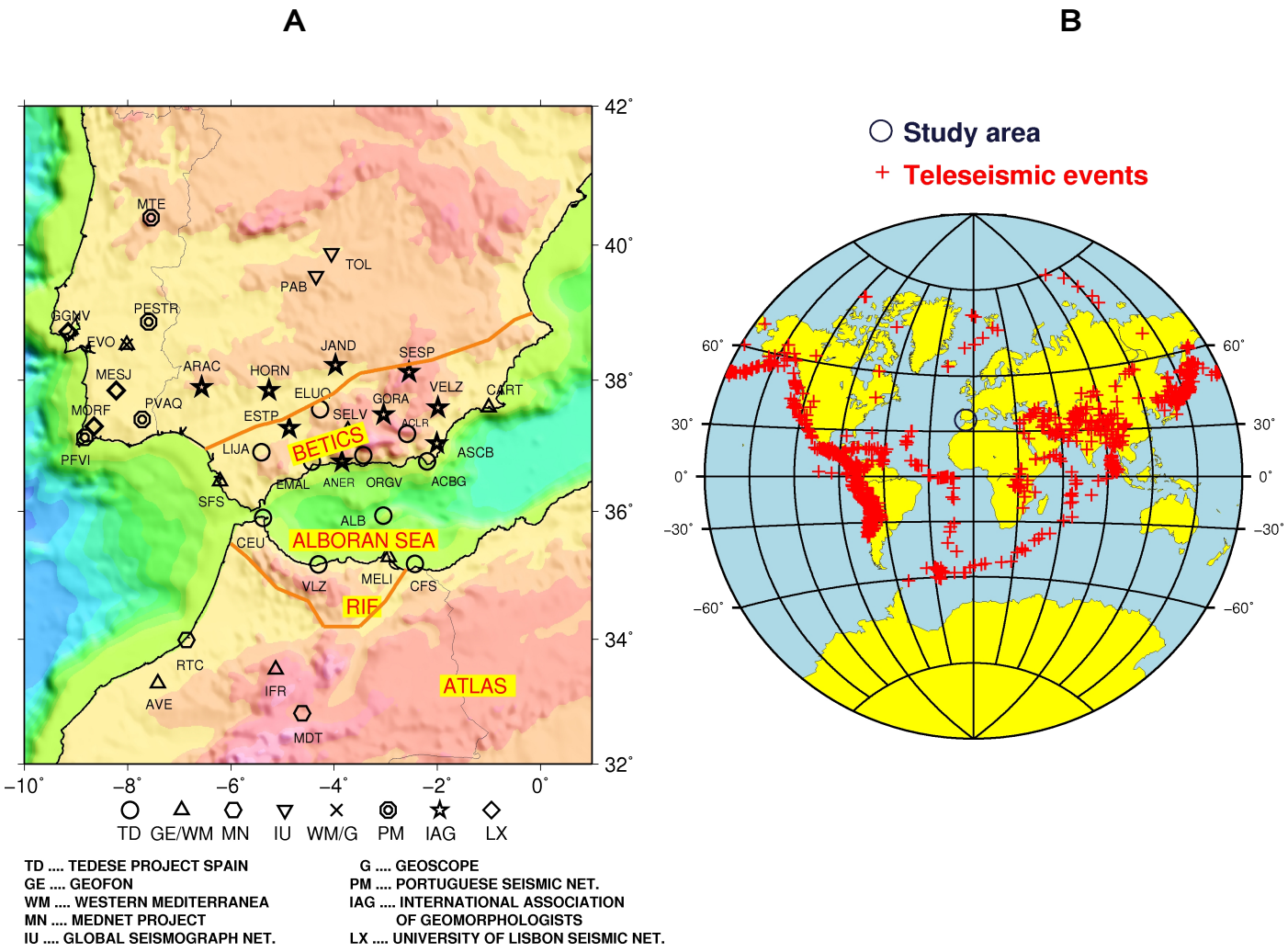

Figure 13: (A) Map of the study region with seismograph stations. Seismic data was obtained from the data center of the Incorporated Institutes for Seismology (IRIS) as well as from GFZ Potsdam. Stations used are coded by different symbols in respect to the conducted experiments. **(B)** Spatial distribution of PRFs-events with large magnitude (M > 5.7) from the epicentral distances between 30°-95°. Earthquakes are indicated by crosses. The circle indicates the area of study. The best azimuthal coverage is obtained from westerly and easterly directions.

Thus, the data of thirty-seven broadband stations operated by different institutes along the region of interest was able to be combined. A list of the stations used and their characteristics (e.g., codes, coordinates, and elevations etc.) is provided in Appendix 1. It is important to note that some stations have been in operation for a longer period than others, and, consequently, have a larger data set. For instance, belonging to the Global Seismograph Network-GSN (IRIS), the seismic broad-band station PAB has been operating since 1992, and is the longest running station in the area of study and is located in the

central part of the Iberian Peninsula. The total number of the teleseismic events with a high signal-to-noise ratio recorded by the station PAB is 591, which were regarded as suitable for PRFs analysis within this work. In contrast, the shortest time-period operating station is the station MORF from the Portuguese National Seismic Network (PM). Situated in the south-western part of the peninsula, this has been in operation for ca. one year. That station provided this study with 71 usable teleseismic events. The geographical distribution of those stations and the epicentral distribution of the teleseismic events used within the scope of this work were illustrated in figure 13A and 13B, respectively. As can be easily seen on the teleseismic events map, most events came from NE and SW-NW backazimuths, due to the larger seismicity of the Kuril and Aleutian Islands, India and Asia-Himalaya range, Andes and Central America regions. Additionally, we would like to give an overview of the events-back-azimuth distribution for each station. For this purpose, in figure 14, circular histograms (red diagrams) were plotted showing the teleseismic events in terms of the incoming back-azimuths.

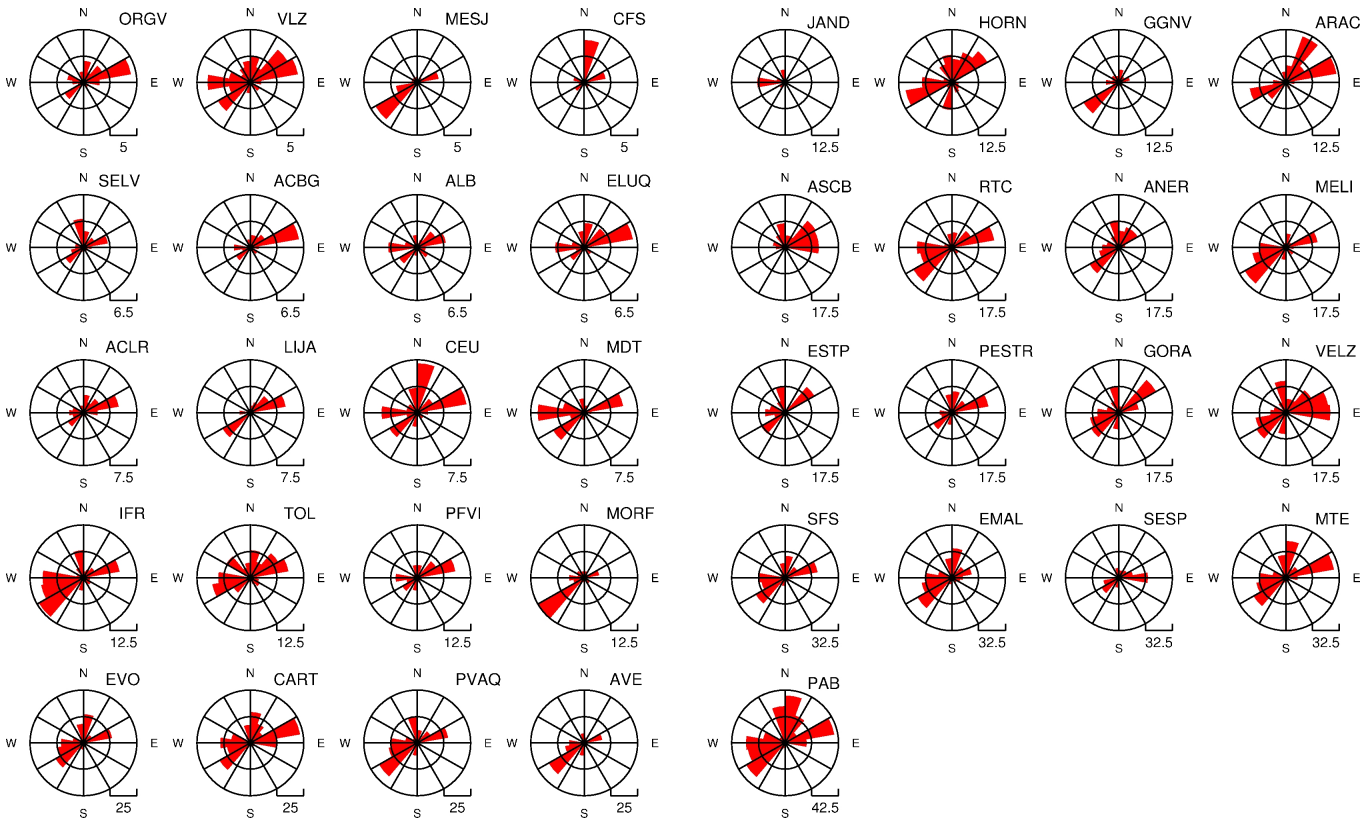

Figure 14: The diagrams show the back-azimuthal distribution of the teleseismic events in red for each station. Each ring represents the number of events which is shown on the bottom right-hand side of each diagram. The orientation is binned in 30 degree increments.

To give an overall view of the PRFs data used in this study, some important event parameters such as depth, magnitude, back-azimuth and epicentral distance are also presented in figure 15. The great majority of teleseismic events used are located shallower than 10 km, even if a small number of all events occurrs at depths of 300–700 km. The observations generally cover a magnitude range from 5.7 to 8.9 M, but a relatively small number of events greater than M=7 exist. The best coverage was obtained in the back-azimuthal ranges 10° to 75° and 210° to 300°. In PRFs, the teleseismic events with epicentral distances between 30° and 95° are usually utilized. In the data-set, the great majority of events has epicentral distances between 70°–95°.

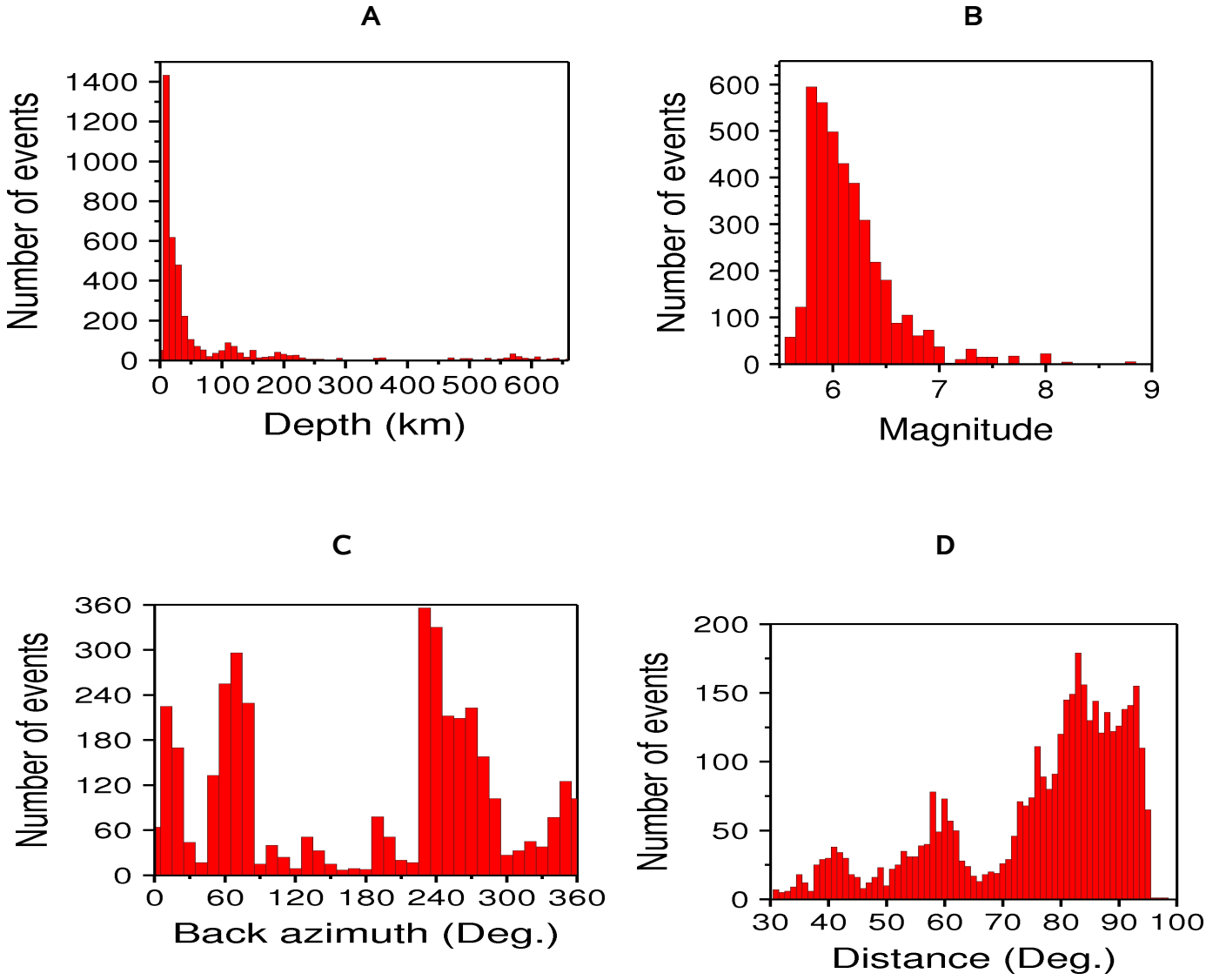

Figure 15: Histogram showing some parameters of the teleseismic events used in the PRFs analysis. Presented are the distribution of focal depths **(A)**, magnitudes **(B)**, back azimuths **(C)** and epicentral distances **(D)**.

Figure 16 summarizes the PRFs data coverage for each station. The blue crosses within the circles are the piercing-points which indicate theoretical P-to-S conversion-points, calculated for each station at a 35 km depth, based on a one-dimensional (1-D) IASP91 velocity model (Kennett and Engdahl 1991). The converted waves (Ps) sample the layers at 35 km depth directly beneath the receiving stations in a small region with a diameter of about 30 km.

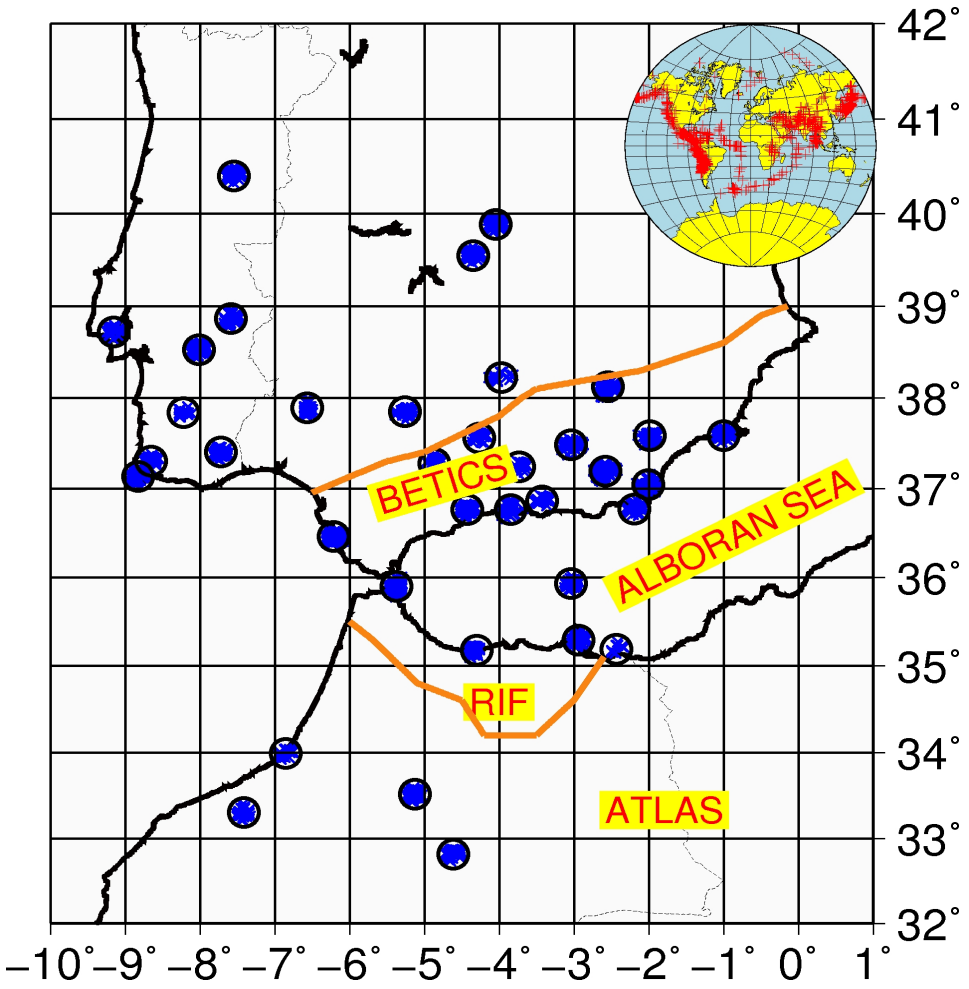

Figure 16: The distribution of P-to-S piercing-points for the thirty-seven seismological stations at a common conversion depth of 35 km. Those are denoted by the blue crosses within the circles. Clearly visible is that the P-to-S conversion points sample the layers directly beneath the receiving stations. The map inset shows the distribution of teleseismic events used for PRFs calculation.

4.3 Data examples

To give an impression of the data quality, we want to present some representative data examples. For this purpose, the PRFs for the stations PAB (A), MTE (B), EVO (C) and

PESTR (D) are displayed in figure 17, which were calculated by using a different set of teleseismic events recorded at those sites. The lower panel in each diagram shows the individual traces sorted according to the back-azimuth. The resulting stacked PRFs are also represented on the upper panel in each diagram. To supress noise and better observe coherent signals, each RF is band-pass filtered in the frequency range of 0.1 to 1 Hz before correcting for the move-out for the direct arrival (Ps). This is done by using a reference slowness of 6.4 s/deg. To enhance the features, which are prominently seen throughout all individual traces, individual traces were then stacked (summed). The azimuthal coverage is sufficient at each station to reliably determine the lateral variation of the crustal structure. However, this is not the focus of this research. The Moho phases and the main multiple reflected phases within the crust are indicated on each of the PRFs stacks by Ps (a), PpPs (b) and PpSs (c) which can be identified on each PRFs-stacks at approximately (3.4s - 3.8s), (12s – 14s) and (16s – 18s) delay time, respectively. All stacks display several high-amplitude conversions within the first 4 s, pointing out some discontinuities within the Earth's crust. In principle, each of the positive phases seen on each summation trace within approximately one second can be attributed to the converted SV-wave from an intra-crustal interface, which is commonly interpreted to be produced at the base of the sediments (sediment-basement discontinuity). Differently from EVO and PESTR, an additional positive phase at about 2s delay time is also clearly visible on the summation traces of PAB and MTE, which can be interpreted to be a reverberating SV-wave within this layer. PRFs at stations MTE and PAB suggest generally a rather complex crustal structure beneath those stations with an approximate Moho depth of 27 km and 30 km, respectively. Being located in central Spain, PAB presents a relatively clear Moho conversion at 3.8s. In contrast, the stack for station MTE reveals a markedly different character, showing a strong positive peak at 2.1s and a smaller amplitude conversion at 3.4s. Even though the third positive peak at 3.4s is marked by lower amplitude, it seems to us to be most likely the seismic Moho. Within this context, the second positive phase was interpreted to be a free-surface reverberation from the basement-sediment contact. By comparing the PRFs- and SRFs- waveforms belonging to MTE, the conclusions were sufficiently confirmed. On the other hand, the PRFs stacks from EVO and PESTR reveal that the crust beneath those sites seems to be more or less homogeneous with roughly the same thickness. At stations EVO and PESTR, a strong Moho arrival Ps (a) at 3.6s to 3.7s is observed, which corresponds to Moho depths of 29 to 30 km, respectively. In addition, the multiply reflected phases PpPs (b) and PpSs (c) can be clearly detected for two stations, as can be seen in figure 17.

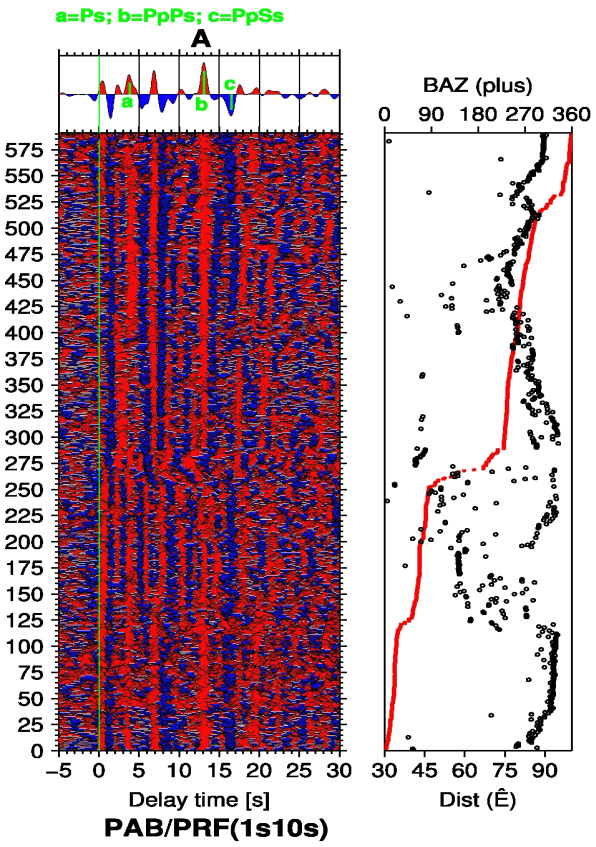
a=Ps; b=PpPs; c=PpSs
A
BAZ (plus)
0 90 180 270 360
Delay time [s]
Dist (Ê)
PAB/PRF(1s10s)

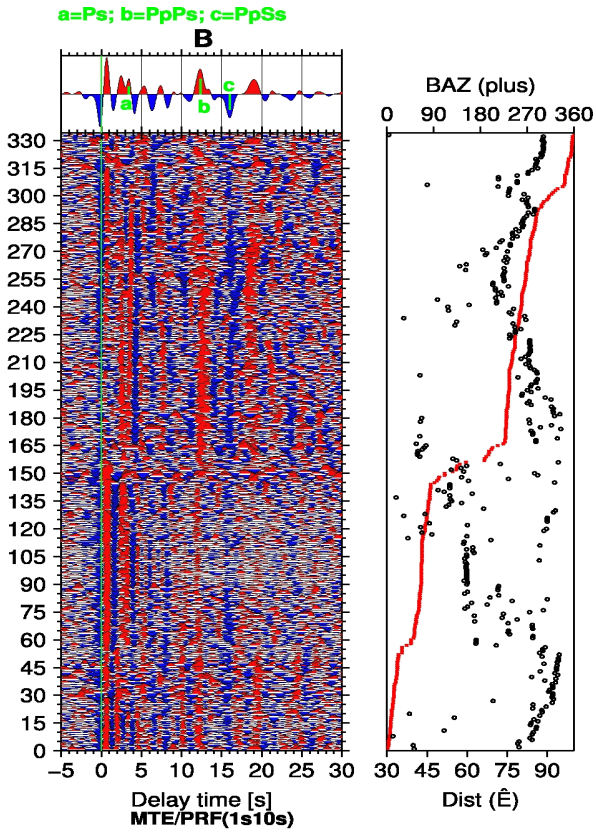
a=Ps; b=PpPs; c=PpSs
B
BAZ (plus)
0 90 180 270 360
Delay time [s]
Dist (Ê)
MTE/PRF(1s10s)

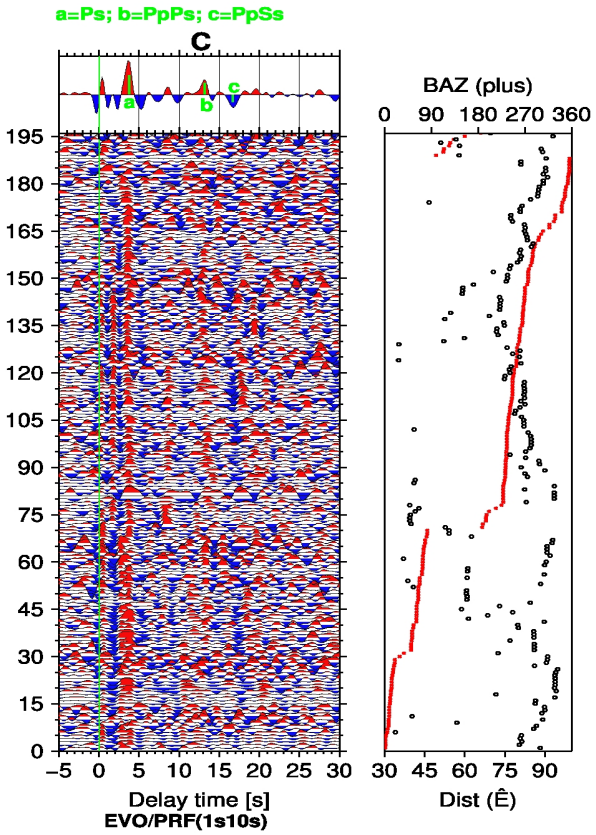
a=Ps; b=PpPs; c=PpSs
C
BAZ (plus)
0 90 180 270 360
Delay time [s]
Dist (Ê)
EVO/PRF(1s10s)

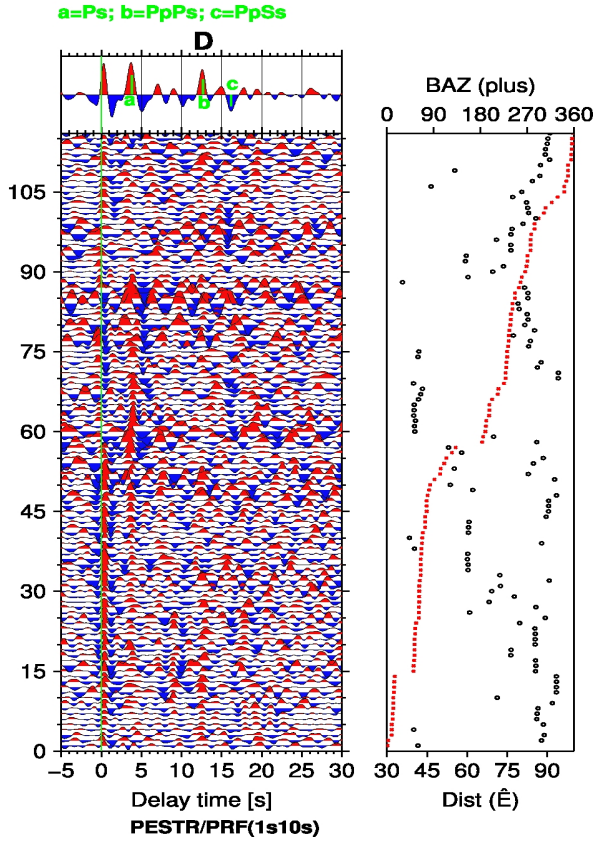
a=Ps; b=PpPs; c=PpSs
D
BAZ (plus)
0 90 180 270 360
Delay time [s]
Dist (Ê)
PESTR/PRF(1s10s)

Figure 17: Slowness moveout-corrected PRFs at stations PAB **(A)**, MTE **(B)**, EVO **(C)**, and PESTR **(D)**. The individual traces sorted by the back-azimuth (red squares) were band-pass filtered with corner frequencies of 0.1 and 1 Hz to eliminate high-frequency noise before the move-out correction. The upper trace in each panel shows the stack of all receiver functions for the corresponding station. The summation traces for each station show very slight difference, particularly in the timing of primary conversions phases and multiples. Ps phase from the Moho and its multiples PpPs and PpSs are clearly visible after the P arrival. It is also clearly seen that a significantly, coherent intra-crustal P-to-S converted phases arrive between the direct P- and the Moho-converted Ps phase, indicating a multi-layered seismic structure. Positive polarity energy is plotted in red; negative polarity energy is plotted in blue. The distance ranges and azimuths are indicated on the right of each diagram with black circles and red squares, respectively. The number of events used to compute receiver functions are also indicated on the left hand side in each section.

4.4 Summation traces of PRFs from all stations

In the next step, the corresponding stacked PRFs were compiled for each station, not only to present a general view of the timing of the important phases, such as P-to-S conversions, but also to obtain some information on the local structure from the observed waveforms. From the observed PRFs stacks shown in figure 18, the following conclusions can be essentially drawn:

1) In general, the stations in the Iberian Massif interior (PVAQ, MORF, TOL etc.) generate a better stack from a smaller number of PRFs.

2) Receiver functions produced for stations in the internal and external zone of the Alboran Sea region are very complex, corresponding to the complicated geology in this area (e.g., ALB, ACLR, ACBG, CFS, GORA).

3) The amplitude of the RFs is generally determined by the impedance contrast across an interface and the incidence angle of the incoming wave. Even if the converted waveform of the Moho discontinuity at most station stacks is very clear (e.g., TOL, ASCB, IFR, etc.), some station stacks are characterized by a lower-amplitude Moho conversion (e.g., CFS, SELV, EMAL, SESP, GORA).

The possible explanations for this observation would be as follows:

A) The velocity contrast might be considerably higher at the intra-crustal interface (e.g., sediment-basement discontinuity). This might give rise to strong intra-crustal multiples that mask the Moho phase.

B) The delay times of the signals associated with P-to-S conversions at Moho discontinuity might vary significantly due to a lateral change of the topography of the Moho interface (e.g., dipping structure) or to the azimuthal dependence on the seismic velocity of incoming waves. Correspondingly, stacking incoherent phases could result in smearing out or annihilating the corresponding signal generated from the Moho discontinuity. Under such circumstances, it is difficult to reliably estimate the converted signal from the Moho on the summation trace, because of its lower amplitude level. For this case, the corresponding P- and SRFs waveforms are directly compared in order to be able to infer the correct conversion signal from the Moho.

C) The amplitude of the RFs also depends on the ratio between the width of the interface (thickness of the transition zone) and the wavelenght of the incident wave. A sharp boundary between crust and mantle may also lead to the generetation of the low-amplitude Moho conversion.

4) In the case of a thick gradational Moho, the RFs generally show a strong-amplitude converted phase when generated at this seismic boundary (e.g., MDT, PVAQ, ESTP, EVO, PAB).

5) For some traces (e.g., for stations CFS, ASCB, ORGV, etc.), the crustal multiples are notably missing or not clearly visible on the receiver functions; they seem to be partially annihilated or suppressed by later arrivals from the upper mantle.

Finally, it should be noted that PRFs are calculated for each station using a different number of earthquake records. The number of traces used in each stack are indicated on the left side of figure 18, which varies from 20 (CFS) to 591 (PAB).

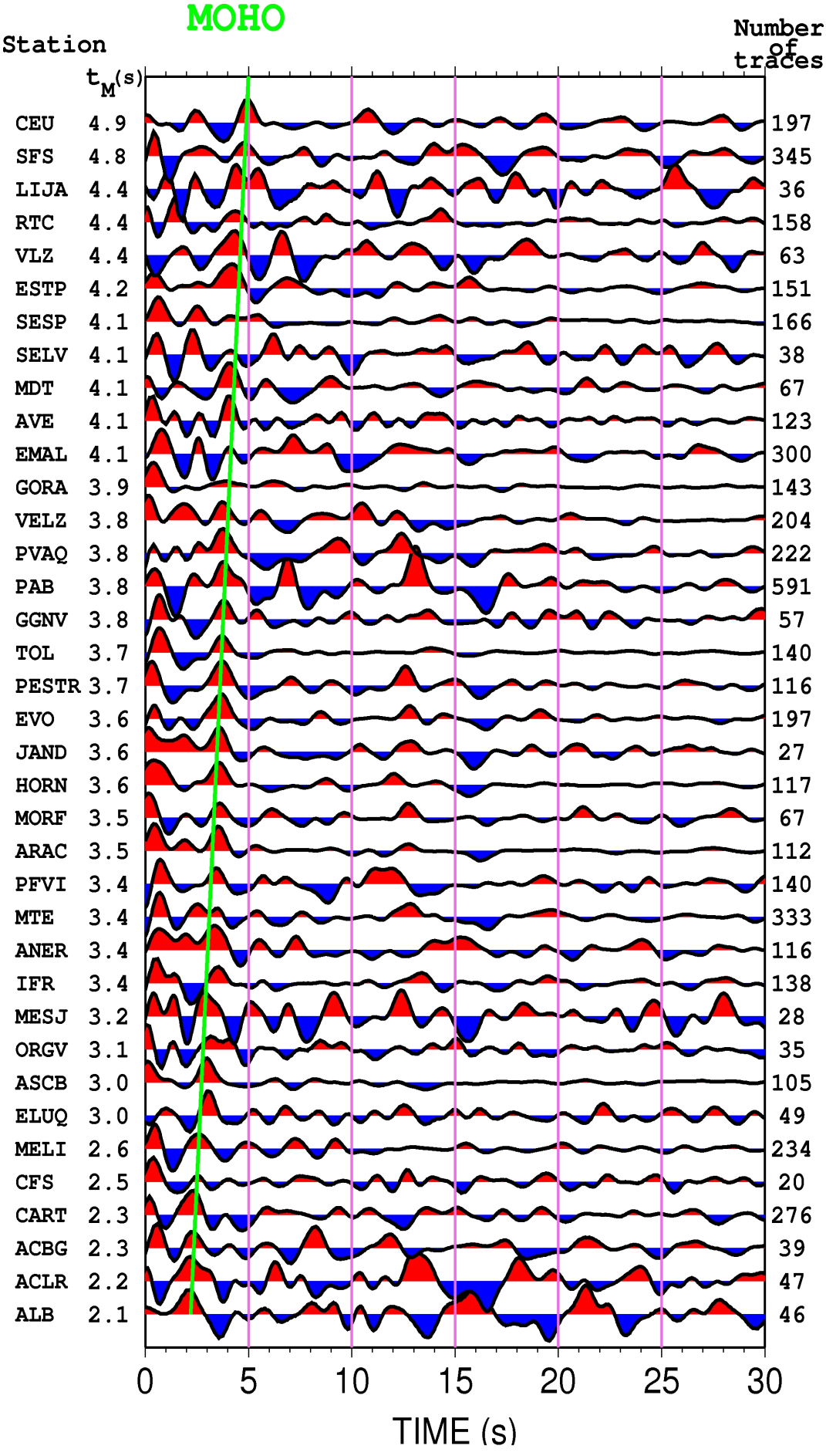
MOHO
Station
Number of traces
t_M(s)
CEU 4.9 197
SFS 4.8 345
LIJA 4.4 36
RTC 4.4 158
VLZ 4.4 63
ESTP 4.2 151
SESP 4.1 166
SELV 4.1 38
MDT 4.1 67
AVE 4.1 123
EMAL 4.1 300
GORA 3.9 143
VELZ 3.8 204
PVAQ 3.8 222
PAB 3.8 591
GGNV 3.8 57
TOL 3.7 140
PESTR 3.7 116
EVO 3.6 197
JAND 3.6 27
HORN 3.6 117
MORF 3.5 67
ARAC 3.5 112
PFVI 3.4 140
MTE 3.4 333
ANER 3.4 116
IFR 3.4 138
MESJ 3.2 28
ORGV 3.1 35
ASCB 3.0 105
ELUQ 3.0 49
MELI 2.6 234
CFS 2.5 20
CART 2.3 276
ACBG 2.3 39
ACLR 2.2 47
ALB 2.1 46
0 5 10 15 20 25 30
TIME (s)

Figure 18: Stacked PRFs from 37 stations shown in figure 13A. Traces are band-pass filtered with a bandpass of 0.1-1 Hz and distance move-out-corrected corresponding to a reference epicentral distance of 67 deg (fixed slowness 6.4 s/deg). The P-to-S Moho converted phase can be clearly recognized at most stations as indicated by a green line. However, the summation traces of some seismic stations (EMAL, GORA, SELV and SESP) are fairly complex. They are especially characterized by the weak or even nonexistent Moho arrivals. In this case, the possible Moho phases were identified by comparing both the PRF- and SRF-waveforms in order to avoid mislabelling Ps phases. The multiple reflected phases for some traces are missing or difficult to identify. Zero time is the P wave arrival. Amplitudes of traces are normalized. Station code and Moho conversions times as well as the number of the receiver functions used are given in the panel on the left and right side for each of the traces, respectively. Arrival times from Moho vary from 2.1 to 4.9s.

4.5 Estimation of the crustal thickness from PRFs

From PRFs results, the crustal thicknesses for 37 sites located along the area of study were finally estimated (figure 19). The Moho depth determined for each station using the IASPI91 model is given in the Appendix B. In order to create a Moho map for the area under investigation, the time difference between the direct (primary) P-wave and the Moho converted (secondary) Ps-wave was measured first (figure 18). In the next step, the resulting times were converted into the depth domain in order to estimate the depth to the converting Moho interface, using an average crustal P wave velocity of 6.5 km/s, corresponding to the IASPI91 velocity model.

Even if a considerable number of the stacked receiver functions show clear crustal multiple arrivals, they are not taken into account when determining the Moho depth. Crustal thickness ranges from 16 km to 40 km in the area of investigation. The crust appears to thicken from the east (16 km) to west (40 km) along the Alboran Sea region. The thickest crust is found below the westernmost part of the Betics and the northern part of the Gibraltar arc (40 km). Relatively shallower crustal thickness observed beneath the Alboran Sea, northernmost Africa, as well as the southernmost Iberian Peninsula, is interpreted to confirm the extensional nature of the plate boundary between the Iberian and African plates. Data also suggest that the high topography in the area investigated appears not to coincide with the thickest Moho depths.

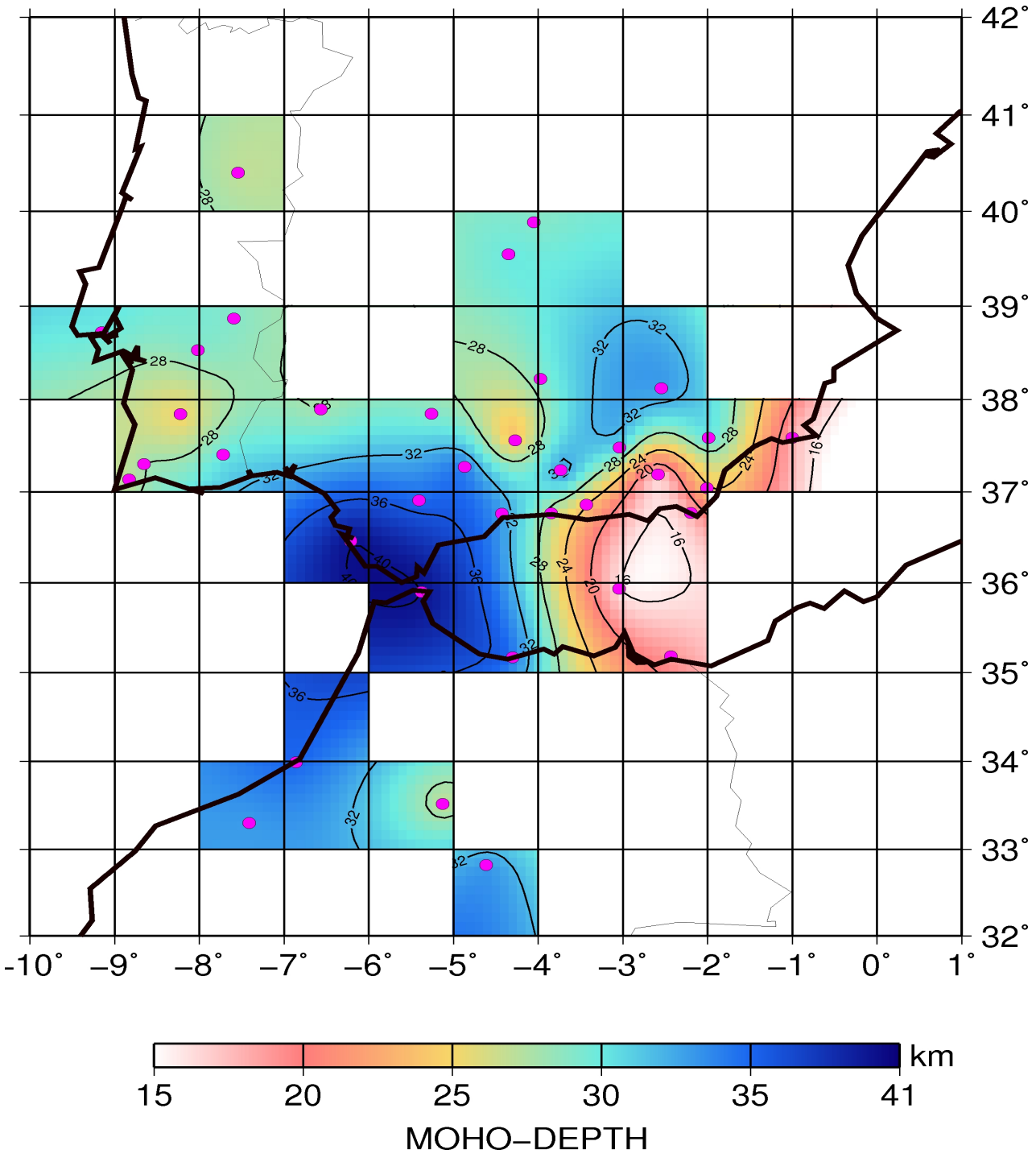

Figure 19: PRFs derived Moho map. The Moho depths are estimated bases on the observed time difference between the direct P-wave and the Ps-phase, using an average velocity model for the crust (Vp = 6.5 km/s). A lateral increase is obtained in the crustal thicknesses beneath the area under investigation: Moho depths range from 16 to 40 km, and thicken progressively from east to west along the Alboran Sea. It is clearly seen that the central part of the Alboran Sea has the thinnest crust. The largest crustal thickness is observed in the westernmost Betics near the Gibraltar.

4.6 Discussion

Results derived from PRFs revealed that the variation in the crustal thickness between the Betic-Gibraltar-Rif area and Alboran Sea is very abrupt in areas near the current coastlines. The largest crustal thickness was observed beneath the Gibraltar arc (40 km) in the vicinity of the westernmost Alboran Sea, and beneath the northern part of the central Betic (33 km). These observations differ significantly from previous studies. For instance, using gravity and seismic data, WGDSSA (1978) and Hatzfeld et al. (1980) concluded a crustal thickness of 35 and 38 km for the Gibraltar arc and the central Betic region, respectively.

Our data also indicated that a thin crust with an average value exists in the central part of the Alboran Basin (16 km) and in the easternmost part of the Betic Cordillera (22 km). This can be attributed to the extensional nature of this area. These findings are consistent with previous seismic refraction studies and two dimensional gravity modelings in this region (Hatzfeld 1980; Banda and Ansorge 1980; Torné and Banda 1992; Banda et al. 1993; Watts et al. 1993).
We found the Moho discontinuity to be reached at around 30 km in the Iberian Massif that bounds Betic Cordillera to the North (the central part of the Spain). This differs slightly from the result (32 km) of Banda et al. (1981; Surinach and Vegas 1988).

Stations situated on the southern edge of the Portugal yield an average crustal thickness of approximately 30 km which generally agrees with the Moho depth values inferred from a large number of seismic refraction and wide-angle reflection experiments (Müller et al. 1973; Sousa Moreira et al. 1978, 1983; Mendes Victor et al. 1980; Palomeras et al. 2008)

We derived an average crustal thickness of 34 km under the Rif and Atlas Cordillera, which agrees reasonably well with the results from other seismic refraction and gravity studies (Demnati 1972; Schwarz and Wigger 1988; Wigger et al. 1992). This result is also fairly compatible with the observation obtained from the integration of elevation and geoid anomaly data with a thermal field (Fullea at al. 2010) (see figure 6A).

Chapter 5

Lithospheric thickness variations obtained from SRFs analysis

5.1 The base of the lithosphere

In the 1912, A. Wegener postulated the theory of the continental drift, stating the horizontal displacement of the continents. The major conclusion of this theory was that some 200 million years ago a supercontinent, Pangaea, existed, which broke up into smaller landmasses, and formed the continents and sub-continents, practically as we know them today. The reasoning behind this hypothesis relied on the observations of the similarities in the fossils, animals, plants and geological records shared by Africa and South America, in conjunction with the apparent similarities in the coastlines of these two continents. From these facts, he concluded that these two continents must have been united in the past and had somehow come to be separated. But, unfortunately, Wegener could not convincingly suggest any mechanism that would have caused the continents to break apart and move around in this way.

In the 1960's, the modern theory of plate tectonics was developed, based on new data from the sea floor, including deep sea topography and the magnetism of seafloor rocks. Seafloor spreading was proposed as a mechanism to drive the movement of the continents on the basis of symmetrical patterns of reversed and normal magnetic rocks on the sea floor. In the context of the plate tectonic theory, continental drift is explained by the movement of lithospheric plates over the asthenosphere. In light of this new concept, the lithosphere is theorized to be the upper rigid layer of the Earth, including the uppermost, solid part of the mantle along with the overlying crust. On the other hand, the asthenosphere is defined as a highly viscous and mechanically weak ductile deformed region in the upper mantle, underneath the lithosphere.

Separating the lithosphere from the asthenosphere, the base of the lithosphere (or lithosphere-asthenosphere boundary, LAB) is treated as the kinematically defined lower boundary of tectonic plates. There is broad agreement that the deep topography of the LAB

can be used as a proxy for the lateral lithospheric thickness variations inside the Earth, providing valuable clues on the mantle dynamic.

From a seismological point of view, the lithosphere is generally interpreted as a seismic high velocity layer above the low velocity zone in the upper mantle (asthenosphere). The lithosphere-asthenosphere discontinuity is attributed to the transition from a high velocity lid beneath the Moho to the asthenospheric low-velocity-zone (LVZ) in the upper mantle. This discontinuity is marked by a decrease in seismic P- and S-wave velocities (impedance decrease), presumably due to the presence of small amounts of molten rock (partial melting) or temperatur effect (Rychert 2005).

Most information about the thickness of the lithosphere has been derived from the surface wave dispersion studies conducted so far (e.g., Leeds et al., 1974; Ekström and Dziewonski, 1998; Netzlets and Dziewonski, 2008). But these studies suffered from a lack of resolution, due to the long-period character of surfaces waves. In the framework of this study, teleseismic body waves (S and SKS) are employed to generate relatively high resolution data for better resolving the LAB depth across the target area.

5.2 SRFs Data

In this study, the SRF method was applied to a large amount of data located at epicentral distances ranging between 60°-85° for S-waves and 85°-120° for SKS-waves, respectively. To resolve the lithospheric structure, all of the available broadband data from 37 temporary and permanent stations were used. The station locations and the geographical distribution of the teleseismic events used in this study are shown in figure 20A and 20B, respectively.

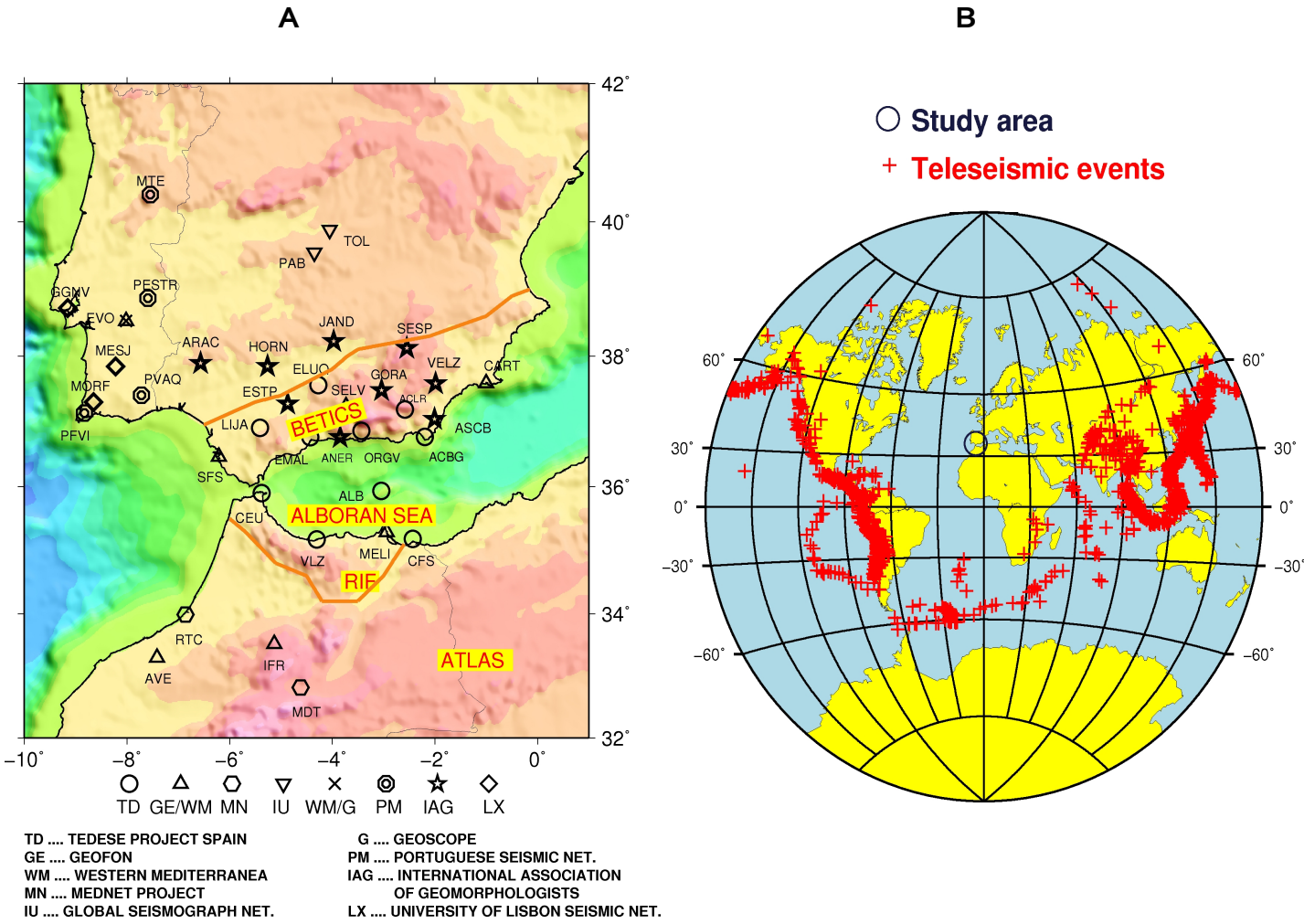

Figure 20: (A) Map of the location of broad-band stations used in the present SRF analysis. **(B)** Map showing the distribution of teleseismic events used. Most of the selected teleseismic events come from the circum-Pacific seismic belt along the margin of Central and South America and on the other side of the Pacific along the Aleutians, the Kuriles, Japan and the Philippines islands.
The crosses and circle indicate the teleseismic events and the location of seismic stations, respectively. The best azimuthal coverage is obtained from westerly and easterly directions. Hypo-center data of earthquakes was collected from the NEIC CMT catalogue.

The representative back-azimuthal distribution of the teleseismic events recorded at each station is represented in the diagrams shown in figure 21.

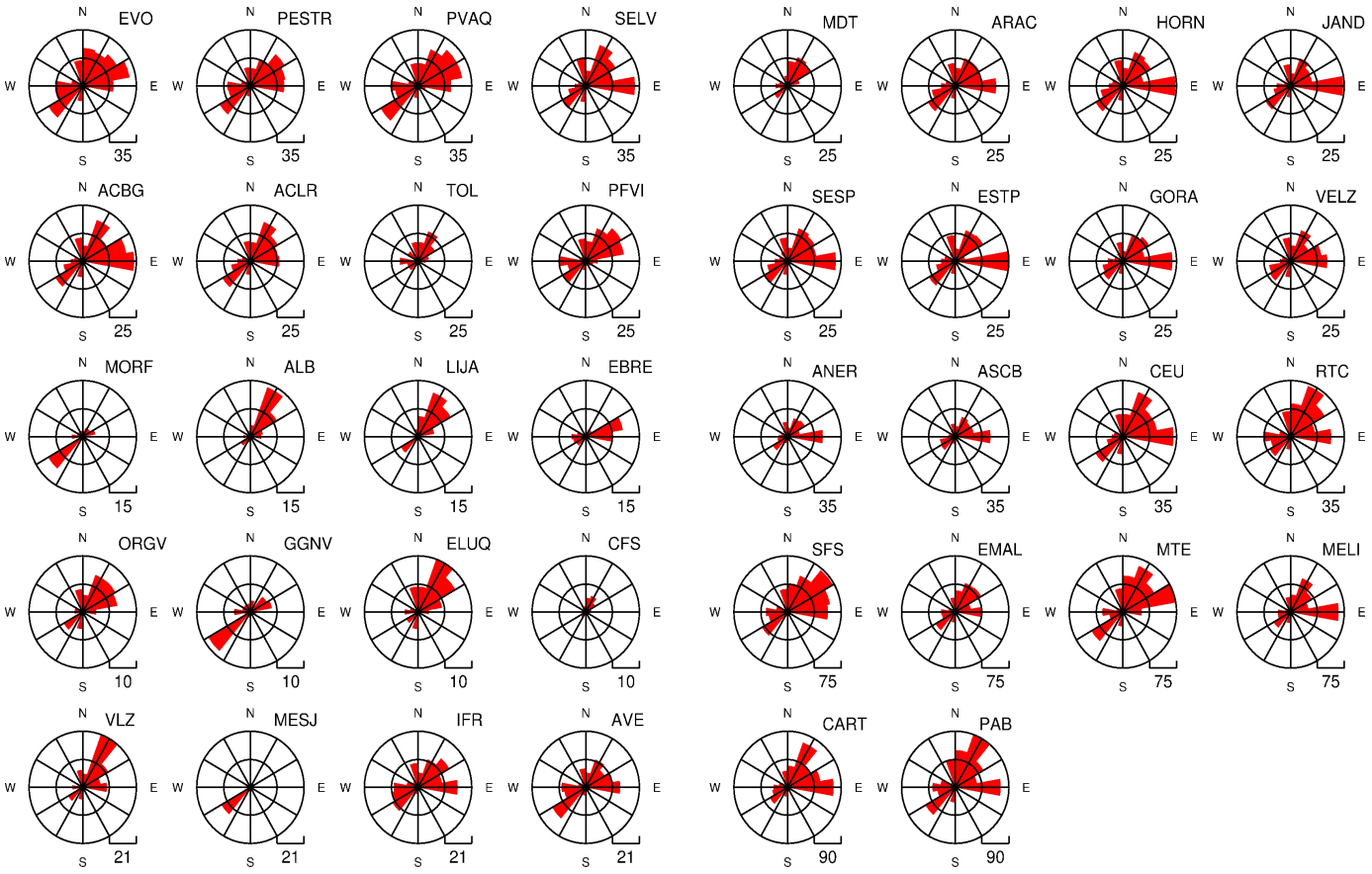

Figure 21: The diagram shows the azimuthal distribution of teleseismic events recorded at the corresponding station. Each ring represents the number of events which is shown on the bottom right-hand side of each diagram. The orientation is binned in 30 degree increments.

To give a general overview of the parameters of events used in the SRF analysis, the teleseismic events are also plotted in figure 22 in terms of depth, magnitude, back-azimuth and distance. For this study, seismograms from events in focal depths ranging between 1 and 650 km are used. But most of the data are obtained from shallow and intermediate-depth events less than 60 km. Some deep-focus earthquakes (below 300 km) are also used, with epicenters as deep as 650 km. The observations covered particularly a range of magnitudes from M=5.7 up to M=7. The epicenters of earthquakes tend to concentrate in the event-station distance range between 80° and 105°. The best coverage is found in the sectors from 5° to 90° and 230° to 360°.

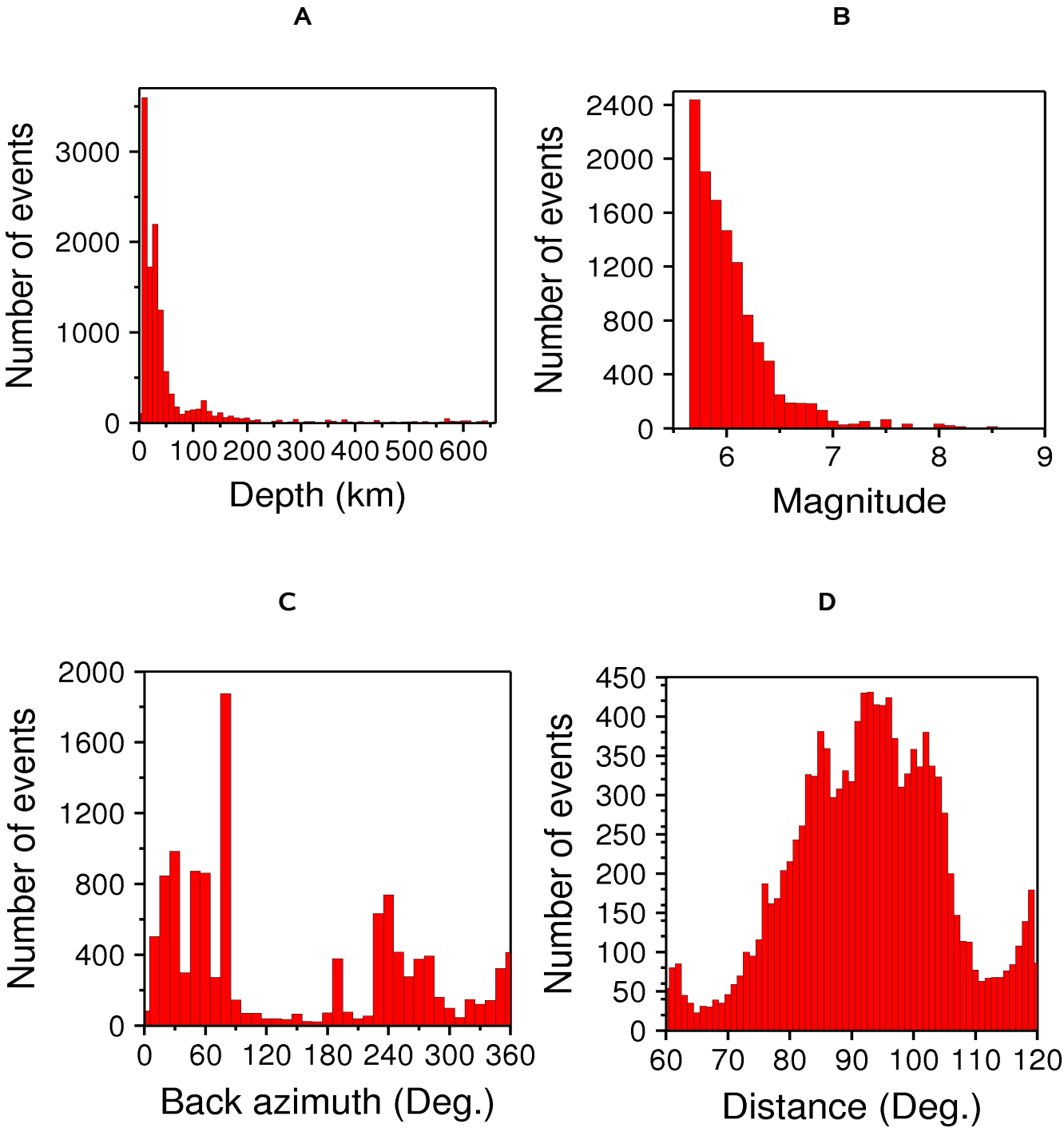

Figure 22: Histogram showing some essential parameters of the teleseismic events used in the SRFs analysis. Presented here are the distribution of focal depths **(A)**, magnitudes **(B)**, back azimuths **(C)** and epicentral distances **(D)**.

5.3 Data examples

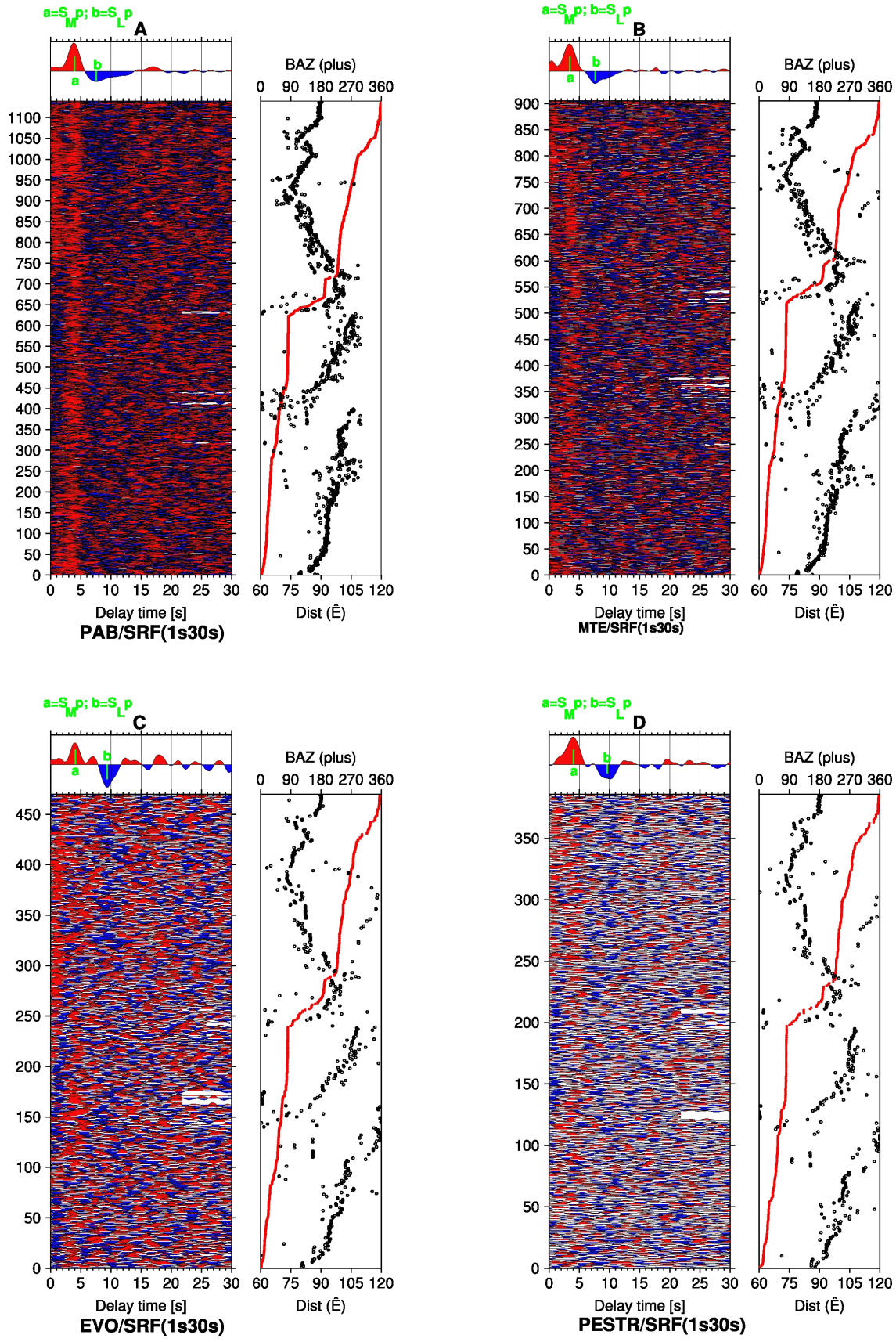

Figure 23: SRFs obtained for the stations PAB (**A**), MTE (**B**), EVO (**C**) and PESTR (**D**). The top panel of each figure show the stacked SRF, whilst the bottom panels of each figure represent individual SRFs that are ordered according to the back azimuth. Similar to PRFs studies, a reference slowness of 6.4 s/deg was used to correct traces for epicentral distance/slowness, before the summation. The polarities and the time axis of the individual traces were additionally reversed in order to be able to compare the SRFs directly with PRFs. The traces were band-pass filtered with a bandpass of 0.03-1 Hz. The two most prominent phases were labeled. The first strong positive "S_Mp" arrivals were generated at the base of the crust (Moho), whilst the second negative "S_Lp" arrivals stemmed from the bottom of the lithospheric discontinuity structure. Positive and negative amplitudes are shown in red and blue colours, respectively. The numbers of the summed receiver functions are given in the panel on the left side for each figure.

To be able to make the P-to-S and S-to-P differential times comparable to each other, and to demonstrate the quality of the SRFs data, the individual and summed SRFs, computed for the same stations PAB, MTE, EVO and PESTR, are plotted in figure 23, as they were presented above as PRFs data examples in figure 17. For each station, we clearly observe coherent positive phases at about 3 to 4s (a) and pronounced negative phases at approximately 7 to 10s (b), which are interpreted to be converted signals from the Moho and the LAB, respectively. The SRFs displayed correlate generally very well with the exemplified PRFs data in terms of conversion arrivals from the Moho interface. However, the crustal multiples, when using the PRFs, seem to interfere with LAB phases that generated at the base of the lithospheric mantle. Therefore, the making of comparison/interpretation related to lithospheric structure is avoided by applying the two types of RFs. Using the IASP91 Earth model, a lithospheric thickness is deduceted from approximately 70 km beneath the stations PAB and MTE to 95 km beneath the stations EVO and PESTR in the central Iberian Massif.

5.4 Summation traces of SRFs from all stations

In a further step, the SRFs stacks generated for all thirty-seven stations are displayed in figure 24, which are sorted with respect to increasing arrival times of the LAB phase. On most station stacks, strong positive conversions from the intra-crustal structure (not labeled) and the Moho interface (S_Mp) within the first four seconds can be clearly observed. Additionally, strong negative phases from LAB (S_Lp) are detected at delay times varying

from around four to thirteen seconds, as denoted by the green line. It is important to remark that for the stations AVE, SESP, MORF and IFR the S_Lp signal is more complex than others.

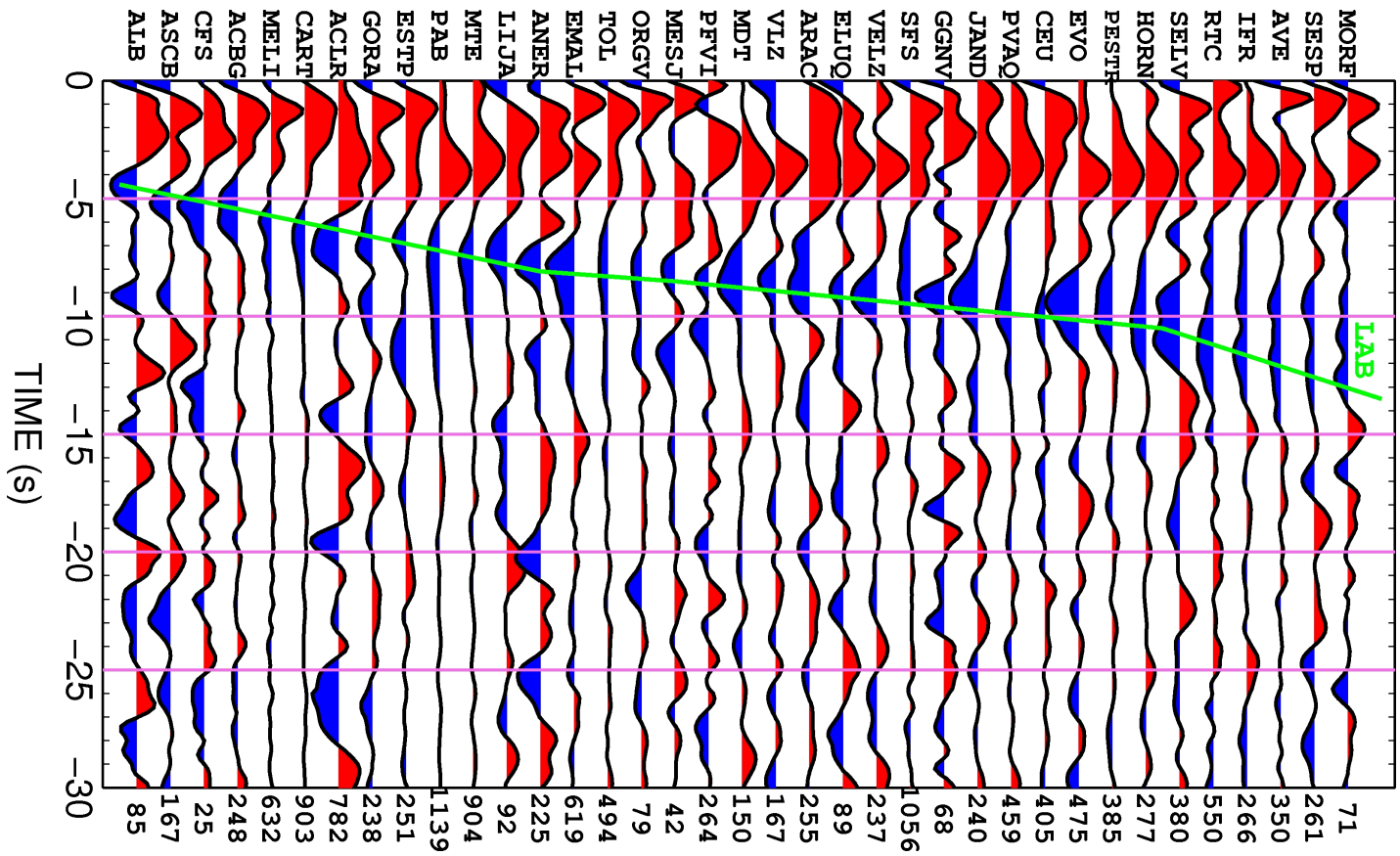

Figure 24: SRFs stack for each of the seismic stations examined in this study. The summation traces were bandpass filtered between 0.3 Hz and 1 Hz, and arranged with increasing LAB time. Peak amplitudes were normalized to unity. In the majority of cases, converted signals from the Moho and the LAB can be clearly seen. A continuous green line marks the conversion signal generated most likely from the LAB. The time axis is valid for slowness of 6.4 s/deg due to moveout correction. Zero time is the arrival time of the direct S- and SKS-phase. Negative time scale indicates times in front of S- and SKS-arrival. The station codes and number of SRFs produced are shown on the left and right side for each summation traces, respectively.

5.5 Common conversion point summation

The RFs can be alternatively summed by performing the common conversion point (CCP) stacking technique to improve the signal-to-noise ratio, if dense station coverage exists in

the area of study. This well-known summation approach permits us to investigate the spatial variation of the subsurface structures within the Earth's interior in greater detail by stacking many RFs that sample nearly the same subsurface point. In this context, for detailed imaging of the LAB-topography along the area under investigation, the geographic distribution of the S-to-P and SKS-to-P conversion points is first determined under the assumption of a common conversion depth of 100 km, using the IASP91 Earth reference model. The station locations and the calculated corresponding piercing point distributions are displayed in figure 25.

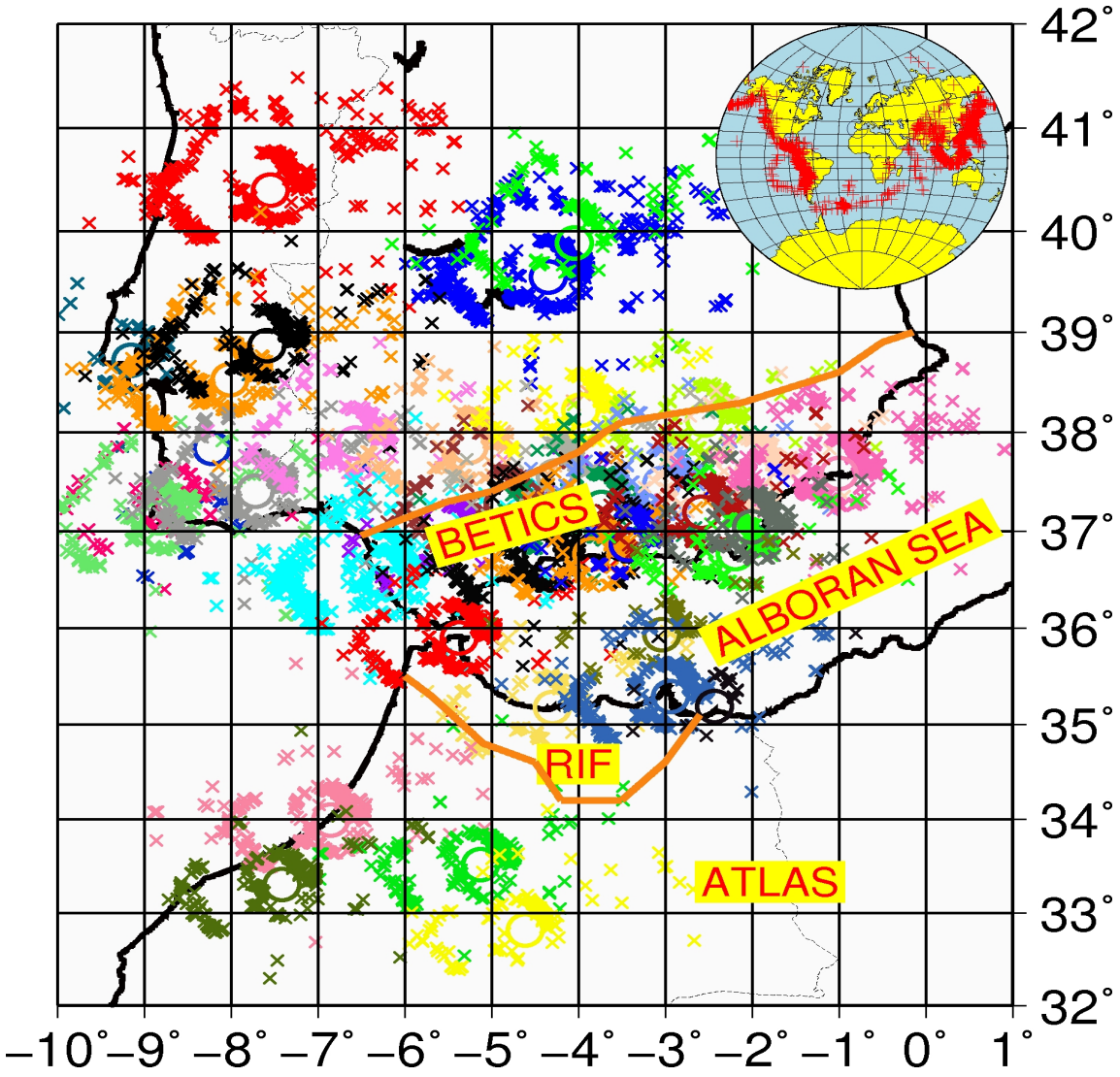

Figure 25: Note that the S- and SKS-phases at a station sample different areas. The piercing points of SKS are located in a region with about 90 km diameter around the station. In contrast, the piercing points of S are located in a region with about 220 km diameter around a seismic station. The inlet shows the global locations of teleseismic events selected within the epicentral distance range of 60°-120°.

In the next step, the S-to-P and SKS-to-P conversions points within the grids of 1°X1° were geographically grouped. Afterwards the corresponding SRFs within these defined bins were stacked. From the resulting summation traces, we produced cross-sections in both east-west (figure 26A) and north-south (figure 26B) orientations throughout the area of interest, and projected them to corresponding grids on the map view. Doing so, we created two image maps views showing the first 20s of the yielded summation traces (figure 26). In these images below, we clearly observe a positive (red) and a negative strong peak within the first 10s of each stacked SRFs, which were interpreted to represent the conversions from the Moho and the LAB interface, respectively. To show the frequency dependence of the stacked traces, we also would like to plot the horizontal and vertical cross-sectional view of the area of study by applying two different band-pass filters at 1s30s and 3s30s, as shown in figure 1 and 2 of the Appendix C of this work, respectively.

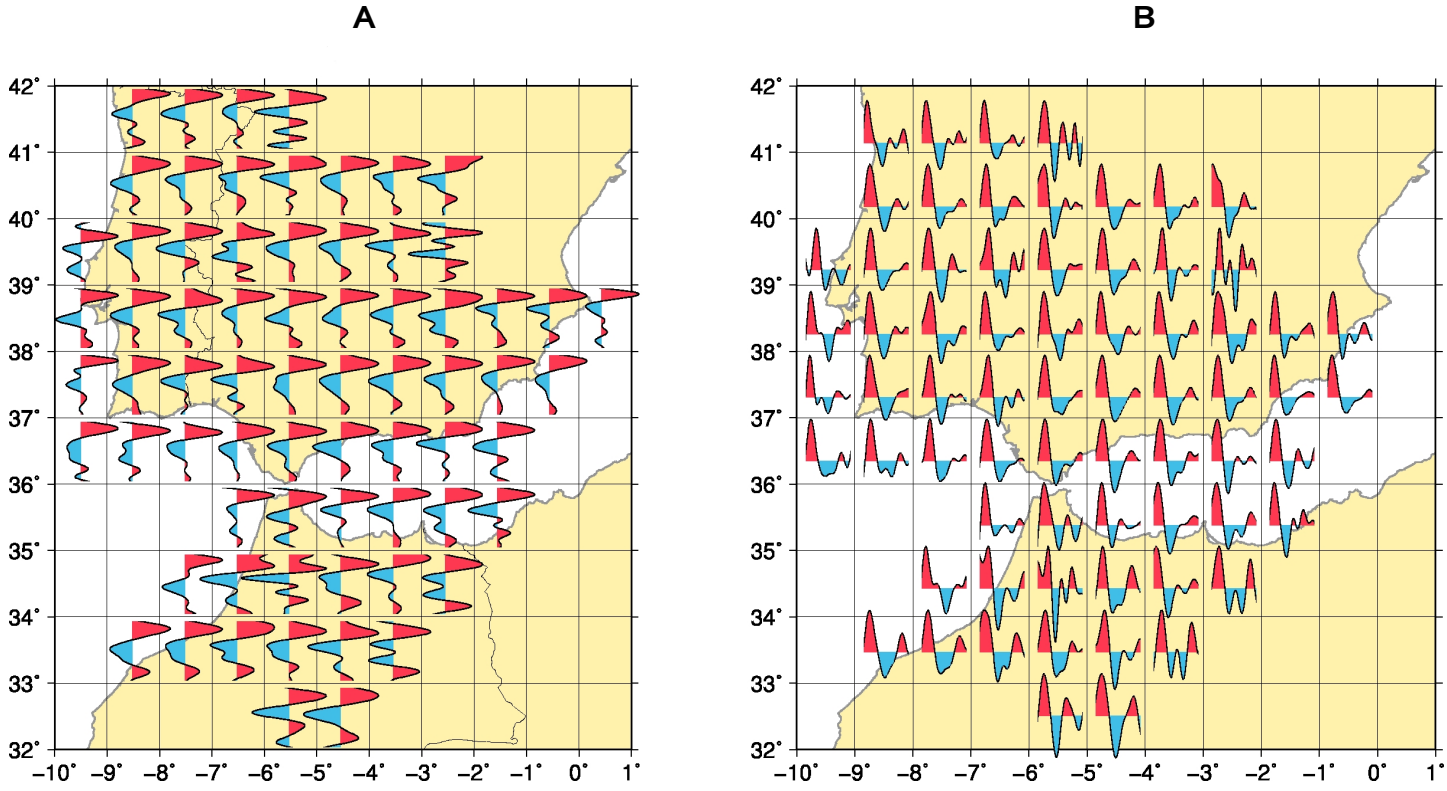

Figure 26: Image map showing the stacked SRFs along the horizontal **(A)** and vertical **(B)** cross-sections. The first 20s of the summed traces were plotted, representing regional variations of the Moho and the LAB structure along the area under investigation. To suppress unwanted background noise, the stacked traces were band-pass filtered between 5-30s. Each trace is normalized to unity. The positive (first) and negative (second) arrivals are generally accepted to be the conversions generated at the major discontinuities i.e., the Moho and LAB. Positive (negative) amplitudes indicate velocity increase (reduction) downwards.

To further improve the signal-to-noise ratio, in the next step, the stacking with the sliding-window technique was applied. For this purpose, the previous grids of 1°X1° were firstly subdivided again into sub grids containing 0.3°X1°. Secondly, the individual traces were averaged by summing within the time window of length 0.3° (ca. 33 km). Thirdly, the time window was moved by 0.1° (ca. 11 km) in order to generate a new summation trace. Finally, the corresponding summation traces were projected to corresponding grids in the map view.

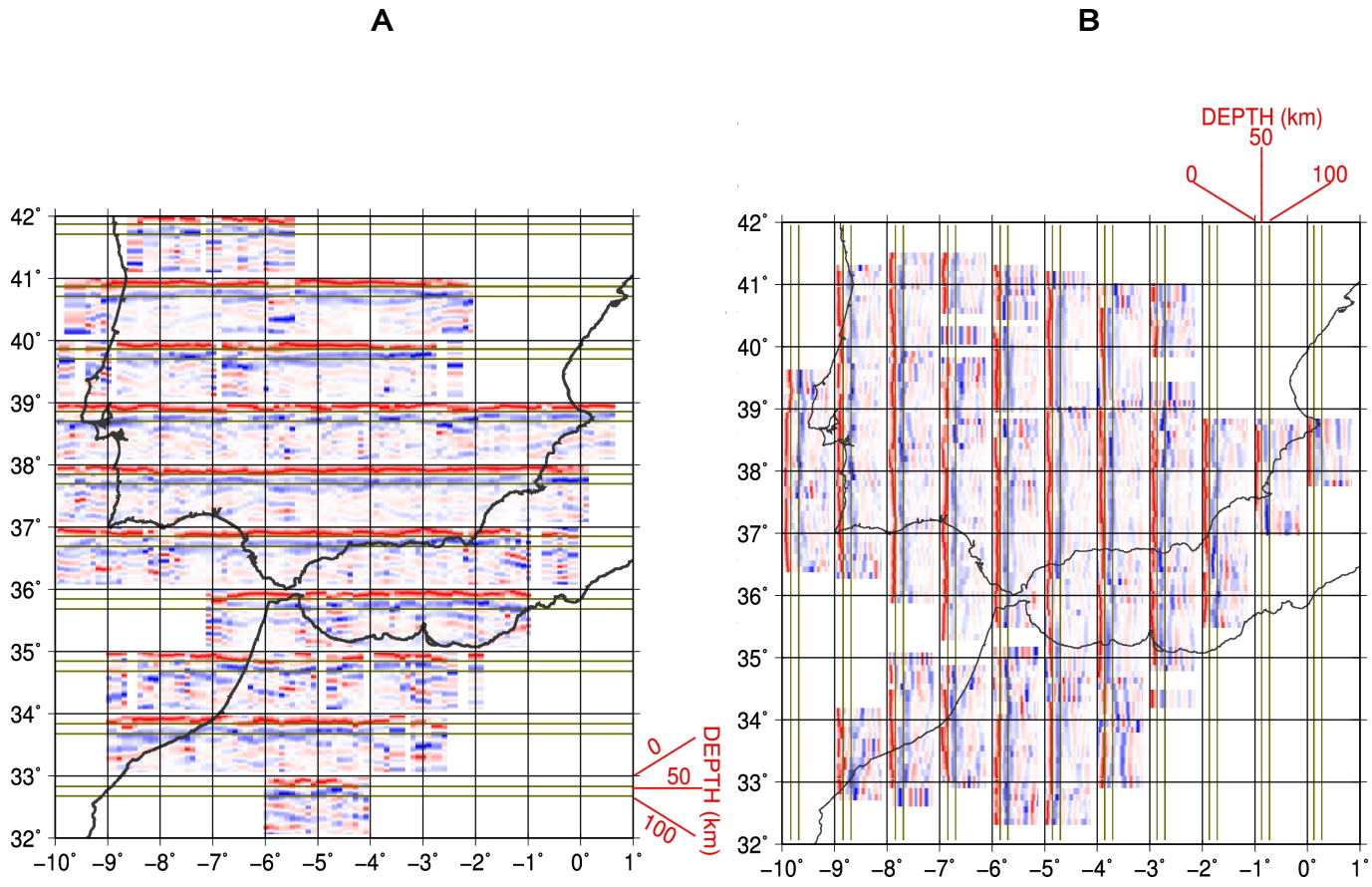

Figure 27: E-W (horizontal) **(A)** and N-S (vertical) **(B)** directed cross sections over the whole the subject area; they were created on the basis of the sliding window technique. The stack bins were designed 0.3° (33 km) with 0.1° (11 km) overlap. Summation traces were equally spaced and sorted by longitude and latitude of the corresponding SRFs piercing-points and were calculated for a depth of 100 km. Individual traces were band-pass filtered with the frequency range between 0.03 Hz and 0.2 Hz. The gray lines indicate a time delay 5s (~50 km) and 10s (~100 km).

In doing so, we created all the possible longitudinal cross-sections in the east-west direction (figure 27A) as well as latitudinal cross-sections in the north-south orientation (figure 27B) running over the whole target area to give a general overview of the main structural units of the study region. It is apparent, from the figures below, that the Moho discontinuity (red) and

the LAB (blue) are clearly visible along the entire profiles, and are continuous features under the entire study area. The two lines plotted denote the 50 and 100 km depths, corresponding roughly to 5 and 10s delay times.

5.6 The thickness of the lithosphere inferred from SRFs analysis

The timing between the direct S and SKS and converted S-to-P and SKS-to-P phases, respectively, is a function of the average crustal seismic velocity and crustal thickness. By using the time delay between the corresponding phase pair, the spatial distribution of the LAB thickness can be seismically constrained under the assumption of a known velocity. On the basis of the stacked SRFs obtained for each defined 1°X1° grid boxes, shown in the figure 26A and 26B, a contour map was created indicating lateral variations of the lithospheric thickness of the area of investigation (figure 28). In Appendix D, the corresponding calculated LAB depth values for each grid are displayed.

From the map below, one can infer five facts regarding the LAB depth distribution in the area under investigation.

- The lithospheric thickness along the area of study varies considerably.

- The seismic LAB is the shallowest beneath the eastern and central Alboran Sea as well as the central and eastern Iberia (70 km) and the northern part of Africa.

- Across the Alboran Sea, the LAB thickness is getting progressively thicker (90 km) from east to west.

- Below the south-west region of Spain and in the Atlantic Ocean, the thickest lithosphere in the region under investigation was found, measuring 100 to 110 km thick.

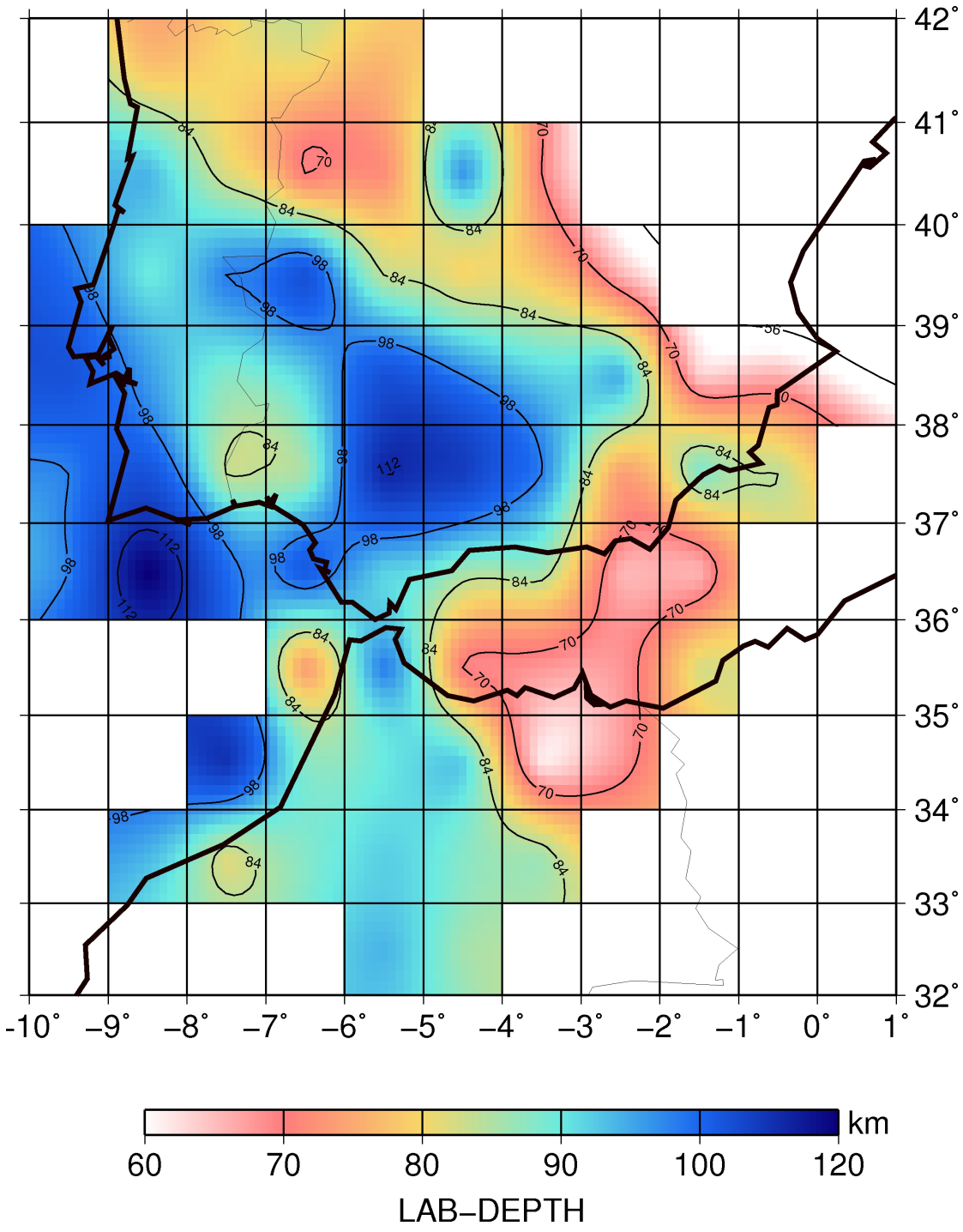

Figure 28: Variation of the thickness of the lithosphere across the area of study, as being determined by teleseismic SRFs analysis. SRFs were mapped to depth via the common conversion point stacking technique. For this purpose, the stacked SRFs lying in grids of 1°X1° were used. The lithospheric thickness varies considerably. Beneath the eastern and central part of the Alboran Sea, the lithosphere is the thinnest in the area of study. In contrast, the SFRs results indicate a substantially thicker lithosphere underlying the south-western part Portugal and the neighbouring Atlantic region.

5.7 Discussion

Our SRFs data documented clearly the presence of a thin LAB with an average thickness of between 70 and 80 km in the central Alboran Sea region. This results are in general agreement with the joint analysis of elevation, gravity, geoid, surface heat flow, and seismic data performed by Fullea et al. 2010, as well as with the gravity modeling conducted by Torne et al. 2000. On the other hand, the thickness of the lithosphere outlines a systematical increase from east to west until it reaches its maximum value (90 km) beneath the Gibraltar Strait along the Alboran Sea basin. This trend was also observed by Iribarren et al. 2007 and Fullea et al. 2010 (see also figure 6B). Differing from our results, however, they suggested a lithospheric thickness of about 130-190 km beneath this region.

We also found a relatively thin lithosphere of around 80 km for the Iberian Massif in central Spain, which also increases tendentially in the NE-SW direction towards the Atlantic Portugal Margin, reaching a maximum thickness 120. Our observation made for the central Iberia agrees partially with the results of Badal et al. (1992) and Martinez et al. (2005), who placed the base of the lithosphere at a depth of 80 km for the entire Iberian Peninsula region.

We also observed a thinning of the lithospheric mantle along the Rif and High-Middle Atlas in north-western Africa (90-100 km) compared with the southern part of the Iberian Variscan Massif (100-120 km). A similar observation was also documented by Fullea et al. 2010 for the High-Middle Atlas (90-100 km). However, they suggested a lithospheric thickness of 210 km beneath the Gulf of Cadiz in the easternmost part of the Atlantic Ocean, which differs significantly from our results (120 km).

5.8 Taking three profiles in the target area based on SRFs data

In addition to 1°X1° grid analysis, the area of study was also investigated, taking three profiles in the light of the SRFs, whose geographical distributions were determined by using the common conversion depth of 100 km, as explained above (see 5.5). In this case, the region under investigation was first subdivided into much bigger boxes, each greater in size than the 1°X1° grid. This aids in focussing on larger-scale structural features. Afterwards, the resulting individual SRFs were stacked within the newly defined corresponding boxes.

The aim is to sum more traces in one box and to obtain a better signal-to-noise ratio. However, this is done at the expense of a reduced lateral resolution.

5.8.1 NW-SE profile running perpendicular to the strike of Betics

At first, we took a NW-SE oriented cross-section that cuts perpendicular to the strike of the Betics. The dimension of each box is designed to cover an area of 100 km wide and 400 km long. In figure 29A, we illustrate this created cross section and the distribution of the theoretical conversion points of SRFs that were calculated for a common depth value of 100 km (No.: 2-9). Additionally, we also considered separately southern Portugal and the north-west African region to be able to make a regional comparison in terms of the variation of the LAB depth even if those regions are located outside of the defined NW-SE directed profile (No.: 1;10-11). After designing the boxes and determining the corresponding piercing points within each respective box, as well as the respective regions, the corresponding SRFs were stacked.

To study the frequency dependence of the results, three different types of filters were in turn applied to construct the stacked SRFs for each region:

- band pass filter from 1-30s (29B).
- band pass filter from 3-30s (29C).
- and a bandpass from 5-30s (29D).

The SRFs reveal again that the lithosphere is shallower beneath the Alboran Sea, as indicated by box-2 and box-3. From box-4 and box-5 a north directed deepening of the LAB beneath the Betics may be inferred. Boxes 6 to 9 also indicated a thinner lithosphere in northern Spain. Represented by box-1 and boxes10-11, the African and the Portugal regions correspond to areas where the lithosphere thickness achieves its maximum value. For the calculation of LAB depth, we refer to delay times of the SRFs generated by applying of 5-30s band-pass filters, due to their much clearer, readable travel times.

To estimate the LAB depth, the delay times of the SRFs were taken from the 5-30s band-pass filter, because the clearest converted signals are more reliable in this bandwidth. Within this context, the LAB-depths for each sub-region were separately estimated by multiplicating the LAB times by a factor of 9.5 in respect to the IASP91 model. The measured delay times and their corresponding depth values were also given in figure 29D.

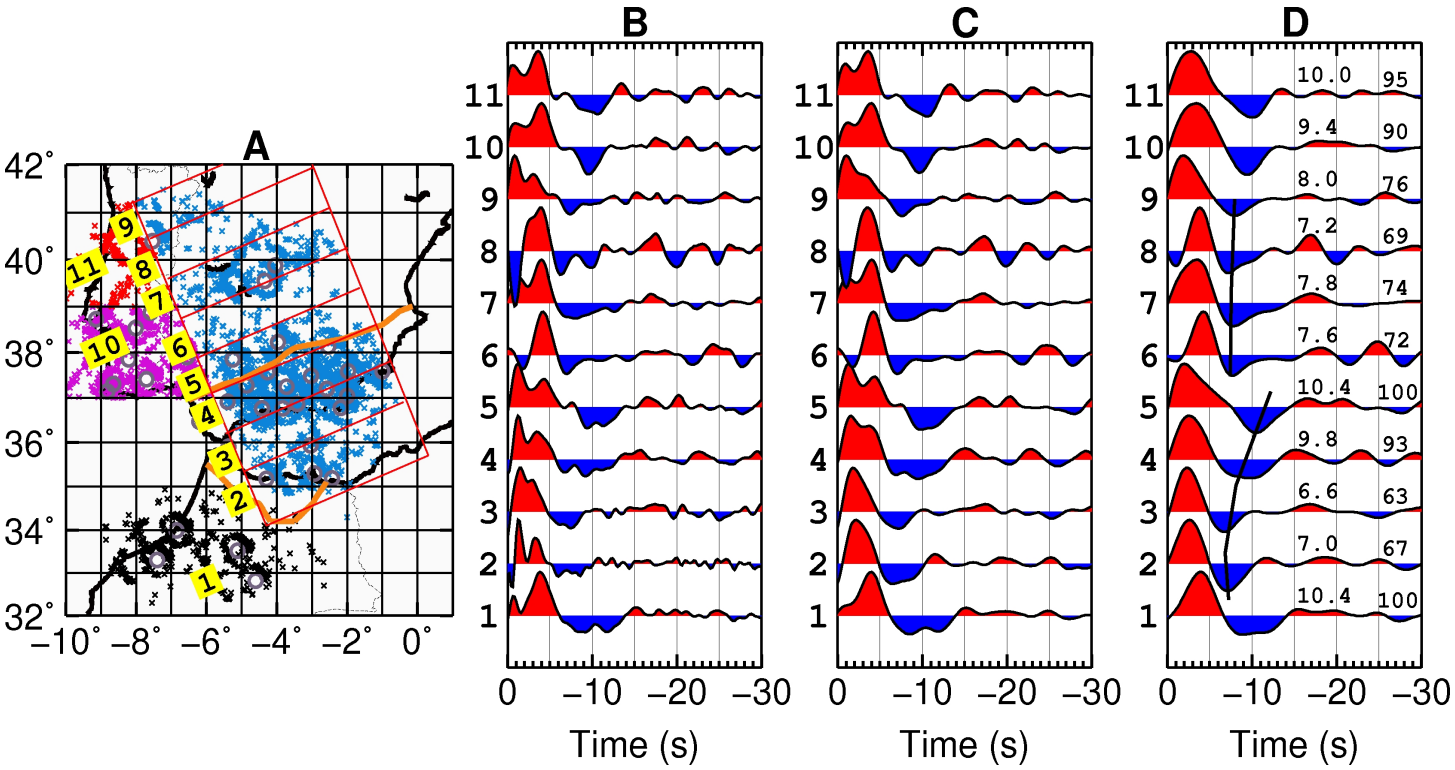

Figure 29: (A) Distribution of the piercing points along the NW-SE cross-section and in other regions, calculated for a common depth of 100 km. **(B, C, D)** Stacked SRFs calculated for each defined sub-regions by using three different band-pass filters (B: 1-30s, C: 3-30s, D: 5-30s). According to the IASP91 reference Earth model, multiplication of the LAB times by a factor of 9.5 gives the approximate LAB depths.

5.8.2 E-W profile through the Alboran Sea

In a second step, we defined an E-W directed cross-section (figure 30A) running through the Alboran Sea in order to probe for the existence of an east-dipping slab, which was previously suggested by several investigators (e.g., Spakman et al. 2004). In this case, we designed 9 boxes, whose dimension covers an area of around 100 km width and 200 km

length. Similarly, we plott this created cross section and the distribution of the theoretical conversion points of SRFs, calculated at a common depth value of 100 km (No. 1-9).

To analyze the frequency dependence of SRFs, we again applied the three different filters to the SRFs within the respective box. The individual traces were band-pass filtered in the following bands: 1-30s, 3-30s and 5-30s, respectively. The corresponding SRFs are illustrated in figure 30B, C, D. From the SRFs results, it can be clearly deduced that the lithosphere is thicker (about 100 km) in the Atlantic near the southern part of Portugal and becomes shallower towards the western Alboran Sea (around 60 km).

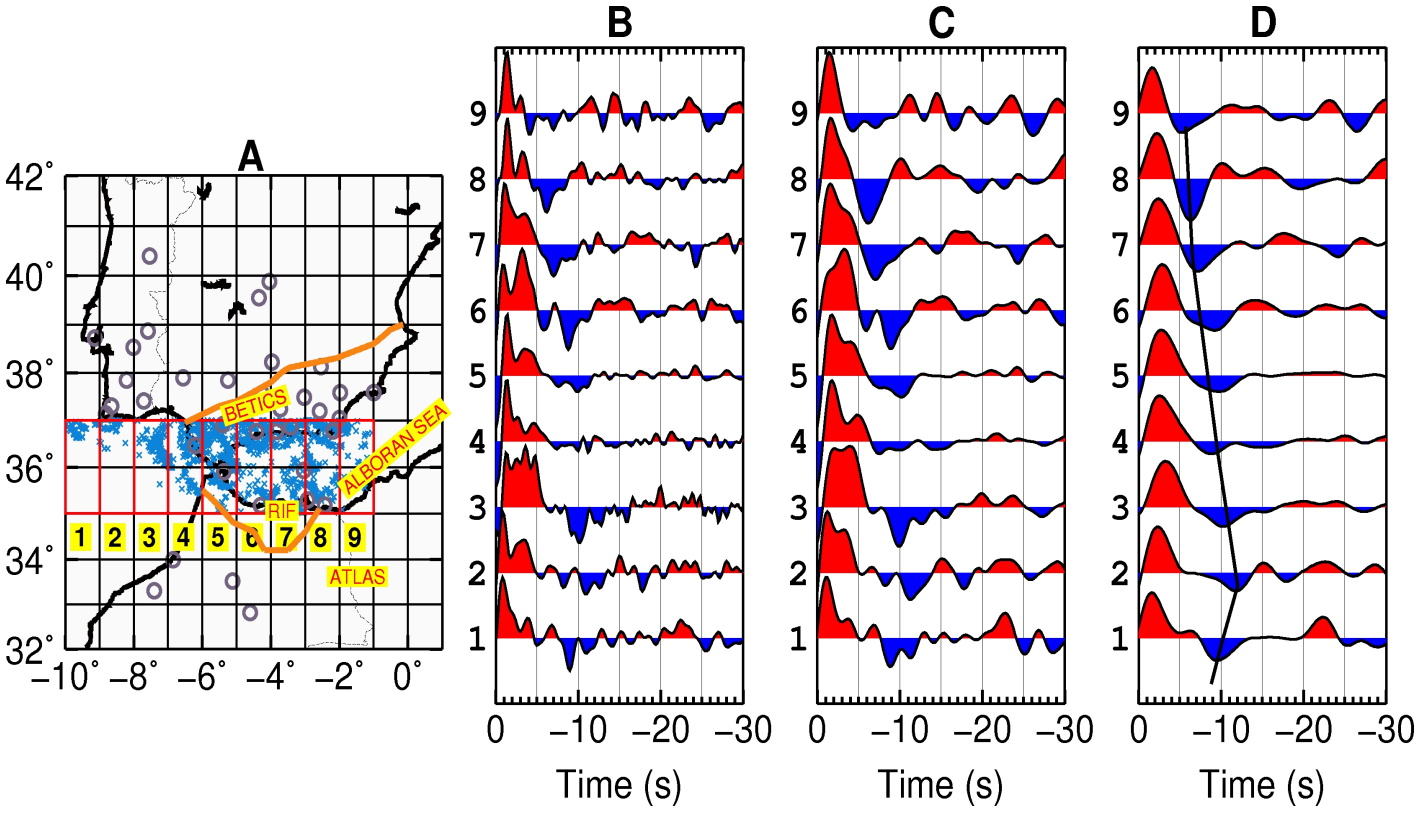

Figure 30: (A) Location of the piercing points along the E-W cross-section running through the Alboran Sea, calculated at a depth of 100 km. **(B, C, and D)** Stacked SRFs computed for each defined sub-regions by using three different band-pass filters. (B: 1-30s, C: 3-30s, D: 5-30s).

5.8.3 SW-NE profile running along the strike of the Betics

Finally, we created a SW-NE cross-section which is directed along the strike of the Betics in order to investigate the variation of LAB depth in the southernmost part of the Iberian Peninsula (figure 31A). Correspondingly, we created nine boxes with dimensions of 100 km width and 200 km length. Similarly to the above-mentioned steps, we first calculated the piercing point locations of SRFs for a depth of 100 km, and then stacked them for each respective box, as shown in figure 32B, C, D. The results clearly revealed that the LAB does not significantly change within this area. The depth to LAB ranges between 90 and 100 km.

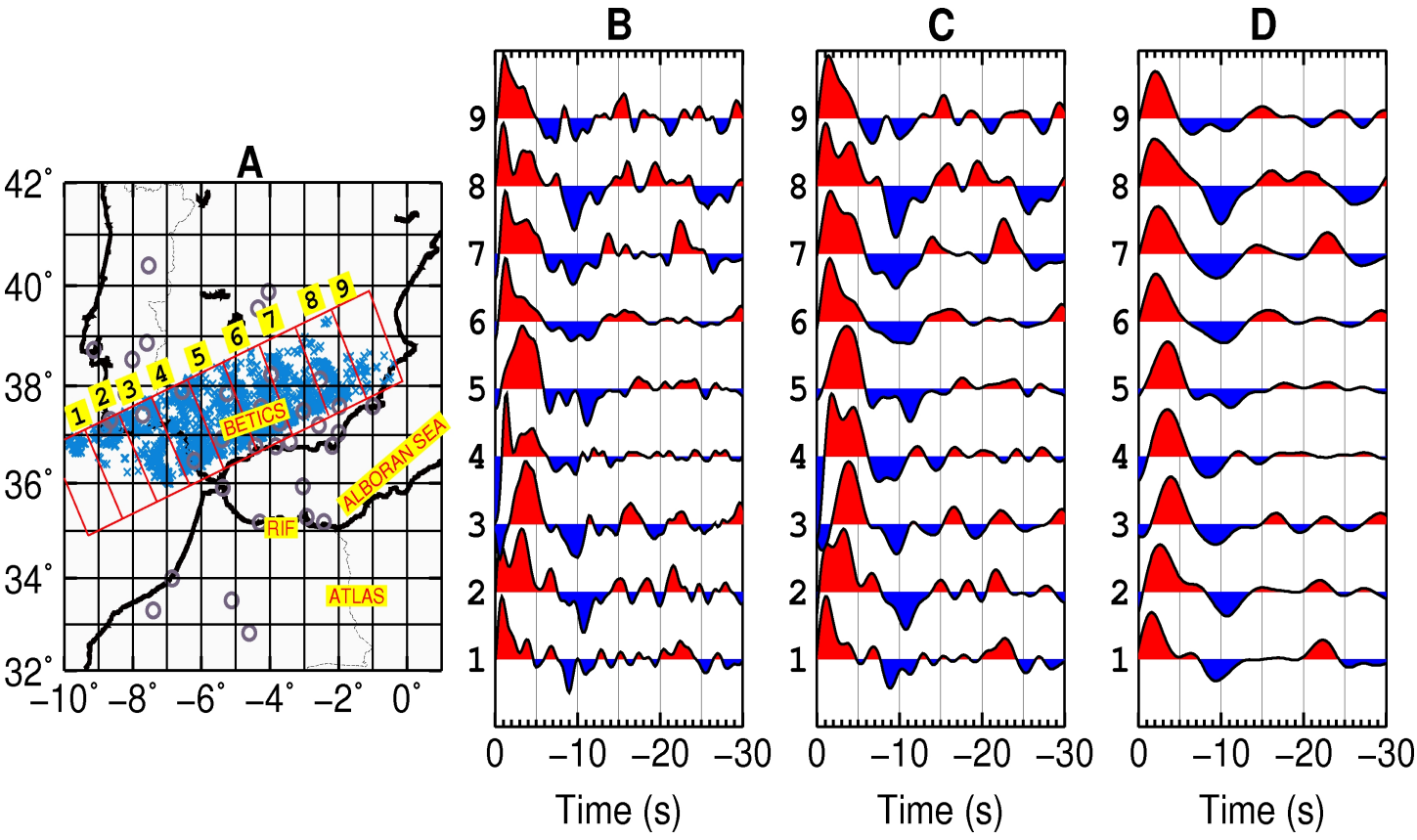

Figure 31: (A) Location of the piercing points along the SW-NE cross-section running along the strike of the Betics in the southernmost Spain, calculated at a depth of 100 km. **(B, C, D)** Stacked SRFs were illustrated by using three different band-pass filters within each defined box (B: 1-30s, C: 3-30s, D: 5-30s).

Chapter 6

Imaging the upper mantle discontinuities using the PRFs analysis

6.1 Introduction

The Earth's mantle is conventionally divided into three major subdivisions: the upper mantle, the transition zone and the lower mantle. The transition zone is bounded by two major seismic velocity discontinuities at approximately 410 and 660 km depths, and detailed knowledge of them is of great importance for a better understanding of the mantle dynamics. Seismic studies carried out extensively during the last decades revealed that these discontinuities are globally observable. In such studies, the spatial variation in the topography of the 410 and 660 km discontinuities was investigated on a regional scale near subduction zones (e.g., Castle and Creager 1998; Gurrola and Minster 1998; Li et al. 2000b), and hotspots (e.g., Dueker and Sheehan 1997; Li et al. 2000a), as well as on a global scale (e.g., Gossler and Kind 1996; Gu et al. 1998; Flanagan and Shearer 1998; Chevrot et al. 1999). Many other boundaries have been reported, but these are smaller or less globally pervasive (Bina 1991).

These key subsurface structures are generally thought to be a result of solid-state transitions of the major minerals of mantle rocks, which are sensitive to temperature and pressure. For instance, the seismic discontinuity at 410 km depth in the Earth's mantle is often related to the transition from the α-phase (Olivine) to the ß-phase wadsleyite of (Mg,Fe)2SiO4 (Ringwood 1970; Ito and Takahashi 1989; Bina 1991; Helffrich, 2000; Shearer 2000; Shim et al. 2001). In contrast, the 660 km discontinuity is generally believed to be caused by an isochemical phase transformation of ringwoodite (the γ phase of (Mg,Fe)2SiO4) to perovskite ((Mg,Fe)SiO3) and magnesiowustite ((Mg,Fe)O) (e.g., Anderson 1967; Ito and Takahashi 1989; Bina and Helffrich 1994).

The tectonic activity in a region is strongly associated with the thermodynamic state of the underlying upper mantle. A detailed knowledge of the mantle transition zone (MTZ) discontinuities is therefore crucial to a full comprehension of processes like subduction and mantle plume upwelling. Associated to relatively hot or cold material in the mantle, variation

in the depth of 410 and 660 km is often considered as a indicator for mantle temperature, which owe their response to thermal perturbation. The upper mantle is generally assumed to be colder under the regions near the subduction zone (slabs) than in regions without subduction. In such cold regions, the 410-discontinuity is expected to be shallower, due to its positive Clapeyron slope, while the 660 km discontinuity becomes deeper because of its negative Clapeyron slope (Collier and Helffrich 1997, 2001; Gilbert et al. 2001).

In the case of a hot upper mantle (upwelling plume), the 410-km discontinuity would be deflected downward, whereas the 660-km discontinuity would be deflected upward (figure 32).

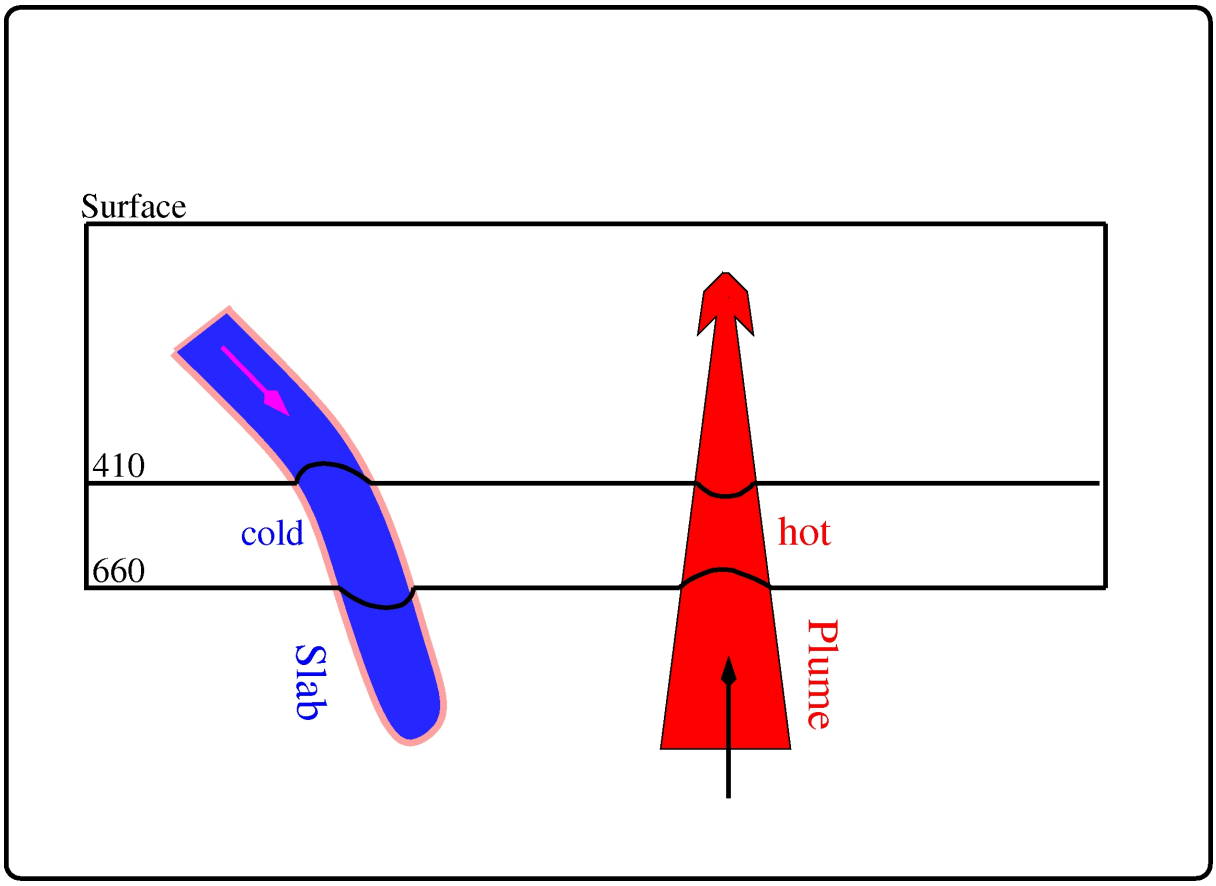

Figure 32: The illustration shows how the topography of the MTZ triggered on each discontinuity by cold (subducting slab) or hot material (upwelling plume), passes through the transition zone. The manner in which a subducted slab or a plume influences the upper mantle can be determined by investigating variations in the depths of the upper mantle seismic discontinuities in the corresponding region.

6.2 Synthetics generated for upper mantle discontinuities

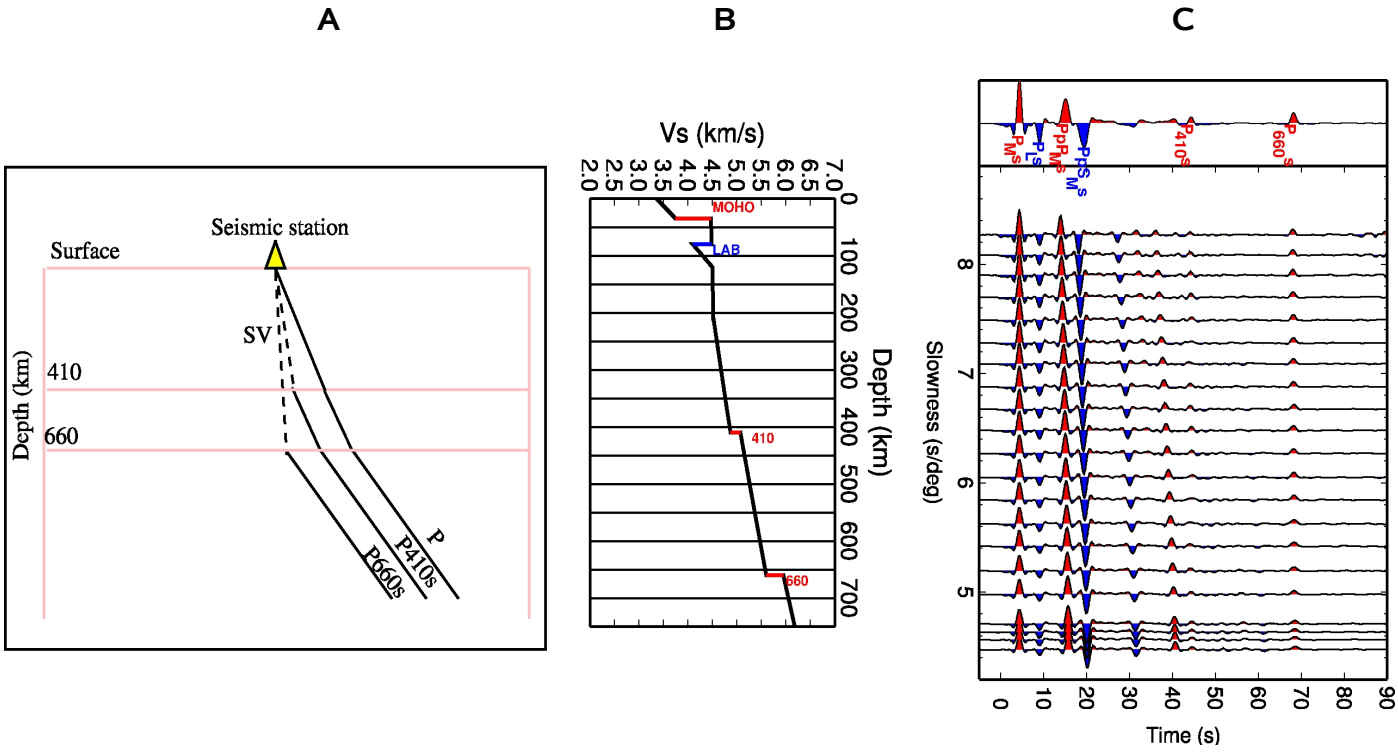

Figure 33: (A) A graphical representation of the conversions from the MTZ discontinuities in the Earth's mantle. **(B)** The modified IASP91 velocity model used in the calculation of the synthetic PRFs. The model consists of four layers: 35 km crust, 80 km lithosphere, 410 and 660 km. **(C)** Synthetic Q-component PRFs generated for a 600 km deep source. The Synthetics feature prominent arrivals from the P-to-S conversions at 410 ($P_{410}S$) and 660 ($P_{660}S$) km depth at 44.1s and 68.0 s, respectively. Note the converted P-to-S phase from the 410 ($P_{410}S$) is rather weaker than that from the 660 ($P_{660}S$). Multiple reflections (P_MS, PpP_MS PpS_MS) and direct conversion (P_MS) from the Moho as well as the direct conversion from the base of the lithosphere (P_LS)are also clearly observable prior to the mantle conversions ($P_{410}S$) and 660 ($P_{660}S$).

Ray paths of direct (P) and converted (P410s and P660s) waves, typically generated at the upper mantle transition zone discontinuities at depths range of 410 and 660 km within the Earth, are illustrated in figure 33A. In order to illustrate the timing and amplitude variations of arrivals originating from the upper mantle discontinuity at 410 and 660 km depths, synthetic PRFs were calculated, utilizing the reflectivity method of Kind (1978). The synthetics were generated applying a modified version of the one-dimensional reference velocity model IASP91, consisting of major layers with four discontinuities at depths of 35 km (crust), 80 km

(lithosphere), 410 km and 660 km (MTZ), as shown in figure 33B. In principal, the synthetic seismic data were processed using the same procedures as used for the original observed data. In figure 33C, the resulting synthetics were plotted in order of increasing ray parameters which span from 4 to 8.4 s/deg.

On the basis of their velocity model (i.e IASP91), Kennett (1991) and Kennett and Engdahl (1991) suggest the arrival times of 44.1s and 68.0s for the converted phases from the 410 and 660 km after the P arrival, respectively. These are characterized by a rapid increase of seismic P- and S-velocities at these depths. They report a velocity increment of +3.6 % and +4.1 % at the 410 km for P- and S-waves, respectively. They assume, on the other hand, a velocity increment of +5.8 % and +6.3 % at the 660 km for P- and S-waves, respectively.

As can be clearly seen in the synthetics, the upper mantle transition zone discontinuities at 410 km and 660 km are therefore relatively less strong boundaries because of the small P- and S-wave impedance contrast in comparison with the Moho. It is also clearly obvious that the amplitude of the $P_{410}s$ is comparatively smaller than that of the $P_{660}s$, making $P_{410}s$ more difficult to detect.

6.3 Data

To examine the upper mantle discontinuity structures ($P_{410}s$ and $P_{660}s$) below the area of interest, we made use of the same PRFs data-set initially used to determine the Moho depth variation along the area of study. It should be noted that this project is concerned only with the geographic variations in the upper mantle discontinuity structure rather than absolute depths of the MTZ discontinuities.

Our data set consists of nearly 5,500 PRFs for 37 seismological stations**.** To get a general idea of the data coverage, and to provide geographical information from a sampled area within the framework of this analysis, we displayed both the station distribution in the area of study and the piercing points of the P-to-S converted phases, calculated for a depth of 520 km by tracing ray paths, using the IASP91 velocity model in figure 34A and 34B, respectively. It is important to note that the piercing points were distributed over a broader region due to the special ray geometry of the converted waves. Thus, they are located far away from the respective station.

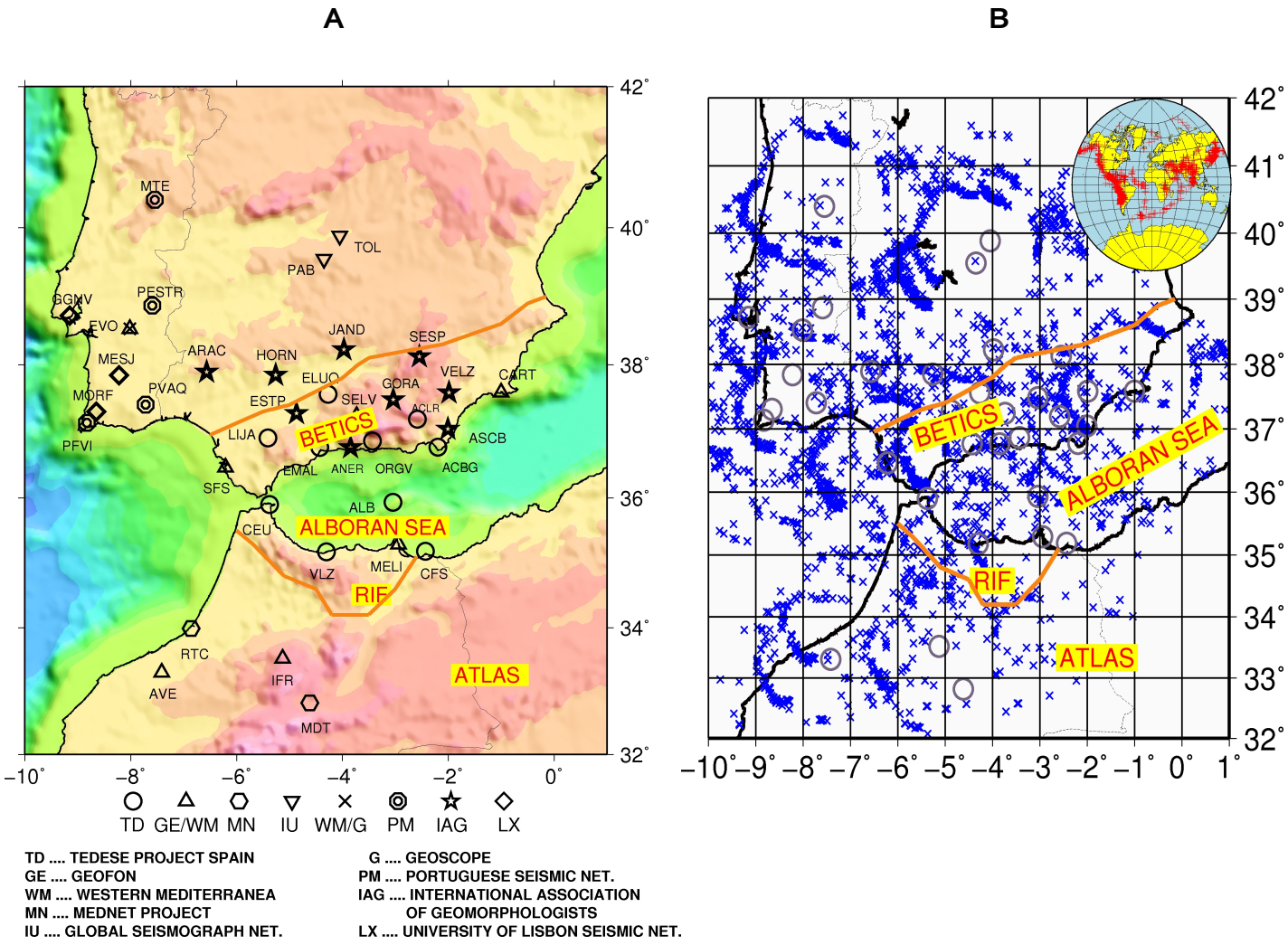

Figure 34: (A) Distribution of stations used in the receiver function analysis.

(B) The distributions of converted P wave ray piercing points at 520 km.

6.4 Data examples

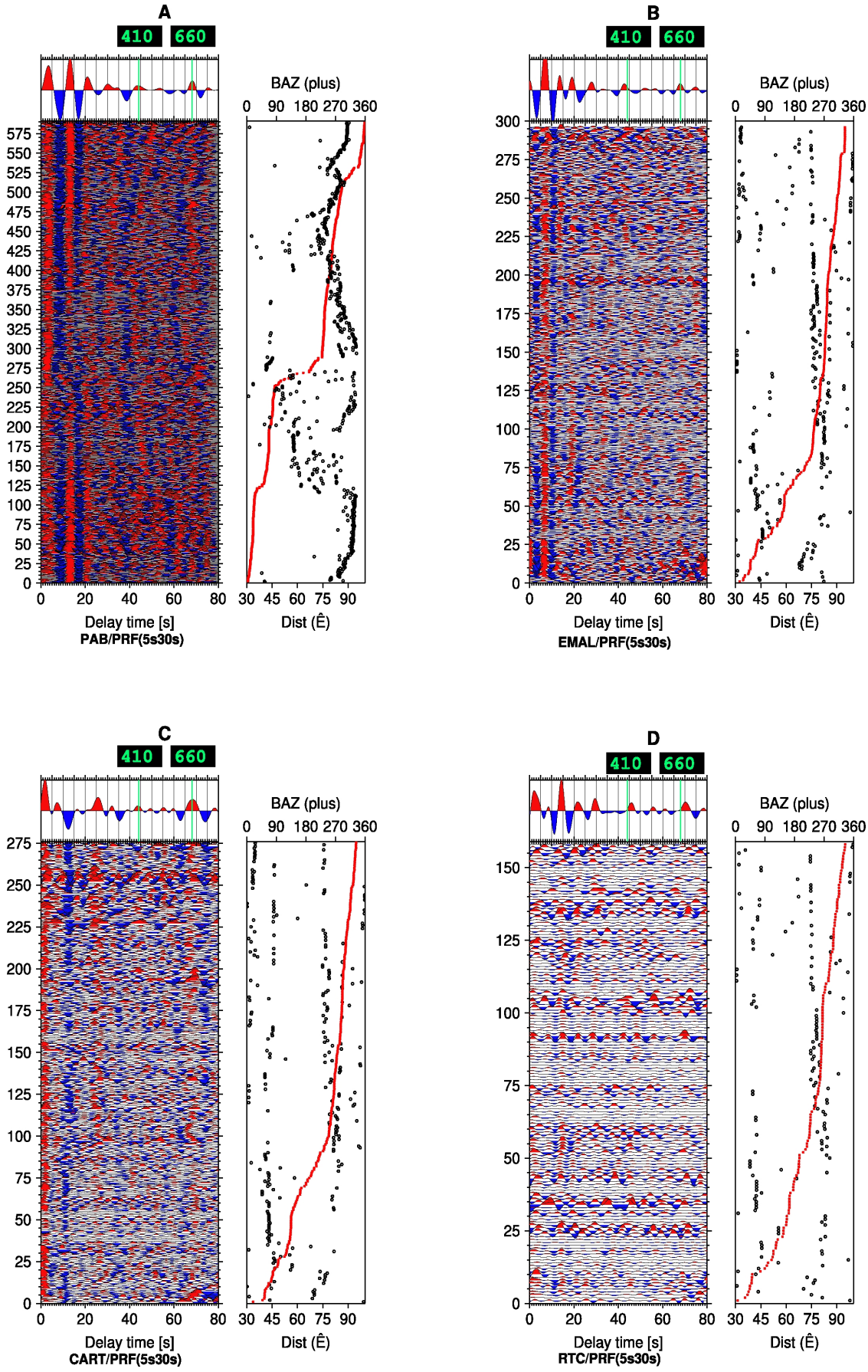

Figure 35: Individual and stacked PRFs observed at stations PAB **(A)**, EMAL **(B)**, CART **(C)**, and RTC **(D)**. They are band-pass filtered with a band-pass from 5-30s. The predicted arrival times from the 410 and 660 km discontinuities, according to the IASP91, are indicated by green lines.

We present here four data examples in figure 35, in which the individual PRFs, displaying the first 80s of the summation traces, are represented from single stations. figure 35A-D show the PRFs from the stations PAB, EMAL, CART, and RTC, respectively. The individual traces, sorted according to the epicentral distances, were moveout corrected before stacking. The trace at the top of each figure represents the stack of all individual traces. At these stations, the 410 and 660 phases are clearly visible. Green lines labeled 410 and 660 indicate the delay times of 48.1 and 68.0s for the discontinuities at 410 and 660 km depths, respectively, based upon the IASP91.

6.5 Subdividing the area under investigation in different sub-regions

After calculating the piercing points of the PRFs for a depth of 520 km, similarly to the SRFs analysis, we also considered a cross-section whose geographical orientation occurs in an imaginary plane which runs parallel to the strike of the Betics (see Box2-9). In order to investigate the regional variations of the topography of the MTZ discontinuities underlying the area of study, the target area was then subdivided into the four geographic sub-regions, shown in figure 36A:

1) The western Iberia (Box10-11 in magenta color))

2) The middle Iberia (Box5-9 in cyan color)

3) The Alboran Sea (Box2-3 in red)

4) The Atlantic-Africa regions (Box1 in blue) and the Betics (Box4 in blue).

To study the MTZ discontinuities in the region of the deep events occurring beneath southernmost Spain, we also defined piercing point boxes with width and length dimensions of 200X 200 km (figure 36B). In figure 36C, we plotted the stacked PRFs within the corresponding geographical sections for a sequence of their frequency bands: a bandpass from 1-30s (B), a bandpass from 3-30s(C), and a bandpass from 5-30s (D). To enable a visual comparison of the arrivals from the MTZ, we also marked the theoretical arrivals according to the IASP91 global reference model with straight green lines.

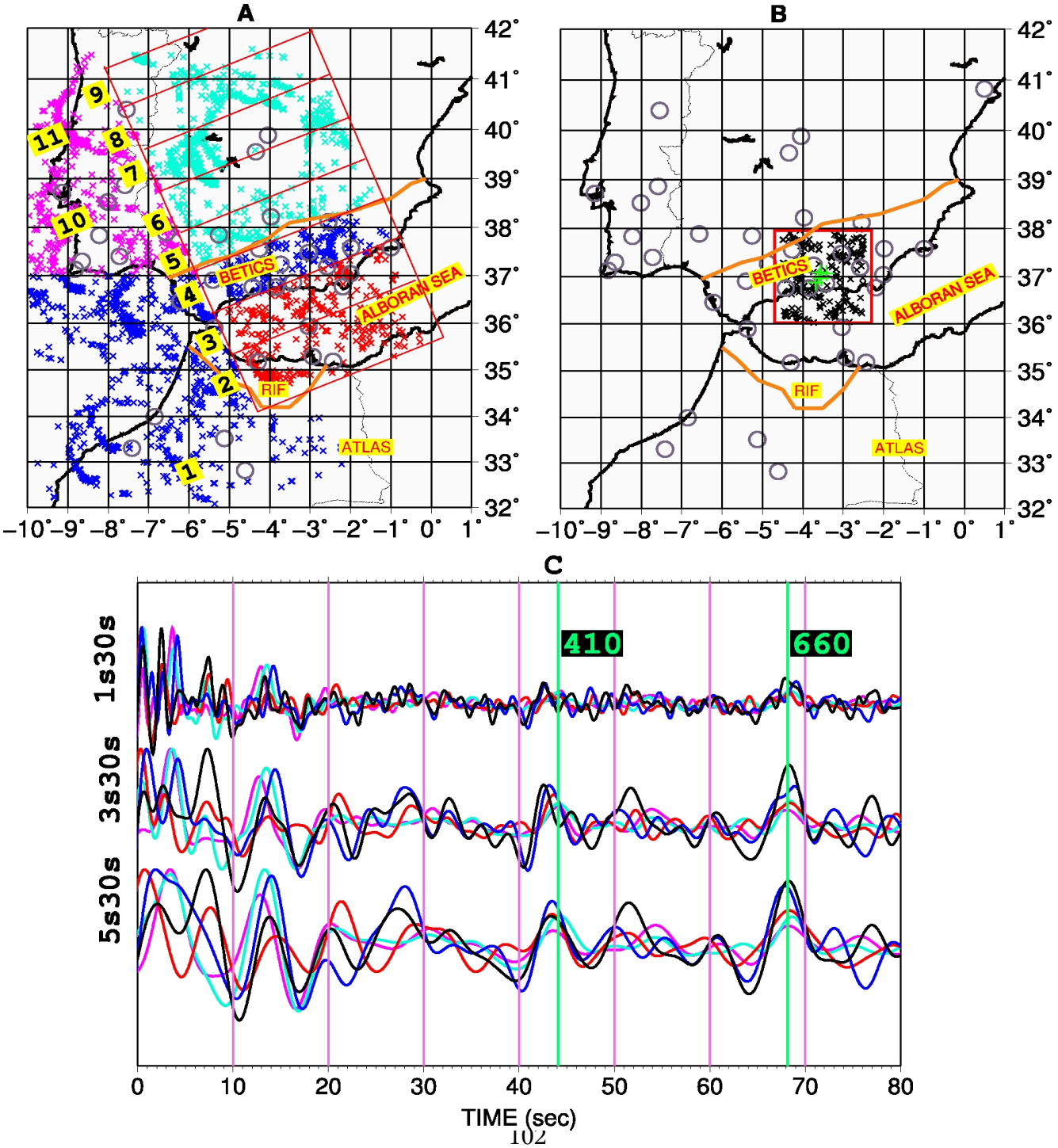

Figure 36: (A) Piercing point distribution of the PRFs, calculated for a depth at 520 km along with division of the area under investigation into four sub-regions in different colors. **(B)** Outlining of the region characterized by some deep events beneath the southernmost region Spain. Green crosses indicate epicenters of the five deep-focus earthquakes. In contrast, black crosses denote piercing-point distributions of the PRFs, calculated at a depth of 520 km. **(C)** Resulting traces corresponding to the each sub-region for different band-pass filters (same colors as piercing points). Amplitudes of waveforms are normalized. P-to-S conversions from the 410 km and 660 km discontinuities are well observed for each sub-region in the entire frequency band. The green lines indicate the expected Ps delay times for P410s and P660s in respect to IASP91. All measured 410 and 660 conversion times are close to IASP91. The results indicate that the topography of the 410 and 660 km discontinuities do not appear to be influenced by any thermal structures potentially associated with subduction or plumes.

By comparing the arrivals from the 410 and 660 with the global average value, one is able to estimate the variation of the thickness of the MTZ as well as the temperature variation in the ambient mantle. From the stacked PRFs waveforms, we clearly observe two positive signals from the two major upper mantle transition discontinuities at depths of 410 and 660 km around 43.8 and 68.1s which correlate very well with the average global value according to the IASP91 reference model. In summary, it can be concluded that the 410 and 660 km discontinuities do not appear to be perturbed by cold or warm material. This situation is also suggesting that the crustal and lithospheric dynamic processes dominating beneath the target area are restricted to depths shallower than 400 km.

To illustrate the consistency of the converted phases on PRFs, we also display the individual and stacked PRFs obtained for two sub-regions containing Alboran Sea basin (Box2-3) (figure 37A) and the middle Iberia (figure 38A). Similarly, we created PRFs, using for a sequence of three different frequency bandpass filter (figure 37B, C, D and figure 38B, C, D). For each region, two strong signals with arrival times of about 44± 0.5s and 67.7± 0.5s after the direct P phases are visible, which can be identified as the converted Ps signals from the 410 and 660 km discontinuities. To compare, we also displayed the theoretical arrival times of these phases corresponding to IASP91 velocity model at 67° (or 6.4 s/deg-slowness), which are denoted by thin green lines at the 44.1 and 68.0s. To sum up, the 410 and 660 km discontinuities are generally found at their expected depth, implying that mantle temperatures in the region are close to the global average. In addition to that, there is also visible a mid transition zone velocities at 520 km for the northern part of the Iberia.

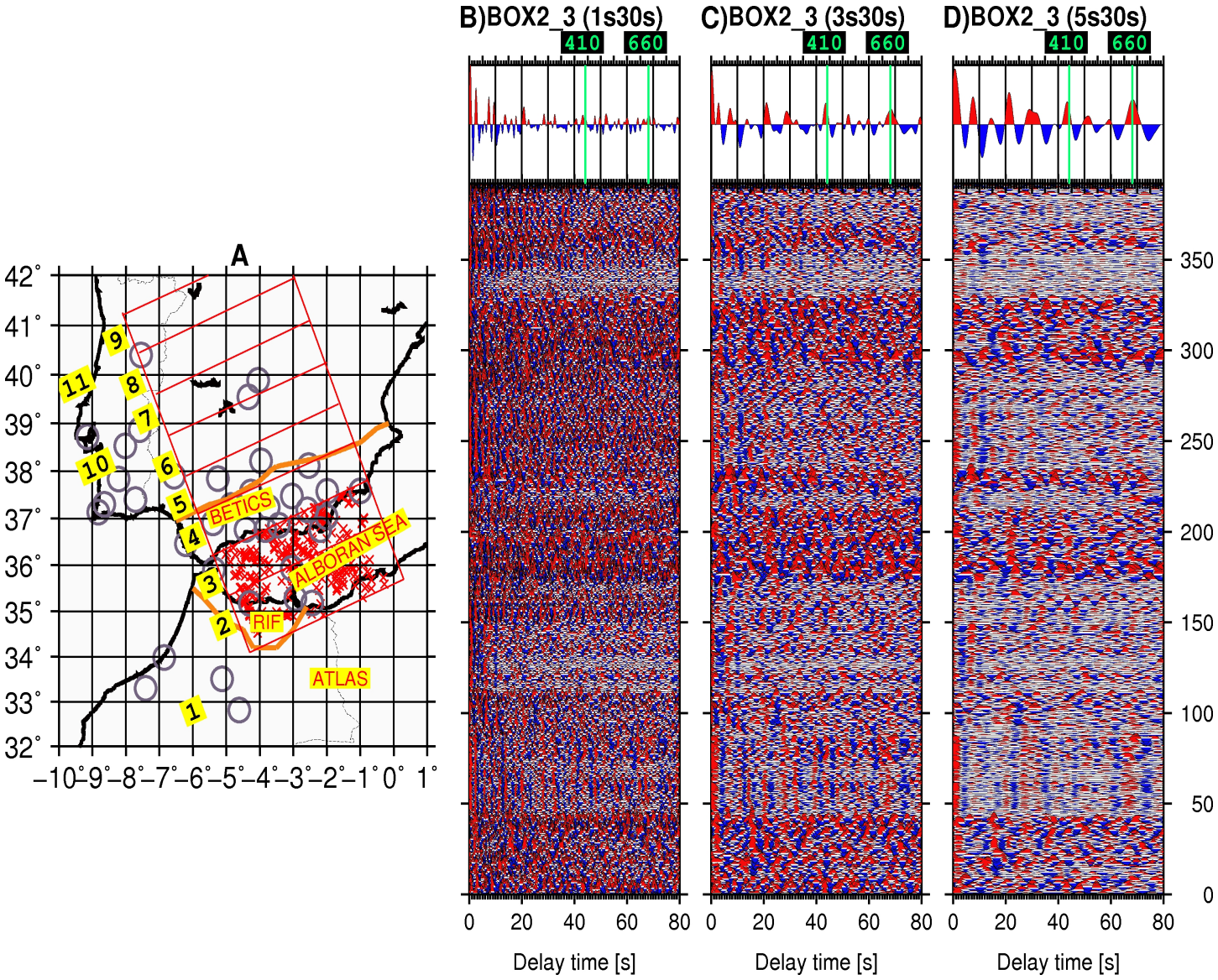

Figure 37: (A) Distributions of piercing points of PRFs as calculated for the Alboran Sea (Box2_3) at a depth of 520 km. **(B, C, D)** Individual and stacked PRFs generated for this sub-region by applying three different bandpass filters. The 410 and 660 can be easily observed in the frequency of all the band. The green lines indicate the expected Ps delay times for 410 and 660 in respect to the IASP91 reference velocity model. In general, the 410 and 660 km discontinuities do not show any significant depth deviation from their expected values. In this region, we observe no clear evidence in a deflection of the MTZ discontinuities as should be expected in presence of any slab or plume in the area of study.

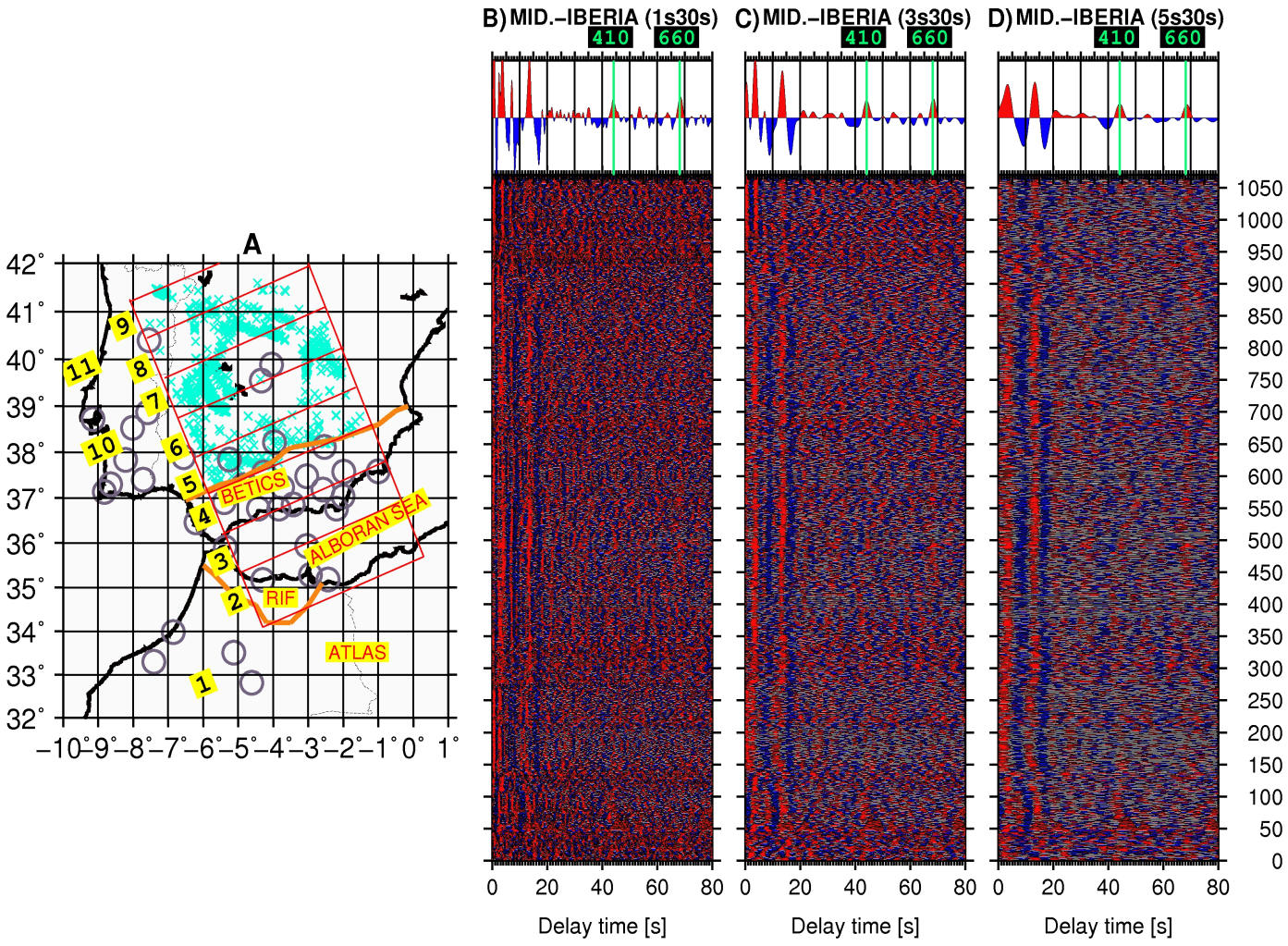

Figure 38: (A) Distributions of piercing points of PRFs as calculated for the northern Iberia for a depth of 520 km. **(B, C, D)** Individual and stacked PRFs generated for this sub-region by applying of three different bandpass filters. The 410 and 660 can be easily observed in the frequency of all the band. The green lines indicate the expected Ps delay times for 410 and 660 in respect to the IASP91 reference velocity model. In general, the 410 and 660 km discontinuities do not show any significant depth deviation from their expected values. In this region, we also observe no clear evidence in a deflection of the MTZ discontinuities owing to any slab or plumes.

Chapter 7

Results and conclusions

7.1 Introduction

In this study, we presented results obtained from PRFs and SRFs analysis conducted for data recorded at thirty-seven seismological stations from nine networks in the westernmost Mediterranean Sea region and the surroundings. To image the crustal, sub-crustal lithospheric and upper mantle transition zone discontinuities at depths of 410 and 660 km, we generated 5,500 PRFs of high signal-to-noise ratio, which were calculated for teleseismic events from a epicentral distance range between 30° to 95°. In contrast, we also exploited SRFs to determine the lateral variation of the lithospheric thickness beneath the area of interest. Overall, PRFs and SRFs analysis techniques have proven to be useful tools in investigating the laterale depth variation of such subsurface discontinuities in a tectonically highly complex region.

In what follows, we would like firstly to present the most significant key findings from our survey. Also, we shall propose a geodynamic model for the tectonic evolution of the area of study.

7.2 Results derived from PRFs

We have successfully estimated the crustal thickness variations along the area investigated, using PRFs calculated for thirty-seven sites. The following conclusions can be made:

- The Moho discontinuities are clearly detected across the area of study.
- PRFs exhibit significant variations in crustal thickness along the area of investigation.
- The crust is the thinnest in the central part of the Alboran Sea.

- One of the fundamental observations is that the thickness of the crust along the Alboran domain is the greatest in the west and reveals a systematic decrease towards the east (ranging between 16.0 and 40.0 km).

- We find the thickest crust in the Gibraltar arc region beneath the stations (CEU and SFS, 40 km). The thinnest crust (16 km) lies beneath the Central Alboran Sea (ALB, 16 km).

- The southern-east part of the Internal Betics (CART, ACLR, ACBG, 18 km) and northern Morocco (MELI, CFS, 20 km) has a relatively thicker continental crust.

By geographically subdividing the target area, we also investigated the upper mantle structure below the same area in order to examine the influence (interaction) of possible subduction- or delamination-related processes acting in the deep interior with 410 and 660 km discontinuities.

Based upon the PRFs analysis, the most important results and conclusions of this study in terms of the upper mantle structure are as follows:

- The 410 and 660 km discontinuities are clearly detected.

- Arrivals from the 410 and 660 km discontinuities do not show any significant difference in terms of delay times from their ordinary values according to the IASP91 global reference model. This implies that mantle temperatures in the region are close to the global average (see figure 36).

- Our observations do not provide conclusive evidence for subduction- or delamination-related processes in the composition of the upper mantle transition zone beneath the target area. The deep earthquakes in this region can, therefore, not be related to a general subduction.

7.3 Results derived from SRFs

For the depth range of LAB, PRFs analysis might lead to misinterpretation of seismic discontinuities, due to multiple signals within the crust. However, SRFs are not falsified with

multiples, because of their precursor character, and therefore provide more reliable patterns in characterizing LAB. Using S and SKS body waves, the lateral variation in depths of the lithospheric discontinuity along the target area has been successfully constrained on a high-resolution. The most important conclusions to be drawn from the observations of SRFs in this work are that:

- We generally obtained a rapid lateral variation in lithospheric thickness beneath the target area.

- We observed a strong lithospheric contrast between the Alboran Sea region, the northern Betics and the remaining fields in the subject area. In the cross-section transecting the Alboran Sea and the Betics (figure 29), the shallowest portions of LAB range between 60 and 90 km (in the Alboran Sea: grids 2-3 and along the Northern Betics: grids 6-9), while the LAB depths are typically between 90 and 100 km along the profile (African plate: grid 1; the Betics: grids 4-5; southern Portugal: grids 10-11). Thus, the lithosphere beneath the central part of the Alboran basin has a depth of 60 km, indicating the thinnest lithosphere in the subject area. A north directed deepening of the LAB beneath the Betics was also observed (figure 29; grids 3-5).

- An east-west oriented cross-section running parallel to the Alboran Sea indicated that the LAB is the deepest in the westernmost part of the region (Atlantic: down to 90 km) and systematically shallows across the Alboran Sea towards the east, reaching up to 60 km (see figure 30).

- By performing a profile along the strike of the Betics, we found that there are no significant changes of LAB signals, as they remain at similar delay times around 10s (see figure 31).

Spatial distribution of the LAB depths along the region is simplified as a sketch in figure 39, separating the regions' shallow and deep depths. In the north, a large portion of Iberian Peninsula accommodates relatively shallow LAB. However, the LAB depths get prominently deeper in south-western Portugal, Gibraltar, and the westernmost part of the Atlantic, the Betics and northern Africa. The LAB depths are shallow also along the Alboran Sea. Here, the coastlines represent a structural boundary between shallow and deep LAB depths.

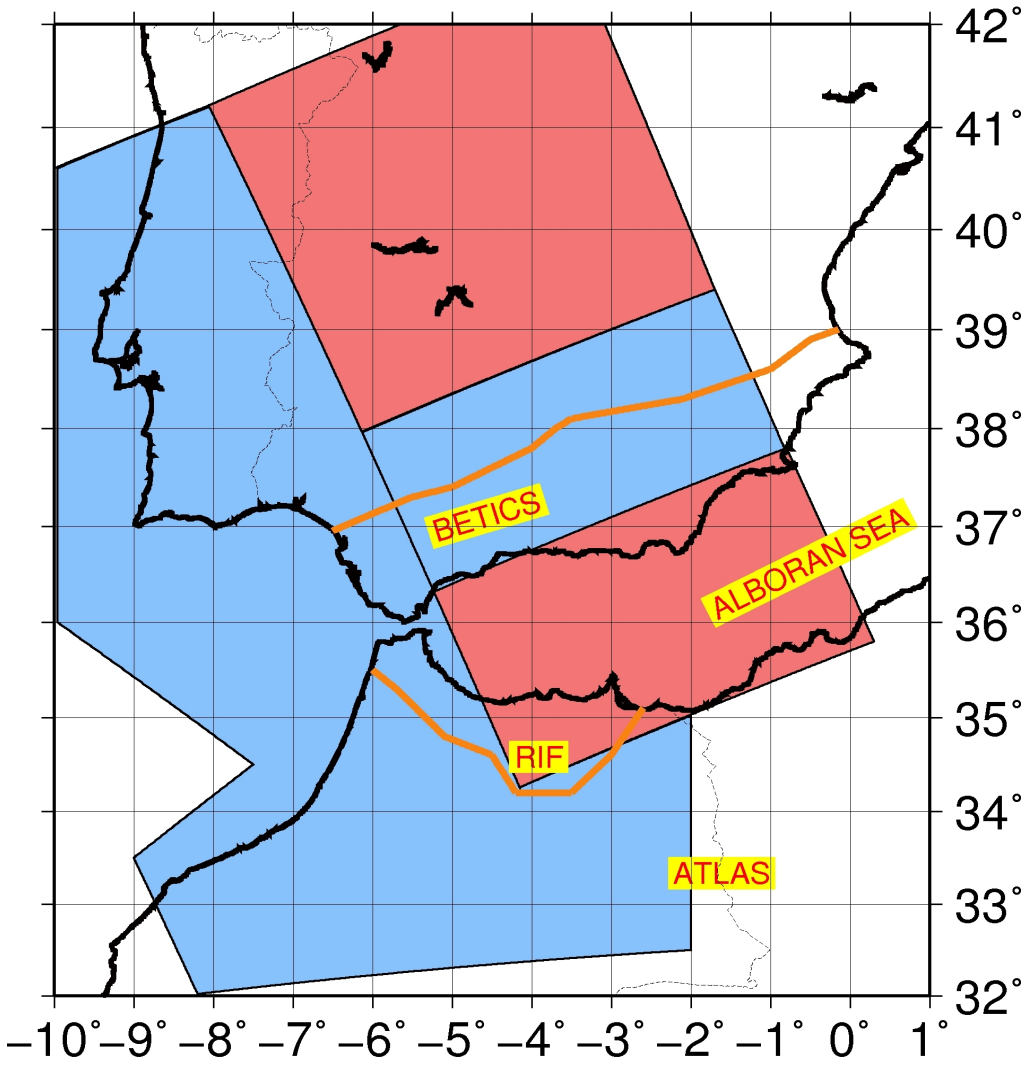

Figure 39: Distribution of LAB depth in the area of study as inferred from a cross-section running perpendicular to the strike of the Betics. Blue area = 90-100 km depth, red-area = 60–90 km depth. The Alboran Sea region and some part of central Iberia possess a shallow LAB, whilst north-west Africa, the Gibraltar region and south-west Portugal have a clearly thicker lithosphere.

7.4 Discussion

We have found a shallow LAB (60-90 km) beneath the northern part of the Betics. This confirms the result obtained from the analysis of surface waves, suggesting a low velocity zone below 80 km along the entire region north of the Betics (Martinez et al. 2005). On the other hand, more recently, Ayarza et al. 2010 have observed a signal at a depth of 60-70 in south west Iberia, processing the wide-angle reflection data. They have modeled this signal with a velocity increase, relating it to the Hales discontinuity. In most cases, however, it is

difficult to know, if a high frequency wide reflection from the upper mantle is generated by a velocity increase or decrease. It depends strongly on the identification of the sign of the reflected signal. Such a reflection should have a positive (negative) sign in case of a velocity increase (decrease). But, Ayarza et al. (2010) have not provided clear evidence that their mantle reflection has a positive sign. In our view, a negative sign is also equally possible. For this case, their result would agree very well with our observations, namely that the wide angle reflection could have been generated by the LAB instead of the Hales discontinuity (which is usually assumed to be positive). In general, SRFs have no problem with the sign of the converted signals due to their long period character. Additionally, Gutierrez-Alonso et al. (2011) and Ducea (2011) put forward a model suggesting large scale delamination below the Iberian Massif. This model is consistent with our observation of a thin lithosphere north of the Betics.

The Alboran Sea has also a shallow LAB which is at its shallowest at its eastern part. Seber et al. (1996) and Houseman (1996) suggested the delamination model for the Alboran Sea, which is directly associated to crustal and lithospheric thinning. In conclusion, according to our results, the northern part of the Betics and Alboran Sea are mainly characterized by lithosphere thinning, being subjected to the delamination process.

According to our results, southern Portugal, Gibraltar, the westernmost part of the Atlantic, the Betic and North Africa indicate a deeper LAB than the Alboran Sea and the Iberian Massif. However, we were not able to find any conclusive evidence for both an easterly-directed subduction from Gibraltar (e.g., Gutscher 2002) and a southerly-directed subduction below the Betics (e.g., Morales et al. 1999), beneath the studied area, as suggested by tomography.

7.5 Conclusions

Our SRFs observations do not show a clear indication for a large subduction zone unless it is near vertical. Furthermore, our PRFs observations related to the structure in the upper mantle at 410 and 660 km do not provide any indications of disturbances due to down-moving cold or upwelling mantel materials. This supports the idea that a collisional regime between the African and Eurasian plates in the western edge of the Mediterranean Sea is

confined within a shallower part of the upper mantle and does not influence the mantle transition zone.

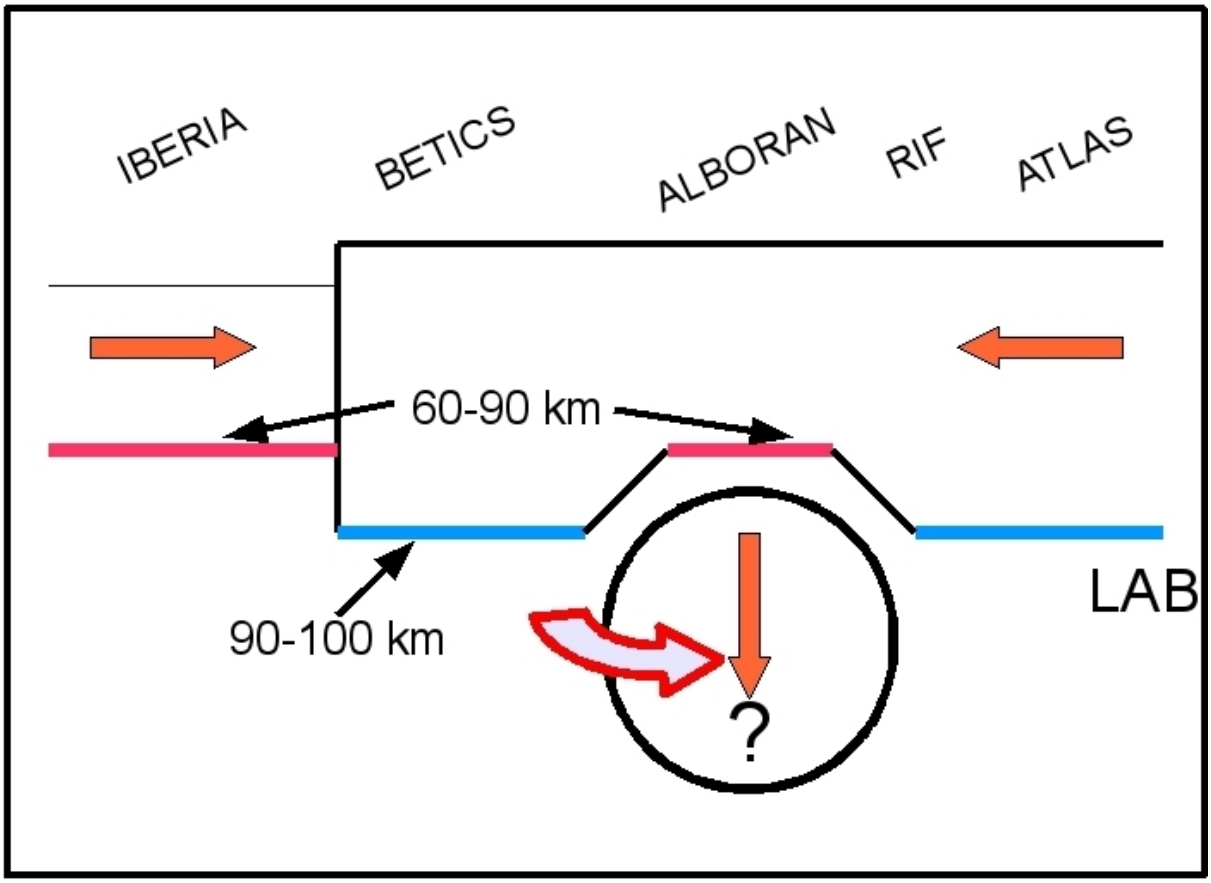

Figure 40: Sketch for the interpretation of the observations. Combined results from PRFs and SRFs suggest that the lower part of a previously thickened lithosphere beneath the Rif Mountains and the adjacent Alboran Sea due to the collision of Iberian and African plates has been delaminated into the upper mantle. Most lithospheric material is removed in the eastern Alboran Sea. Gibraltar and the neighbouring Atlantic appear to remain unaffected by this delamination. The rotational arrow indicates a hypothetical explanation for mantle anisotropy observations in the area.

We interpret our results to support the model developed based on delamination of the deep roots of Betics-Rif collusion orogen (Platt and Vissers 1989, Houseman 1996, Calvert et al. 2000). As indicated before, Buontempo et al. (2008) suggested fast polarization directions obtained from SKS analysis aligned parallel to the coastlines of Alboran Sea, which is in agreement with the subduction rollback model. If we combine the results of both of those studies, it might be claimed that a near vertical delaminating body might eventually get a

rotational component in a complicated mantle structure (figure 40). The earthquakes with very-deep focal depths are probably due to relatively small amounts of materials moving downward rather than to a general subducting slab.

Literature

Al–Amri, A. M. S. (1998), The crustal structure of the western Arabian platform from the spectral analysis of long–period P–wave amplitude ratios. Tectonophysics 290, 271–283.

Anderson, D.L. (1967), Latest information from seismic observations. In: T.F. Gaskell (Ed.), The Earth's Mantle.Academic Press, New York, pp. 355–420.

Ammon, C. J. (1991), The isolation of receiver effects from teleseismic P waveforms, Bull. Seismol. Soc. Am., 81, 2504-2510.

Ammon, C. J., and Zandt G. (1993), The receiver structure beneath the southern Mojave Block, Bull. Seism. Soc. Am., 83, 737-755.

Anderson, D. L., and Toksöz, M. N. (1963), Surface Waves on a Spherical Earth 1. Upper Mantle Structure from Love Waves, J. Geophys. Res., 68(11), 3483–3500.

Anderson, D.L. and Bass, J.D. (1986), Transition region of the Earth's upper mantle, Nature, 320, 321–328.

Andrieux, J., Fontbote and Mattauer, M. (1971), Bull. Soc. géol. Fr. 27, 115-118.

Ayarza, P., Palomeras, I., Carbonell, R., Afonso, J.C., Simancas, F. (2010), A wide-angle upper mantle reflector in SW Iberia: Some constraints on its nature. Physics of the Earth and Planetary Interiors, 181, 88-102.

Badal, J., Corchete, V., Payo, G., Serón, F. J., Canas, J. A. and Pujades, L. (1992), Deep structure of the Iberian Peninsula determined by Rayleigh wave velocity inver- sion, Geophys. J. Int., 108, 71-88.

Bakun, W. H. (1971), Crustal model parameter from P–wave spectra. Bull. Seism. Soc. Am. 61, 913–935.

Banda, E., and Ansorge, J. (1980), Crustal structure under the central and eastern part of the Betic Cordillera. Geophys. J. R. Astron. Soc., 63:515-532.

Banda, E., Suriñach E., Aparicio A., Sierra J. and Ruiz de la Parte E. (1981), Crust and upper mantle structure of the central Iberian Meseta (Spain), Geophys. J. R. Astron. Soc. 67, pp. 779–789.

Banda, E., Udias, S., Müller, S., Mezcua, J., Boloix, M., Gallart, J. and Aparicio, A. (1983), Crustal structure beneath Spain from deep sounding experiments, Phys. Earth Planet. Inter., 31, 277-280.

Banda, E., Gallart, J., García-Dueñas, V., Danobeitia, J., and Makris, J. (1993), Lateral variation of the crust in the Iberia Peninsula: new evidence for the Betic Cordillera. Tectonophysics, 221:53-66.

Barrel, J. (1914), The strength of the Earth's crust, Geology, 22, 28-44.

Bijwaard, H., Sparkman, W. (2000), Nonlinear global P-wave tomography by iterated linearized inversion. Geophysical Journal International 141, 71– 82.

Bina, C.R. (1991), Mantle discontinuities, U.S. Natl. Rep. Int. Union Geodes. Geophys. 1987–1990, Rev. Geophys., 29, 783–793.

Bina, C., Helffrich, G.R. (1994), Phase transition Clapeyron slopes and transition zone seismic discontinuity topography. J. Geophys Res. 99, 15853–15860.

Blanco M. J. and Spakman W. (1993), The P-wave velocity structure of the mantle below the Iberian Peninsula: evidence for subducted lithosphere below southern Spain. Tectonophysics, 221:13-34.

Booth-Rea, G., Ranero C.R., Martinez-Martinez J.M., Grevemeyer I. (2007), Crustal types and Tertiary tectonic evolution of the Alboran sea, western Mediterranean. Geochem Geophys Geosyst., 8(10), 1–25.

Bortolotti, V. and Principi, G. (2005), Tethyan ophiolites and Pangea break-up, Island Arc 14, pp. 442–470

Buforn, E., Coca, P., Udias, A. and Lasa, C. (1997), Source mechanism of intermediate and deep earthquakes in southern Spain. J. Seismol., 1, 113–130.

Buontempo L, GHR Bokelmann, G Barruol and J Morales (2008), Seismic anisotropy beneath southern Iberia from SKS splitting. Earth Planet. Sci. Lett. 273, 237-250.

Byerly, P. (1926), The Montana earthquake of. June 28, 1925, G.M.C.T.: Seismol. Soc. America Bull., 16, 209-265.

Calvert, A., Sandvol, E., Seber, D., Barazangi, M., Roecker, S., Mourabit, T., Vida, F., Alguacil, G., Jabour, N. (2000), Geodynamic evolution of the lithosphere and upper mantle beneath the Alboran region of the western Mediterranean: Constraints from travel time tomography, J. Geophys. Res., 105, 10871-10898.

Castle, J.C. and Creager, K.C. (1998), Topography of the 660-km seismic discontinuity beneath Izu-Bonin: Implications for tectonic history and slab deformation, J. geophys. Res., 103, 12 511–12 527.

Cavendish, H. (1798), Experiments to determine the density of Earth. Philosophical Transactions of the Royal Society of London, 88: p. 469-479.

Chen, L., Zheng, T., Xu, W. (2006), A thinned lithospheric image of the Tanlu Fault Zone,eastern China constructed from wave equation based receiver function migration. Journal of Geophysical Research 111, B09312. doi:10.1029/2005JB003974.

Chevrot, S., Vinnik, L. and Montagner, J.-P. (1999), Global-scale analysis of the mantle Pds phases, J. geophys. Res., 104, 20 203–20 219.

Collier, J. D., and G. R. Helffrich (1997), Topography of the “410” and “660” km seismic discontinuities in the Izu-Bonin subduction zone, Geophys. Res. Lett., 24, 1535– 1538.

Collier, J. D., and G. R. Helffrich (2001), The thermal influence of the subducting slab beneath South America from 410 and 660 km discontinuity observations, Geophys. J. Int., 147, 319– 329

Comas, M.C. and Jurado, M.J. (1990), The sedimentary record of the. Iberian Alboran Margin. In: Global events and Neogene evolution of the. Mediterranean. IX Congress Regional Committee on Mediterranean. Neogene Stratigraphy. 105.

Comas, M.C., Garcia-Duenas, C. V. and Jurado, M. J. (1992), Neogene tectonic evolution of the Alboran Sea from MCS data Geo-Mar. Lett. 12, 157-164 .

Comas, M.C., Platt, J.P., Soto, J.I, Watts, A.B. (1999). The origin and tectonic history of the Alboran Basin: insights from Leg 161 results. In: Zahn, R., Comas, M.C., Klaus, A. (Eds.), Proc. ODP, Sci. Results, vol. 161. Ocean Drilling Program, College Station, TX, pp. 555–580.

Comas, M.C., Dañobeitia, J.J., Alvarez-Marrón, J., and Soto, J.I. (1997), Crustal reflections and structure in the Alboran Basin: preliminary results of the ESCI-Alboran Survey. Rev. Soc. Geol. Esp., 8, 76-88.

Dallmeyer, R.D. and Martínez-Garcia, E. (1990), Pre-Mesozoic geology of Iberia, Springer Verlag.

DeMets, C., Gordon, R.G., Argus, D.F., and Stein, S. (1990), Current plate motions: Geophysical Journal International, 101, 425-478.

DeMets, C., Gordon, R.G., Argus, F., Stein, S. (1994), Effect of recent revisions of the geomagnetic timescale on estimates of current plate motions. Geophys. Res. Lett. 21, 2191–2194.

Demnati, A. (1972), Krustenstruktur im Rif-Bereich von nord-Morocco aus gravimetrischen und aeromagnetischen regionalmessungen, Bull. Geofis. Theo. Appl., 14, 203-236.

De Smet M.E.M (1984), Wrenching in the External Zone of the Betic Cordilleras, southern Spain, Tectonophysics, 107 , 57–79.

Dewey J.F., Pitman W.C. III, Ryan W.F.R. and Bonnin J. (1973), Plate tectonics and the evolution of the Alpine system, Geol. Soc. Am. Bull. 84, 3137–3180.

Dewey J.F., Helman M.L., Turco E., Hutton D.H.W. and Knott S.D. (1889), Kinematics of the western Mediterranean, Alpine Tectonics. In: M.P. Coward, D. Dietrich and R.G. Park, Editors, Geol. Soc. London, Spec. Publ., 45 , 265–283.

Díaz, J., Gallart, J. (2009), Crustal structure beneath the Iberian Peninsula and surrounding waters: A new compilation of deep seismic sounding results, Phys. Earth Planet. Int. 173, 181-190.

Diaz, J., Gallart, J., Villasenor, A., Mancilla, F., Pazos, A., Cordoba, D., Pulgar, J. A., Ibarra, P., and Harnafi, M. (2010), Mantle dynamics beneath the Gibraltar Arc (western Mediterranean) from shear-wave splitting measurements on a dense seismic array, Geophys. Res. Lett. 37, L18304, doi: 10.1029/2010GL044201.

Dillon, W.P., Robb, J.M., Greene, H.G. and Lucena, J.C. (1980), Evolution of the continental margin of southern Spain and the Alboran Sea. Marine Geology, 36, 205-226.

Docherty, C. and Banda, E. (1995), Evidence for the eastward migration of the Alboran Sea based on regional subsidence analysis: A case for basin formation by delamination of the subcrustal lithosphere?, Tectonics 14, 804-818.

Ducea M. H. (2011), Fingerprinting orogenic delamination, Geology 39, 191-192.

Dueker, K. G., and Sheehan A. F. (1997), Mantle discontinuity structure from midpoint stacks of converted P to S waves across the Yellowstone hotspot track, J. Geophys. Res., 102, 8313– 8327.

Durand, B., Jolivet, L., Horvath, F. and Seranne, M. (1999), The Mediterranean Basins: Tertiary Extension within the Alpine Orogen, Geological Society London Special Publication no. 156.

Ekström, G. and Dziewonski A.M. (1998), The unique. anisotropy of the Pacific upper mantle, Nature, 394,. 168–172.

Faber, S. and Mueller, G. (1984), Converted phases from the mantle transition zone observed at European stations, J. Geophys., 54: 183194.

Faccenna et al. (2004), Lateral slab deformation and the origin of the western Mediterranean arcs. Tectonics, 23, 1012-1033.

Fadil A., Vernant P., McClusky S., Reilinger R., Gomez F., Ben Sari D., Mourabit T., Feigl K. and Barazangi M. (2006), Active tectonics of the Western Mediterranean: GPS evidence for roll back of a delaminated subcontinental slab beneath the Rif Mountains, Morocco. Geology 34, 529–532, doi:10.1130/G22291.1.

Farra, V., Vinnik, L. (2000). Upper mantle stratification by P and S receiver functions. Geophys. J. Int. 141, 699–712.

Fee, D., and Dueker, K. (2004), Mantle transition zone topography and structure beneath the Yellowstone hotspot: Geophysical Research Letters, v. 31, doi: 10.1029/2004GL020636.

Fischer, K. M., Ford, H. A., DL Abt, D. L., and Rychert, C. A. (2010), The Lithosphere-Asthenosphere Boundary. Annual Review of Earth and Planetary Sciences 38, 551-575, DOI:10.1146/annurev-earth-040809-152438.

Flanagan, M.F. and Shearer, P.M. (1998), Global mapping of topography on transition zone velocity discontinuities by stacking SS precursors, J. Geophys. Res., 103, 2673–2692.

Frederiksen, A.W. and Bostock, M.G. (1999), Modelling teleseismic waves in dipping anisotropic structures, Geophys. J. Int., 141, 401–412.

Fullea, J., Fernandez, M. and Zeyen, H. (2006), Lithospheric structure in the Atlantic-Mediterranean transition zone (southern Spain, northern Morocco): a simple approach from regional elevation and geoid data, C. R. Geosci., 338, 140–151.

Fullea J., Afonso, J.C., Fernàndez M., Vergés J. (2010), The structure and evolution of the lithosphere - asthenosphere boundary beneath the Trans-Mediterranean region" Lithos, 120, 1-2, 74-95.

Galindo-Zaldívar, J., Jabaloy, A., González-Lodeiro, F., and Aldaya, F. (1997), Crustal structure of the central sector of the Betic Cordillera (SE Spain). Tectonics, 16, 18-37.

Garcia-Duenas, V., Balanya, J. C. and Martinez-Martinez J. M. (1992), Miocene extensional detachments in the outcropping basement of the northern Alboran Basin (Betics) and their tectonic implications Geo-Mar. Lett. 12, 88-95.

Gilbert, H. J., A. F. Sheehan, D. A. Weins, K. Dueker, L. Dorman, J. Hildebrand, and S. Webb (2001), Upper mantle discontinuity structure in the region of the Tonga subduction zone, Geophys. Res. Lett., 28, 1855–1858.

Gilbert, H. J., A. F. Sheehan, K. G. Dueker, and P. Molnar (2003), Receiver functions in the western United States, with implications for upper mantle structure and dynamics, J. Geophys. Res., 108(B5), 2229, doi:10.1029/2001JB001194.

Gomez F., Allmendinger, R., Barazangi, M., Er-Raji, A. and Dahmani, M. (1998), Crustal shortening and vertical strain partitioning in the Middle Atlas Mountains of Morocco. Tectonics 17, 520–533

Gomez, F., Barazangi, M., and Beauchamp, W. (2000), Role of the Atlas Mountains (northwest Africa) within the African-Eurasian plate boundary zone, Geology, 28, 775-778

Gossler, J. and Kind, R. (1996), Seismic evidence for very deep roots of continents, Earth Planet. Sci. Lett., 138, 1–13.

Grunewald, S., Kind, R. and Weber, M. (2001), The upper mantle under Central Europe - indications for the Eifel plume. Geophys. J. Int., 147, 590-601.

Gu, Y., Dziewo´nski, A.M. and Agee, C.B. (1998), Global de-correlation of the topography of transition zone discontinuities, Earth Planet. Sci. Lett., 157, 57–67.

Gurrola, H. and Minster, J.B. (1998), Thickness estimates of the upper-mantle transition zone from bootstrapped velocity spectrum stacks of receiver functions, Geophys. J. Int., 133, 31–43.

Gurrola, H., Baker, G.E. and Minster, J.B. (1995), Simultaneous time domain deconvolution with application to the computation of receiver functions, Geophys. J. Int., 120, 537–543.

Gutenberg, B. (1914). Über Erdbebenwellen VII. A. (1914), Beobachtungen an Registrierungen von Fernbeben in Göttingen und Folgerungen über die Konstitution des Erdkörpers. Nachrichten K. Gesell. Wiss., Göttingen, Math.-Phys. Klasse, 166-218.

Gutenberg, B. and Richter, C.F. (1938), P' and the Earth's core. Mon. Not. R. Astr Soc. Geophys. Suppl. 4, 363.

Gutenberg, B. (1948), On the layer of relatively low wave velocity at a depth of about 80 kilometers, Bull. Seismol. Soc. Am., 38, 121-148

Gutenberg, B. (1954), Low velocity layers in the Earth's mantle, Bull., Seismol. Soc. Am., 65, 337-348.

Gutenberg, B. (1959), Physics of the Earth's interior, Academic Press, New York and London, 240pp.

Gutierrez-Alonso, G., Murphy, J.B., Fernández-Suárez, J., Weil, A.B., Franco, M.P., and Gonzalo, J.P. (2011), Lithospheric delamination in the core of Pangea: Sm-Nd insights from the Iberian mantle: Geology, v. 39, p. 155–158.

Gutscher M.-A., Malod, J., Rehault, J.-P., Contrucci, I., Klingelhoefer, L., Mendes-Victor, L. and Spakman, W. (2002), Evidence for active subduction beneath Gibraltar Geology, 30(12), 1071-1074.

Gutscher, M.-A.; Baptista M.A. and Miranda J.M. (2006), The Gibraltar Arc seismogenic zone (part 2): Constraints on a shallow east dipping fault plane source for the 1755 Lisbon earthquake provided by tsunami modeling and seismic intensity. Tectonophysics 426: 153–166. doi:10.1016/j.tecto.2006.02.025.

Horvath F. and Berckhemer H. (1982), Mediterranean Backarc Basins. In H. Berckhemer and K. Hsu,. Alpine-Mediterranean Geodynamics, AGU Geodynamic Series v.7, 141-173.

Hatzfeld, D., y Frogneux, M. (1980), Structure and tectónics of the Alboran Sea area, Evolution and tectonics of the Western Mediterranean and surroundings areas, ed. Inst. Geog. Nacional, Special publication, n. 201, 93-108

WGDSSA (1978), (The Working Group for Deep Seismic Sounding in the Alboran Sea 1974–1975), Crustal seismic profiles in the Alboran Sea: preliminary results, Pageoph., 116, 167–179.

Helffrich, G. (2000), Topography of the transition zone seismic discontinuity. Rev. Geophys. 38, 141–158.

Houseman, G. (1996), From mountains to basin, Nature 379, 771 – 772.

Iribarren, L., Vergés, J., Camurri, F., Fullea, J. and Fernàndez, M. (2007), The structure of the Atlantic–Mediterranean transition zone from the Alboran Sea to the Horseshoe Abyssal Plain (Iberia–Africa plate boundary), Marine Geology 243, 97–119.

Ito, E. and Takahashi, E. (1989), Post-spinel transformations in the system Mg2SiO4-Fe2SiO4 and some geophysical implications. J. Geophys. Res. 94, 10637-10646.

Jeffreys, H. (1939), The times of the core waves, Mon. Notes R. Astron. Soc. Geophys. Suppl, 4, 548–561.

Jeffreys, H. and Bullen, K. E. (1940), Seismological Tables. British Association for the Advancement of science London, 50pp.

Johnson, L. R. (1967), Array measurements of P velocities in the upper mantle: Jour. Geophys. Research, 72, 6309-6325.

Jolivet, D. Frizon De La Motte, A. Mascle and M. Seranne, The Mediterranean Basins: Tertiary extension within the Alpine Orogen — An Introduction. In: B. Durand, L. Jolivet, F. Horvath and M. Séranne, Editors, The Mediterranean Basin: Tertiary Extension within the Alpine Orogen, London Geological Society, Special publications **156** (1999), pp. 1–14.

Jordan T. H. (1979), Sept., 76(9): 4192–4200, "Structural Geology of the Earth's interior", Proceedings of the National Academy of Science.

Kanamori, H. (1967), Upper mantle structure from apparent velocities of P waves recorded at Wakayama Micro-Earthquake Observatory, Bull. Earthq. Res. Znst. Tokyo Univ., 45,657-678.

Kennett, B. L. N., and E. R. Engdahl, Travel times for global earthquake location and phase identification (1991), Geophys. J. Int., 105, 429-465.

Kennett B.L.N., Engdahl E.R. and Buland R. (1995), Constraints on seismic velocities in the Earth from travel times Geophys. J. Int, 122, 108-124

Kind, R. (1978), The reflectivity method for a buried source. J. Geophys. 44, 603-612.

Kumar, P.; Kind, R.; Hanka, W.; Wylegalla, K.; Reigber, Ch.; Yuan, X.; Woelbern, I. (2005), The lithosphere asthenosphere boundary in the North-West Atlantic region, Earth and Planetary Science Letters, Volume 236, 249-257.

Kumar, P., X. Yuan, R. Kind, and J. Ni (2006), Imaging the colliding Indian and Asian lithospheric plates beneath Tibet, J. Geophys. Res., 111, B06308, doi:10.1029/2005JB003930.

Langston, C. A. (1977), Corvallis, Oregon, crustal and upper mantle structure from teleseismic P and S waves, Bull. Seism. Soc. Am. 67, 713–724.

Langston, C. A. (1979), Structure under Mount Rainier, Washington, inferred from teleseismic body waves, J. Geophys. Res. 84, 4749–4762.

Leblanc, D. and Olivier P. (1984), Role of strike-slip faults in the Betic-Rifian orogeny, Tectonophysics, 101 , 345–355.

Leeds, A. R., Knopoff, L. and. Kausel e.g., (1974), Variations of upper mantle structure under the Pacific Ocean. Science 186, 141–143.

Lehmann, I. (1936), P', Publ. Bur. Cent. Sismol. Int. Trav. Sci.,A, 14,. 87-115.

Leong, L. S. (1975), Crustal structure of the Baltic shield beneath Umea, Sweden, from the spectral behavior of long–period P waves. Bull. Seism. Soc. Am. 65, 113–126.

Li, X., Kind, R., Priestley, K., Sobolev, S.V., Tilmann, F., Yuan, X. and Weber, M. (2000(a)), Mapping the Hawaiian plume conduit with converted seismic waves. Nature, 405, 6789, 938-941.

Li, X., S. V. Sobolev, R. Kind, X. Yuan, and C. Estabrook, (2000(b)), A detailed receiver function image of the upper mantle discontinuities in the Japan subduction zone, Earth Planet. Sci. Lett., 183, 527–541.

Li, X., R. Kind, X. Yuan, S. V. Sobolev, W. Hanka, D. S. Ramesh, Y. Gu, and A. M. Dziewonski, (2003), Seismic observation of narrow plumes in the oceanic upper mantle, Geophys. Res. Lett., 30(6), 1334.

Li, X., Kind, R., Yuan, X., Wölbern, I., Hanka, W. (2004), Rejuvenation of the lithosphere by the Hawaiian plume, Nature, 427, 827-829.

Li X., Yuan X., Kind R. (2007) The lithosphere-asthenosphere boundary beneath the western United States. Geophys. J. Int. 170(2):700–710

Lonergan, L., White N. (1997), Origin of the Betic-Rif mountain belt, Tectonics, 16, 504-522.

Martinez, M., Lana, X., Caselles, O., Canas, J., and Pujades, L. (2005), Elastic-anelastic regional structures for the Iberian Peninsula obtained from a Rayleigh wave tomography and a casual uncoupled inversion. Pure Appl. Geophys., 162: 2321-2353.

McClusky S., Reilinger R., Mahmoud S., Ben Sari D. and Tealeb A. (2003), GPS constraints on Africa (Nubia) and Arabia plate motions. Geophys. J. Int. 155, 126-138.

McKenzie, D.P., and Parker, D.L. (1967), The North Pacific: An example of tectonics on a sphere, Nature, 216:1276-1280.

McKenzie D. P. (1972), Active tectonics of the Mediterranean region. Geophysical Journal of the Royal Astronomical Society 30:109–185.

Medialdea, T., Surinach, E., Vegas, R., Banda, E. and Ansorge, J. (1986), Crustal structure under the western end of the Betic cordillera (Spain). Ann. Geophys., 4: pp. 457-464.

Mendes Victor, L.A., Hirn, A. and Veinante, J.L. (1980), A seismic section across the Tagus Valley, Portugal: possible evolution of the crust, Ann. Geophys. 36 (1980), pp. 469–776.

Mezcua, J., Rueda, J. (1997), Seismological evidence for a delamination process in the lithosphere under the Alboran Sea, Geophys. J. Int., 129, F1-F8.

Michard, A., Chalouan, A., Feinberg, H., Goffé, B., Montigny, R. (2002), How does the Alpine belt end between Spain and Morocco?, Bull. Societe Geol. France,173, 3-15.

Mohorovicic, A. (1909), Das Beben vom 8. X. 1909, Jahrb. Meteorol., Observatorium Zagreb für das Jahr 1909, 9, Pt. IV, Sec. 1, 63 pp..

Monroe, J. S., Wicander, R. (2008), The changing Earth: exploring geology and evolution (5th ed.). Cengage Learning. p. 216.

Morales, J., Serrano, I., Vidal, F., and Torcal, F. (1997), The depth of the earthquake activity in the Central Betics (Southern Spain), Geophys. Res. Lett., 24(24), 3289–3292.

Morales, J., Jabaloy, A., Galindo-Zaldívar, J., Zhao, D., Torcal, F., Vidal, F. and González Lodeiro F. (1999), Active continental subduction beneath the Betic Cordillera and the Alborán Sea, Geology August, 27, 735-738.

Morley, C. K. (1993), The origin of sedimentary basins: Inferences from quantitative modelling and basin analysis Tectonophysics 226, 359-376.

Mueller, St., Prodehl, C., Mendes, A.S. and Sousa Moreira, V. (1973), Crustal structure in the southern part of the Iberian Peninsula. Tectonophysics, 20:307-318.

Neele, F., Sharp 400 km discontinuity from P reflections. (1996), Geophys. Res. Lett., 23, 419-422.

Nettles, M. and Dziewoński, A.M. (2008), Radially anisotropic shear-velocity structure of the upper mantle globally and beneath North America. J. Geophys. Res., 113(B02303).

Niazi, M., and D. L. Anderson (1965), Upper Mantle Structure of Western North America from Apparent Velocities of P Waves, J. Geophys. Res., 70(18), 4633–4640.

Niu, F. and James, D.E. (2002), Fine structure of the lowermost crust beneath the Kaapvaal Craton and its implications for crustal formation and evolution. Earth Planet. Sci. Lett., 200, 121–130.

Oldenburg, D. W. (1981), A comprehensive solution to the linear deconvolution problem, Geophys. J. Int., vol. 65, issue 2, pp. 331-357.

Oldham R. D. (1906), The Constitution of the Interior of the Earth as revealed by Earthquakes, Quart. J. Geological Soc. Lond., 62, 456-475.

Owens, T. J., G. Zandt and S. R. Taylor, (1984), Seismic evidence for an ancient rift beneath the Cumberland Plateau, Tennessee: A detailed analysis of broadband teleseismic P waveforms, J. Geophys. Res., 89, 7783-7795.

Owens, T. J. (1987), Crustal structure of the Adirondacks determined from broadband teleseismic waveform modeling, J. Geophys. Res., 92, 6391-6401.

Palomeras, I., Carbonell, R., Flecha, I., Simancas, F., Ayarza, P., Matas, J., Martínez Poyatos, D., Azor, A., González Lodeiro, F., Pérez-Estaún A. (2009), Nature of the lithosphere across the Variscan orogen of SW Iberia: Dense wide-angle seismic reflection data. J. Geophys. Res. (114), B02302, 29 PP.

Paulssen, H. (1985), Upper mantle converted waves beneath the NARS Array. Geophys. Res. Lett. 12, 709–712.

Perouse E., Vernant P., Chery J., Reilinger R. and McClusky S. (2010), Active surface deformation and sub-lithospheric processes in the western Mediterranean constrained by numerical models. Geology 38, 823-826, doi: 10.1130/G30963.1

Platt, J. and Vissers, R. (1989), Extensional collapse of thickened continental lithosphere: A working hypothesis for the Alboran Sea and Gibraltar arc, Geology, 17, 540-543.

Platt, J.P., Soto, J.I., Comas, M.C. and Leg 161 Shipboard Scientific Party (1996), Decompression and high-temperature - low-pressure metamorphism in the exhumed floor of an extensional basin, Alboran Sea, western Mediterranean. Geology 24, 477-450.

Phinney R A. (1964), Structure of the Earth's crust from spectral behavior of long-period body waves. J. Geophys. Res., 69: 29973017

Polyak B.G., Fernàndez M., Khutorskoy M.D., Soto J.I., Basov I.A., Comas M.C., Khain V.Ye., Alonso B. , Agapova G.V. , Mazurova I.S., Negredo A.M., Tochitsky, V.O., Linde J. de la, Bogdanov N.A. and Banda E. (1996), Heat flow in the Alboran Sea (the western Mediterranean). Tectonophysics 263, 191–218.

Piromallo, C. and Morelli, A. (2003), P-wave tomography of the mantle under the Alpine-Mediterranean area, J. geophys. Res., 108

Rehault, J.-P., Boillot, G., and Mauffret, A. (1985), The Western Mediterranean basin, in Stanley, D.J., and Wezel, F.-C., eds., Geological evolution of the Mediterranean basin: New York, Springer-Verlag,101–129.

Ringwood, A. (1970), Phase transformations and constitution of the mantle. Phys Earth Planet. Inter., 3, 109-155.

Royden L. H. (1993), Evolution of retreating subduction boundaries formed during continental collision, Tectonics, 12, 629-638.

Rychert, C. A., Fischer, K. M. and Rondenay, S. (2005), A sharp lithosphere-asthenosphere boundary imaged beneath eastern North America, Nature, 436, 542-545.

Schaer, J.P. (1987), Evolution and structure of the High Atlas of Morocco. In: Schaer, J.P., Rodgers, J. (Eds.), The Anatomy of Mountain Ranges. Princeton Univ. Press, Princeton, N.J., pp. 107– 127.

Schwarz, G., Wigger, P. J. (1988), Geophysical studies of the Earth's crust and upper mantle in the Atlas system of Morocco, Lecture notes in Earth Science 15 Springer 339-357.

Seber D., Barazangi M., Ibenbrahim A. and Demnati A. (1996a), Geophysical evidence for lithospheric delamination beneath the Alboran Sea and Rif–Betic mountains, Nature 379, 785 – 790.

Seber, D., Barazangi M., Tadili B.A., Ramdani M., Ibenbrahim A., and Ben Sari D. (1996b), Three-dimensional upper mantle structure beneath the intraplate Atlas and intraplate Rif mountains of Morocco. J. Geophys. Res. 101 (B2), 3125-3138.

Shearer, P. M. et al. (2000), in Earth's Deep Interior: Mineral Physics and Tomography from the Atomic to the Global Scale (ed. Karato, S.-I.) 115 (AGU Geophys. Monogr, Vol. 117, Washington DC).

Sheehan, A. F., G. A. Abers, C. H. Jones, and A. L. Lerner-Lam (1995), Crustal thickness variations across the Colorado Rocky Mountains from teleseismic receiver functions, J. Geophys. Res., 100, 20,391– 20,404.

Shen, Y., Solomon, S. C., Byarnason, I. T., and Wolfe C. J. (1998), Seismic evidence for a lowermantle origin of the Iceland Plume, Nature, 395, 62-65.

Shim S.H., Duffy, T. S. , Shen G. (2001) The post-spinel transformation in Mg2SiO4 and its relation to the 660-km seismic discontinuity. Nature 411: 571-574

Shiomi, K., H. Sato, K. Obara, and M. Ohtake (2004), Configuration of subducting Philippine Sea plate beneath southwest Japan revealed from receiver function analysis based on the multivariate autoregressive model, J. Geophys. Res., 109, B04308.

Sousa Moreira V., Mueller St., Mendes A.S. and Prodehl C. (1978), The deep structure of southern Portugal, Geodinámica de la Cordillera Bética y Mar de Alborán, University of Granada, pp. 35–41.

Sousa Moreira V., Prodehl C., Mueller St. and Mendes A.S. (1983), Crustal structure of western Portugal. In: E. Bisztricsàny and G.Y. Szeidovitz, Editors, Developments in Solid Earth Geophysics 15, Elsevier, Amsterdam (1983), pp. 529–532 Proceedings of the 17th Gen. Assoc. Eur. Seismol. Comm., Budapest, 1980.

Spakman W. and Wortel R. (2004), A tomographic View on Western Mediterranean Geodynamics, in The TRANSMED Atlas, The Mediterranean Region from Crust to Mantle, 31-52, eds Cavazza W., Roure EM., Spakman W., Stampfli G.M. And Ziegler P., Springer-Verlag Berlin.

Stammler, K. (1993), Seismic Handler – Programmable multichannel data handler for interactive and automatic processing of seismological analyses, Computers and Geosciences, Vol. 19, No. 2, 135-140.

Suriñach, E. and Vegas, R. (1988), Lateral inhomogeneities of the Hercynian crust in Central Spain . Phys. Earth Plan. Int., 51, 226 – 234.

Toksöz, M. N. and Ben-Menahem, A. (1963), Velocities of mantle Love and Rayleigh waves over multiple paths, Bull. seism. SOC. Am., 53, 741 -764.

Toksöz, M. N. and Anderson, D. L. (1966), Phase velocities of long-period surface waves and structure of the upper mantle, 1. Great-circle Love and Rayleigh wave data, J. geophys. Res., 71, 1649-1658.

Torné, M., and Banda, E. (1992), Crustal thinning from the Betic Cordillera to the Alboran Sea. Geo-Mar. Lett., 12:76-81.

Torné, M., Fernàndez, M., Comas, M.C. and Soto, J.I. (2000), Lithospheric structure beneath the Alboran Basin: results from 3D gravity modeling and tectonic relevance. J. Geophys. Res., 105, 3209–3228.

Vernant Ph., Fadil A., Mourabit T., Ouazar D., Koulali A., Davila J. M., Garate J., McClusky S. and Reilinger R. (2010), Geodetic constraints on active tectonics of the Western Mediterranean: Implications for the kinematics and dynamics of the Nubia-Eurasia plate boundary zone. Journal of Geodynamics 49, 123-129.

Vidale, J. E., Ding, X.-Y. and Grand, S. P. (1995), The 410-km-depth discontinuity: A sharpness estimate from near-critical reflections, Geophys. Res. Lett., 22, 2557-2560.

Vinnik, L. P. (1977), Detection of waves converted from P to SV in the mantle: Physics Earth Planet. Interiors, 15, 39–45.

Watts, A. B., Platt, J. P. and Buhl, J. P. (1993), Tectonic evolution of the Alboran Sea Basin Res. 5, 153-177 .

Wegener, A. (1912), Die Entstehung der Kontinente: Geologische Rundschau, v. 3, pp.276-292.

Wessel, P., and W. H. F. Smith, (1991), Free Software helps Map and Display Data, EOS Trans. AGU, 72, 441, 445-446.

Wessel, P., and W. H. F. Smith, (1998), New, Improved Version of Generic Mapping Tools Released, EOS Trans., AGU, 79 (47), p. 579.

Wigger P., Asch G., Giese P., Heinsohn W.D., El Alami S.O. and Ramdani F. (1992), Crustal structure along a traverse across the Middle and High Atlas mountains derived from seismic refraction studies. Geol. Rundschau, 81, 237-248.

Wiechert, E. (1896), Über die Beschaffenheit des Erdinnern. Sitz.-Ber. Physik.-ökonom. Ges. Königsberg 37,4.

Wiechert, E. (1897), Über die Massenverteilung im Erdinnern. Nachr. Kgl. Ges. Wiss. Göttingen, math.-phys. Kl, 221.

Wilson, J.T. (1965), A new class of faults and their bearing on continental drift, Nature, 207:343-347.

Yuan, X., Ni, J., Kind, R., Mechie, J. and Sandoval, E. (1997), Lithospheric and upper mantle structures of southern Tibet from a seismological passive source experiment, J. Geohpys. Res., 102, 27 491–27 500.

Yuan, X., et al. (2000), Subduction and collision processes in the central Andes constrained by converted seismic phases, Nature, 408, 958– 961.

Zeck, H.P. (1996), Betic-Rif orogeny: subduction of Mesozoic Tethys lithosphere under eastward drifting Iberia, slab detachment shortly before 22 Ma, and subsequent uplift and extensional tectonics. Tectonophysics, 254:1-16.

Zeyen H., Ayarza P., Fernàndez M. and Rimi, A. (2005), Lithospheric structure under the western African-European plate boundary: a transect across the Atlas Mountains and the Gulf of Cadiz, Tectonics 24 , p. TC2001 16pp.

Zhu, L., and H. Kanamori, (2000), Moho depth variation in southern California from teleseismic receiver functions, J. Geophys. Res., 105 (B2), 2969–2980.

Zhu, L. (2004), Lateral variation of the Tibetan lithospheric structure inferred from teleseismic waveforms, in Advancements in Seismology and Physics of the Earth Interior in China, Seismology Press, Beijing.

Appendix A: List of all stations and their characteristics.

STATION CODE	NETWORK CODE	LATITUDE (DEGREE)	LONGITUDE (DEGREE)	ALTITUDE (METER)	SEISMO-METER	TIME PERIOD USED
ACBG	Tedese-Projekt-Spain (TD)	36.8	-2.2	30	STS-2/N	2001-2004
ACLR	Tedese-Projekt-Spain (TD)	37.2	-2.6	1670	STS-2/N	2001-2004
ALB	Tedese-Projekt-Spain (TD)	35.9	-3.0	30	STS-2/N	2001-2004
CEU	Tedese-Projekt-Spain (TD)	35.9	-5.4	320	STS-2/N	2001-2004
CFS	Tedese-Projekt-Spain (TD)	35.2	-2.4	90	STS-2/N	2001-2004
ELUQ	Tedese-Projekt-Spain (TD)	37.6	-4.2	690	STS-2/N	2001-2004
EMAL	Tedese-Projekt-Spain (TD)	36.8	-4.4	150	STS-2/N	2001-2004
LIJA	Tedese-Projekt-Spain (TD)	36.9	-5.4	1000	STS-2/N	2001-2004
ORGV	Tedese-Projekt-Spain (TD)	36.9	-3.4	1270	STS-2/N	2001-2004
VLZ	Tedese-Projekt-Spain (TD)	35.2	-4.3	90	STS-2/N	2001-2004
AVE	Western-Mediterranea-Seismic-Network (WM)	33.3	-7.4	230	STS-2/N	1997-2011
CART	Western-Mediterranea-	37.6	-7.4	65	STS-2/N	1997-2011

STATION CODE	NETWORK CODE	LATITUDE (DEGREE)	LONGITUDE (DEGREE)	ALTITUDE (METER)	SEISMO-METER	TIME PERIOD USED
	Seismic-Network (WM)					
EMAL	Western-Mediterranea-Seismic-Network (WM)	36.8	-4.4	80	STS-2/N	2006-2011
EVO	Western-Mediterranea-Seismic-Network (WM)	38.5	-8.0	232	STS-2/N	2006-2011
IFR	Western-Mediterranea-Seismic-Network (WM)	33.5	-5.1	163	STS-2/N	2007-2011
MELI	Western-Mediterranea-Seismic-Network (WM)	35.3	-2.9	40	STS-2/N	1999-2011
SFS	Western-Mediterranea-Seismic-Network (WM)	36.5	-6.2	21	STS-2/N	2001- 2009
MTE	Portuguese seismic network (PM)	40.4	-7.5	815	STS-2/N	1997-2011
SELV	Western-Mediterranea-Seismic-Network (WM)	37.2	-3.7	650	STS-2/N	2001-2003
RTC	Mednet-Project (MN)	33.9	-6.9	50	STS-1/VBB	2003-2011
MDT	Mednet-Project (MN)	32.8	-4.6	1200	STS-1/VBB	1990-1998
PAB	Global-Seismogramph-Network (IU)	39.5	-4.3	925	STS-1/VBB	1992-2010

STATION CODE	NETWORK CODE	LATITUDE (DEGREE)	LONGITUDE (DEGREE)	ALTITUDE (METER)	SEISMO-METER	TIME PERIOD USED
TOL	Global-Seismogramph-Network (IU)	39.9	-4.0	480	STS-1/VBB	1992-1993
EVO	Geoscope (G)	38.5	8	0	STS-1/VBB	1996-2000
PVAQ	Portuguese National Seismic Network (PM)	37.4	-7.7	200	Guralp CMG-3T	2006-2011
PESTR	Portuguese National Seismic Network (PM)	38.9	-7.6	410	Guralp CMG-3T	2006-2011
PFVI	Portuguese National Seismic Network (PM)	37.1	-8.8	89	CMG-3ESP/120	2008-2011
GGNV	University of LISbon SEISmic Network (LX)	38.7	-9.1	77	CMG-40T	2007-2011
MESJ	University of LISbon SEISmic Network (LX)	37.8	8.2	250	STS-2	2007-2011
MORF	University of LISbon SEISmic Network (LX)	37.3	8.6	560	CMG-40T	2005-2011
ASCB	International Association of Geomorphologists (IAG)	37.0	-2.0	550	STS-2	2007-2008
VELZ	International Association of Geomorphologists (IAG)	37.6	-2.0	1000	STS-2	2007-2008
SESP	International Association of Geomorphologists (IAG)	38.1	-2.54	1528	STS-2	2007-2008
JAND	International Association of Geomorphologists (IAG)	38.2	-4.0	645	STS-2	2007-2008

STATION CODE	NETWORK CODE	LATITUDE (DEGREE)	LONGITUDE (DEGREE)	ALTITUDE (METER)	SEISMO-METER	TIME PERIOD USED
HORN	International Association of Geomorphologists (IAG)	37.8	-5.3	268	STS-2	2007-2008
ANER	International Association of Geomorphologists (IAG)	36.7	-3.8	170	STS-2	2007-2008
ARAC	International Association of Geomorphologists (IAG)	37.9	-6.6	675	STS-2	2007-2008
ESTP	International Association of Geomorphologists (IAG)	37.2	-4.9	893	STS-2	2007-2008

Appendix B: List of the Moho depth estimated for each station.

STATION-CODE	LONGITUDE (Degree)	LATITUDE (Degree)	MOHO-DEPTH (Km)
ALB	-3.030000	35.930000	16
ACLR	-2.583000	37.188000	17
ACBG	-2.195000	36.767000	18
CART	-1.001000	37.587000	18
CFS	-2.431000	35.184000	19
MELI	-2.939000	35.290000	20
ELUQ	-4.268000	37.559000	24
ASCB	-2.005700	37.039300	24
ORGV	-3.429000	36.859000	24
MESJ	-8.220000	37.840000	25
IFR	-5.130000	33.520000	27
ANER	-3.845300	36.762300	27
MTE	-7.540000	40.400000	27
PFVI	-8.826800	37.132800	27
ARAC	-6.564700	37.892300	28
MORF	-8.650000	37.300000	28
HORN	-5.258200	37.846600	29
JAND	-3.970483	38.221580	29
EVO	-8.016740	38.529400	29
PESTR	-7.590199	38.867199	29
TOL	-4.049000	39.881000	29
PAB	-4.348300	39.545800	30
PVAQ	-7.717299	37.403702	30
GGNV	-9.150000	38.720000	30
VELZ	-1.988000	37.583800	30
GORA	-3.039800	37.480500	31
AVE	-7.410000	33.300000	33
MDT	-4.614000	32.817000	33
SELV	-3.730000	37.236000	33
SESP	-2.545200	38.120800	33
EMAL	-4.428000	36.762000	33

ESTP	-4.866200	37.27	34
VLZ	-4.367000	35.167000	35
RTC	-6.856900	33.988100	35
LIJA	-5.404000	36.906000	35
SFS	-6.210000	36.460000	40
CEU	-5.373700	35.898300	40

Appendix C: Figure 1: Cross-section of vertical **(A)** and horizontal map **(B)** view. Summation traces were generated applying a band-pass filter from 1 to 30s.

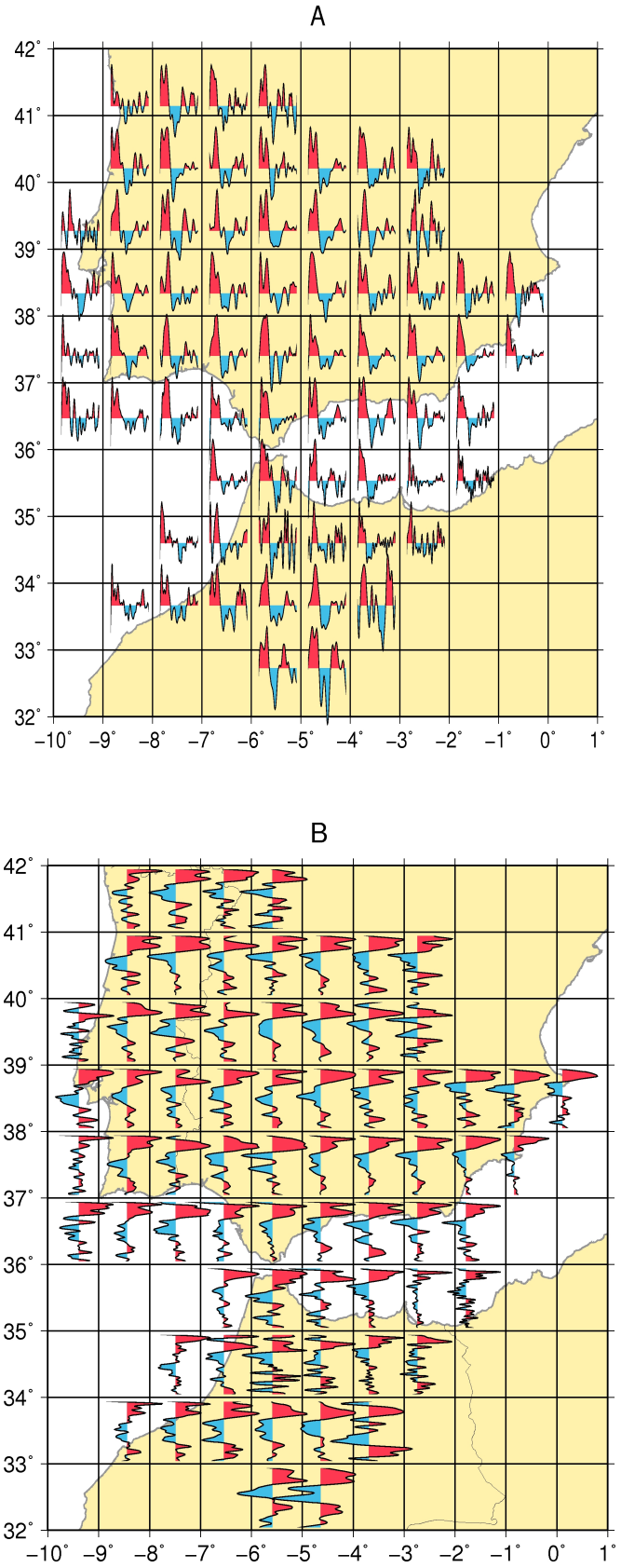

Appendix D: Figure 2: Cross-section of vertical **(A)** and horizontal map **(B)** view. Summation traces were generated applying a band-pass filter from 3 to 30s.

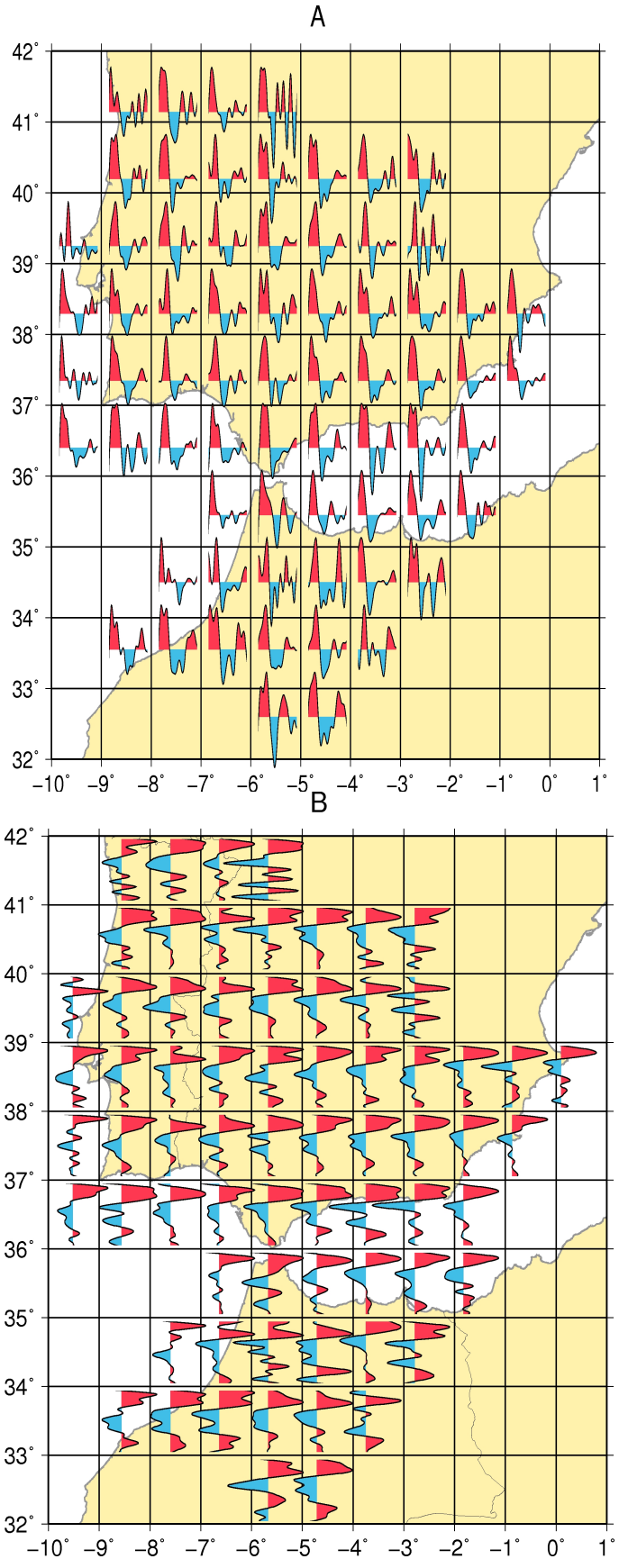

Appendix E: The location of the center of the 1°X1° gridboxes and the obtained LAB depth values for each defined grid.

LONGITUDE (DEGREE)	LATITUDE (DEGREE)	LAB-DEPTH (Km)
-8.5	41.5	78
-7.5	41.5	80
-6.5	41.5	80
-5.5	41.5	76
-8.5	40.5	94
-7.5	40.5	82
-6.5	40.5	70
-5.5	40.5	72
-4.5	40.5	96
-3.5	40.5	70
-8.5	39.5	90
-7.5	39.5	98
-6.5	39.5	104
-5.5	39.5	84
-4.5	39.5	80
-3.5	39.5	78
-2.5	39.5	66
-9.5	38.5	104
-8.5	38.5	96
-7.5	38.5	88
-6.5	38.5	92
-5.5	38.5	104
-4.5	38.5	98
-3.5	38.5	92
-2.5	38.5	94
-1.5	38.5	64
-0.5	38.5	66
0.5	38.5	58
-9.5	37.5	98
-8.5	37.5	104

-5.5	32.5	94
-4.5	32.5	86